Gaseous hydrogen embrittlement of 3D-printed Inconel 718 manufactured from sustainable feedstock

Naveen K Mohandas

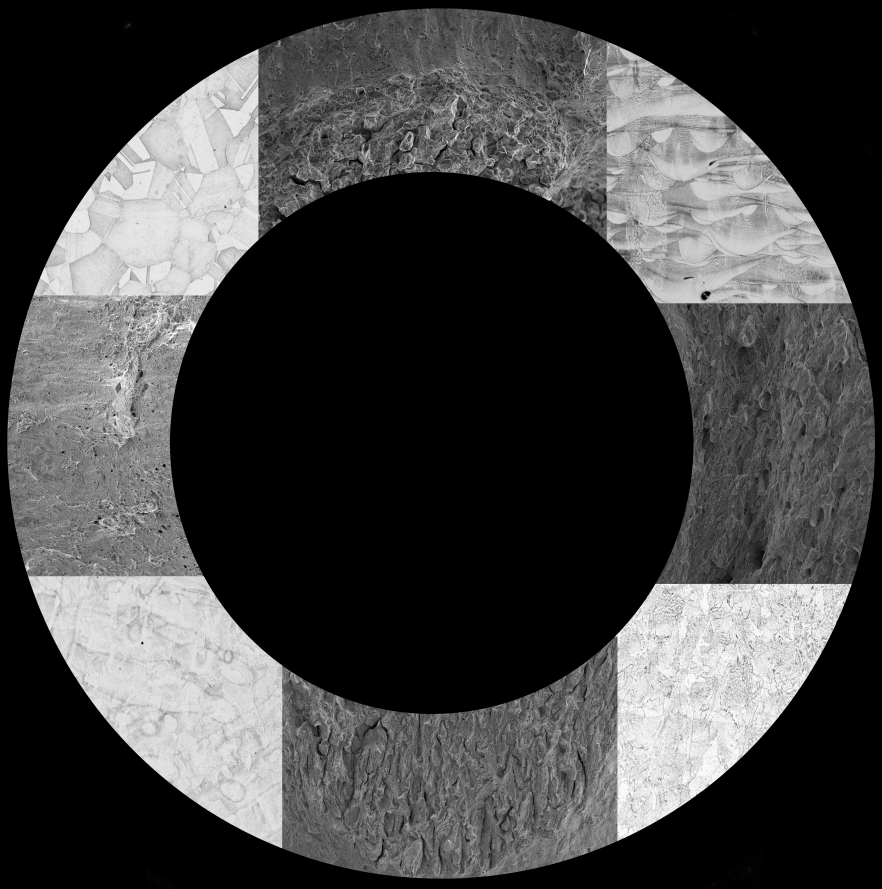

TU Delft

Gaseous hydrogen embrittlement of 3D-printed Inconel 718 manufactured from sustainable feedstock

by

Naveen K Mohandas

to obtain the degree of Master of Science
at the Delft University of Technology,
to be defended publicly on October 18, 2022 at 13:00.

Student number:	5258839	
Project duration:	February 1, 2022 – October 18,2022	
Thesis committee:	Dr. Vera Popovich (MSE),	TU Delft, supervisor
	Dr. Can Ayas (PME) ,	TU Delft
	Dr. Poulumi Dey (MSE),	TU Delft
	Dr. Yaiza Gonzalez Garcia (MSE)	TU Delft
	Ir. Tim Boot	TU Delft

An electronic version of this thesis is available at `http://repository.tudelft.nl/`.

TU Delft

Acknowledgements

This thesis has been a journey to find answers both academically and personally; and this endeavour would not have been possible without the guidance of Dr. Vera Popovich. Thank you Vera, for the critical discussions and being the light guiding the way. I would also like to thank the people at Fenice, Matteo Vanazzi and Alex Giorgini for providing with the materials and promptly replying to all the queries I had. Then I would like to thank the lab technicians, Ton Riemslag and Sean Scott without whom the experiments would not have been possible. Thank you for providing innovative solutions for the numerous hurdles I faced and also making sure that I did the experiments right. When mentioning the lab, I need to mention the the student assistants Kevork Perez and Roel Webb, who made it fun and lively to work in the lab. Additional thanks to Kevork for showing how as engineers we can always find a solution in life. I also thank Ruud Hendrikx and Richard Huizenga for the X-Ray characterisation and analysis. I am also grateful to Remko Seijffers for the immediate support with the equipments at microscopy lab, and also the student assistants there, Maria Terol Sanchez for training me to use all equipments and Alice Dautezac for dealing with my email spams for booking SEM slots.

Personally I would like to thank my friends, MS Suryanarayanan, Roland Varga, Shaurya Verma, Joe Joseph, Harishankar S Bhat, Archana P S, Anagha Dinesh and Alfred Jose P whose constant support and encouragement helped me get through difficult times. Lastly, I would like to thank my parents and my sister for the unconditional love and support, without it I wouldn't have been able get this far.

Naveen K Mohandas
Delft, October 2022

Abstract

Laser powder bed fusion (L-PBF) is an additive manufacturing (AM) technology that has been gaining a lot of interest as it allows to produce parts with complex geometries and eliminate expensive tooling. Unlike the conventional manufacturing processes where material is removed to make the final component; AM part is manufactured layer-wise as per the required geometry. Due to this, the material wastage in the AM process is minimal. In addition, powder feedstock produced from recycled materials can promote a more sustainable L-PBF. It is however known that properties of L-PBF material are influenced by numerous variables, among which is the powder feedstock. It is thus important to investigate mechanical and other functional properties of AM components produced from recycled feedstock.

Inconel 718 is a Nickel-based superalloy that is often used in turbine blades and heat exchangers where high performance in extreme environments is required. Good mechanical properties of Inconel 718 and high design flexibility enabled by L-PBF process allow to expend applications of this alloy to fuel injection nozzles used for liquid hydrogen fuel engines or tubing for fuel transport in the engine. Although Inconel 718 shows good performance in high temperature applications, in the presence of hydrogen the material is found to lose ductility.

This study investigated the in-situ gaseous (under 150 Bar) hydrogen embrittlement behaviour of L-PBF Inconel 718 manufactured from sustainable feedstock. It was found that despite its higher yield strength, heat treated L-PBF samples demonstrate 64% lower degree of hydrogen embrittlement compared to the wrought counterpart. This was linked to anisotropic microstructure induced by L-PBF process, which was found to cause directional embrittlement unlike the wrought samples showing isotropic embrittlement.

In conclusion, this study shows that L-PBF Inconel 718 produced from recycled feedstock shows better hydrogen embrittlement resistance compared to the wrought sample. Furthermore, the unique anisotropic properties, seen in this study for L-PBF Inconel, could be considered further in component design to help minimise the degree of hydrogen embrittlement.

Abbreviations

AC	Air Cooled
AIDE	Adsorption Induced Dislocation Emission
AM	Additive manufacturing
ASS	Austenitic Stainless Steel
AP	As-processed
BD	Build direction
CAD	Computer Aided Design
DA	Double aging
FC	Furnace cooled
FCC	Face Centered Cubic
GA	Gas atomisation
HC	Hydrogen Charged
HE	Hydrogen Embrittlement
HEDE	Hydrogen Enhanced Decohesion
HEI	Hydrogen embrittlement Index
HELP	Hydrogen Enhanced Localised Plasticity
HIP	Hot Isostatic Pressing
HT	Heat Treatment
L-PBF	Laser Powder Bed Fusion
LOF	Lack of fusion defects
PREP	Plasma rotating electrode process
RA	Rotary atomisation
SEM	Scanning electron microscope
SFE	Stacking Fault Energy
SLM	Selective Laser Melting
SSRT	Slow Strain Rate Tensile test
UC	Uncharged (hydrogen absent)
UTS	Ultimate Tensile Strength
VED	Volume Energy Density
WA	Water atomisation
XRF	X-Ray fluorescence spectroscopy
Ys	Yield Strength

Contents

List of Figures

List of Tables

1

Introduction

There is an increased need for sustainable solutions as the world moves towards a greener future. Achieving a circular economy is one of the primary goals in this transition. In simple words, a circular economy involves recycling materials and minimising the extraction of materials from nature. Figure 1.1 is a general illustration of the concept; the primary focus here is the recycling of metals which fits in the blue region.

Laser Powder Bed Fusion (L-PBF) is a metal additive manufacturing (AM) technology which utilises laser to melt the feedstock which is in the form of metal powder. By recycling the powder feedstock it would be possible to promote a circular economy. The major limitation with this is that the powder feedstock is one among the key variables affecting the component properties. Even among the commercially available powders, it is observed that the mode of powder production can induce difference in properties. This poses a challenge as feedstock produced from recycled materials could further increase the variability.

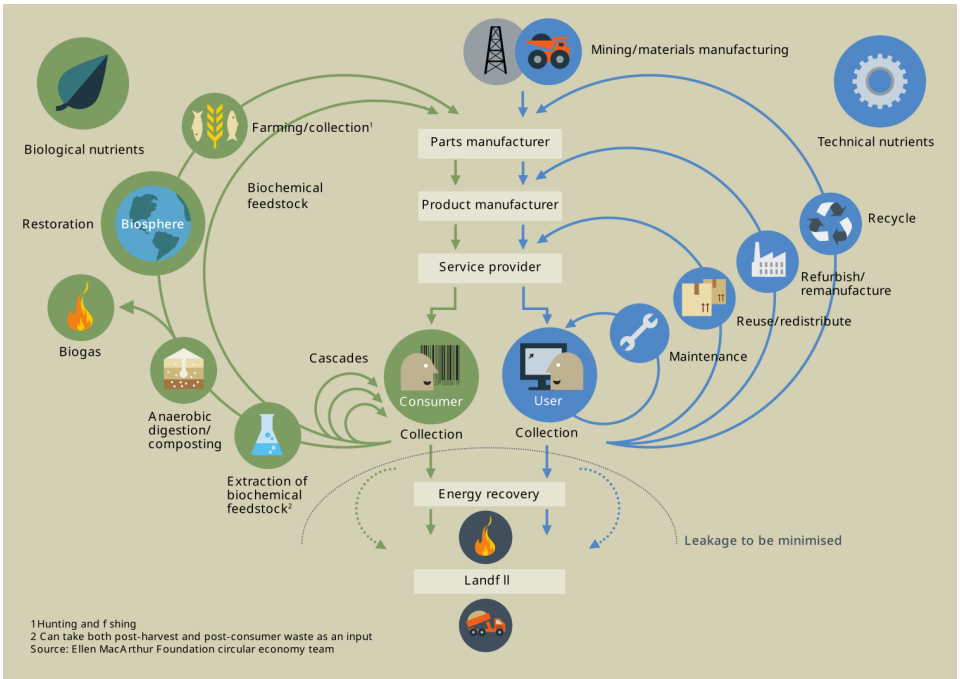

Figure 1.1: Illustration of Circular economy. Reproduced from [1]

The hydrogen economy is another aspect of the transition to a greener future. It relies on using hydrogen as a fuel for energy production. On a weight basis, hydrogen has three times the energy content of gasoline; however, being a low-density gas, hydrogen storage and transport poses a major hurdle in the transition[2]. This means there is a need for materials compatible with hydrogen. Inconel 718 is a nickel-iron-chromium alloy widely used in hydrogen servicing conditions due to its excellent corrosion and mechanical properties in a wide temperature range[3]. Due to the presence of numerous alloying elements, it has a complex microstructure, which is further dependent on the manufacturing route and the post-processing treatments. In the 1990s, the main engine of a hydrogen fuel-based space shuttle comprised of 51% of this alloy[4]. However, it was found that the material is susceptible to hydrogen embrittlement, thereby sparking a profound interest in understanding its interaction with hydrogen. As the material's microstructure plays a key role in hydrogen embrittlement, Inconel 718 that has undergone different processing route shows different degrees of embrittlement.

Soller et al.[5] describes how L-PBF could be utilised to produce injectors from Inconel 718 and stainless steel for a liquid rocket engine, which are complex and demanding. Additive manufacturing technology has the potential to eliminate numerous integration steps involved in conventional manufacturing mode, thereby reducing production costs[6]. Nevertheless, if it were to be used for hydrogen-based fuels, it is necessary to prevent hydrogen embrittlement in Inconel 718. There is however a caveat, the properties of the components from L-PBF process are influenced by numerous process variables specific to the technology. A broad classification of the process variables is heat-source parameters and feedstock properties[7]. So to understand hydrogen embrittlement in components produced from L-PBF, it is necessary to account for the process-specific properties and defects; and how it interacts with hydrogen.

This thesis aims to study hydrogen embrittlement of additively manufactured Inconel 718 produced from the recycled powder feedstock and relate it to the process-induced defects, such as porosity and anisotropy. To do so, initially, a comprehensive literature study is done to identify the research gaps and presented in Chapter 2. This knowledge is then utilised to design the experiment for evaluating the hydrogen embrittlement behaviour of L-PBF Inconel 718 as elaborated in Chapter 3. Chapter 4 focuses on the results and discussion obtained from the experiments. The final chapter consists of the conclusions obtained from this thesis along with future recommendations.

2

Background

2.1. Inconel 718

Inconel 718 is a Ni-Fe-Cr based superalloy well known for its good corrosion and mechanical properties in a wide temperature range, hence has been extensively used in aircraft engines, nuclear reactors, thermal power plants and so on[8, 4]. The required mechanical properties and corrosion resistance is achieved by tailoring the microstructure and introducing suitable phases in the matrix through post-processing heat treatments. The alloy contains numerous alloying elements, the composition is as given in Table 2.1, which gives rise to an array of secondary phases both beneficial and detrimental to its properties. The good weldability of the alloy makes it a suitable candidate for additive manufacturing technology, specifically laser powder bed fusion (L-PBF) also known as selective laser melting(SLM)[7]. The design flexibility of the process makes it possible to produce components that are otherwise unfeasible. In the subsequent sections of the chapter the microstructure and mechanical properties of Inconel 718 produced by L-PBF and conventional methods will be elucidated.

2.1.1. Manufacturing Process

Conventional

The conventional production route of Inconel 718 begins with the fabrication of large ingots or electrodes by vacuum induction melting (VIM) to form the base alloy. Subsequently, the ingots undergo one of the three major processing routes: 1) remelting followed by investment casting, 2) remelting and then wrought processing, or 3) remelting to form alloy powder that is consolidated and subjected to wrought processing operations [10].

Investment casting is the choice of production for components with complex shapes and structures, like turbine blades and vanes. Single-use ceramic moulds containing silica, alumina and/or zirconia are used in this process. The remelted alloy is poured into the mould of the required shape in a preheated vacuum chamber to obtain the casting.

Table 2.1: Composition of Inconel 718 [9]

Composition wt.%												
Ni	Cr	Fe	Co	Mo	W	Nb	Ti	Al	C	Mn	Si	B
50.00-55.00	17.00-21.00	bal.	1.00	2.8-3.3	-	4.75-5.5	0.65-1.15	0.20-0.80	0.08	0.35	0.35	0.006

Depending on the end application, equiaxed grains, columnar grains or single crystals are produced by this method[10]. For columnar and single crystals, the casting is withdrawn at a controlled rate from the hot zone in the furnace to a cold zone. Subsequent post-processing treatments are required to reduce segregation, remove porosity or alter the grain structures.

In the case of wrought alloy, the material is cast as consumable electrodes during the primary melting process[10]. It is then remelted to obtain a more homogeneous ingot by electro-slag remelting (ESR), vacuum arc remelting (VAR) or electron beam cold hearth refining (EBCHR). The remelted ingots are subjected to homogenisation treatments to remove micro-segregation. Subsequently, thermo-mechanical treatments are employed to produce billets or bars.

Powder processing routes were introduced to overcome the limitations of melt-related defects and produce advanced high-strength components. The process begins with the atomisation of a highly alloyed VIM ingot in gas or vacuum. The rapid solidification effectively suppresses the macro-segregation in the fine powders[10]. The powder size is critical for reducing the defects in the final components. Although a smaller powder size is preferred, it is not economically feasible as the yield is substantially reduced. Hot isostatic pressing or extrusion is then used to consolidate the powder and produce the billet. The conventional processing routes are all summarised in Figure 2.1.

The wrought materials in the form of ingots or billets are machined to obtain the final product. The strain hardening rate, hard carbide particles and high toughness of the material lead to premature tool failure during machining posing a bottleneck in the production of complex and intricate structures[11].

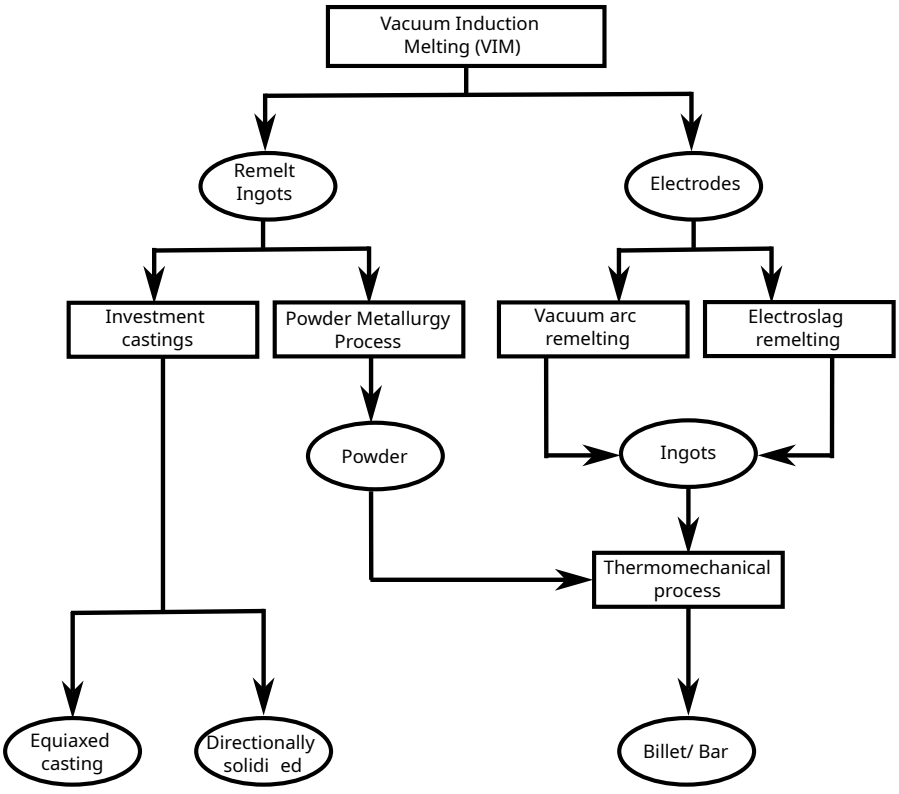

Figure 2.1: Flow diagram of conventional processing for Inconel 718. Reproduced from [10]

Additive Manufacturing

Additive manufacturing fabricates the component by addition of material layer by layer as the name suggests; unlike the conventional manufacturing methods where the material is removed to obtain the final component. This has the advantage that there is minimum material wastage[6]. In addition, the technology allows freedom to produce components with complex shapes and geometry directly from computer-aided design (CAD) models easily. The various steps involved in AM process is summarised in Figure 2.2 a).

In the current landscape, additive manufacturing covers a wide range of technologies classified based on the material and printer technology. Among them, metal-based AM technologies have been gaining traction as it is possible to produce functional components with complex geometry or structures. Metal AM technologies are further differentiated based on the type of feedstock (wire or powder) and heat source (laser or electron beam or gas metal arc)[7]. Though in theory, the primary steps involved are the same in all-metal AM technologies the properties of the final component vary due to the complexities in the AM processes. Laser-Powder bed fusion (L-PBF) is one of the metal AM technologies showing promising results. In this technology, metal powders are the feedstock; which are layered on a substrate and then completely melted using a high-power laser. The components present in a typical L-PBF machine are as shown in Figure 2.2b).

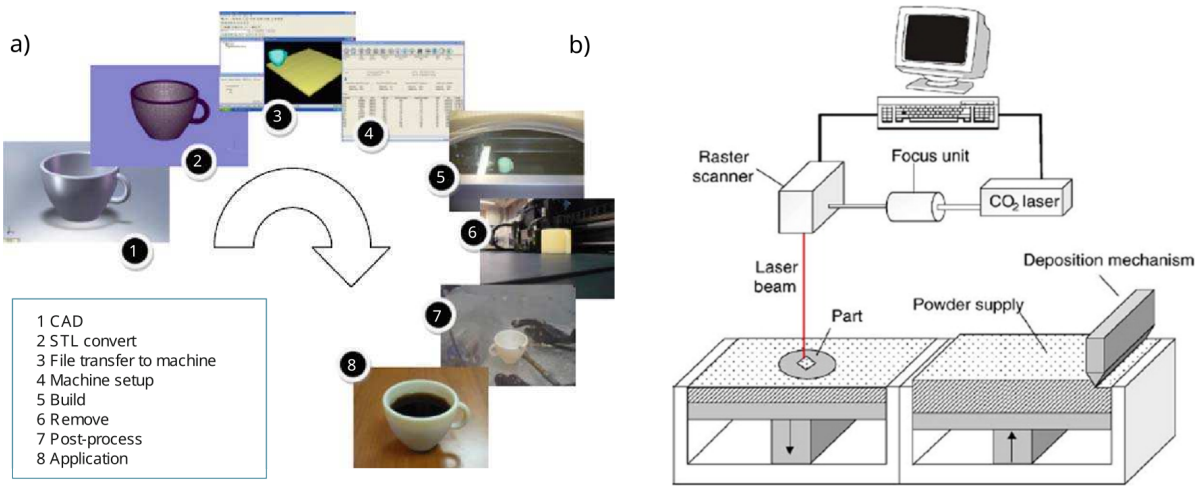

Figure 2.2: a) Steps involved in AM b)Schematic of L-PBF technology. Reproduced from [12] and [13] respectively.

In L-PBF, the feedstock powder characteristics affect the quality of the final product, which in turn depends on the powder manufacturing process. The powders are produced mainly in four ways: 1) Gas atomisation (GA), 2) Rotary atomisation (RA), 3) Plasma rotating electrode process (PREP), and 4) Water atomisation (WA)[7]. Figure 2.3 shows SEM images of powders produced by different processing routes. With changes in powder surface morphology, size, composition and shape, characteristics like porosity, inter-layer bonding, surface roughness, and minimum layer thickness varies drastically. A more detailed explanation is provided in the later sections.

Once the feedstock is available and the CAD model is uploaded into the machine, the 3-D printing process starts (the software aspects of the process is not covered here if required the reader is advised to refer [12]). The first stage in the process is the layering of the powder feed onto a metal substrate from the powder dispenser. The laser then scans the

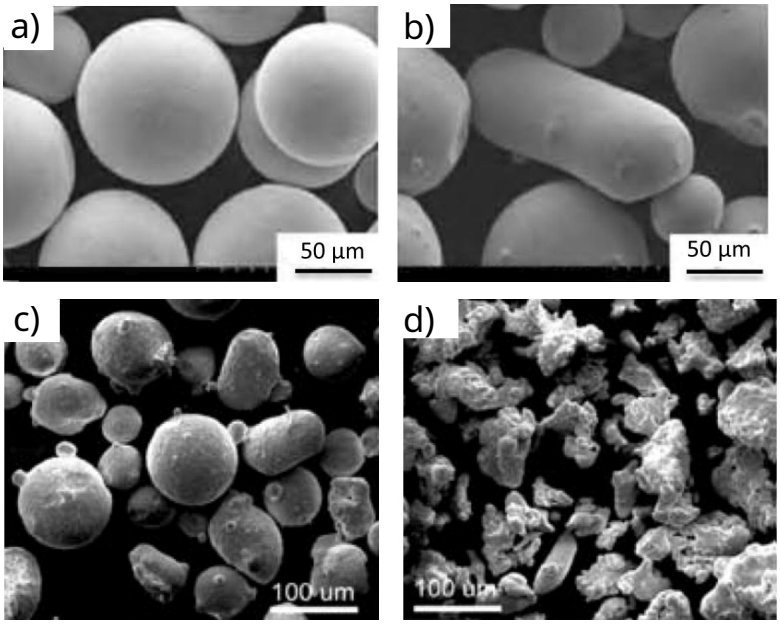

Figure 2.3: SEM micrographs of alloy powders manufactured by (a) PREP (b) RA (c) GA and (d) WA process. Reproduced from [7].

pattern corresponding to the layer obtained from the CAD model and melts the powder. The substrate then moves down by a layer thickness and a fresh layer of powder is spread over the previous layer. The laser then scans the pattern for the second layer. This process is repeated for the subsequent layers to form the final component.

L-PBF technology has several process parameters that could be altered to vary the properties of the component, the most important process parameters are: laser power (P), laser scan speed (v), layer thickness (t), hatch distance (h) and scan strategy. Among them, the parameters laser power, layer thickness hatch distance and scan speed are together considered as volume energy density. VED is given by Equation 2.1 where E is in J/mm^3, P is in Watts, v is in mm/s and t and h are in mm. It is generally found that using a high VED leads to higher density[14]. However, it should be noted that for the same VED the properties could vary depending on the difference in scan speed and laser power[7].

$$E = \frac{P}{v \cdot t \cdot h} \tag{2.1}$$

As mentioned earlier, the quality of the powder feedstock is key in obtaining dense and high-performance components, however variation in part properties arising from the differences in powder is not well documented in the literature. For the same process parameters, GA powder produces components with higher porosity than PREP powder. This is because GA powders contain gas bubbles entrapped during the atomisation process. Similarly, when GA and WA are compared: thinner deposition layers are needed for WA powders due to poor powder flowability. Among the different powders, PREP shows the most uniform powder size distribution, whereas WA shows the least[7].

The large number of influential parameters along with the highly dynamic nature of the process leads to a high degree of variance in mechanical properties and introduce defects such as lack of fusion, porosities, cracking, balling, residual stress build-up and so on in the component[15, 16]. This makes it necessary to identify process maps that could guarantee

reproducibility and minimise defects. In the current scenario, researchers have reported process parameters that can produce near defect free components for L-PBF Inconel 718[7, 17].

2.1.2. Microstructure

The microstructure of Inconel 718 is quite complex with different phases, like Laves phase, MC carbides, δ phase, γ' and γ", present in the primary fcc (γ) matrix. Some of these phases are necessary to enhance the strength of the material, whereas others are detrimental to the properties. A brief description of different phases present, microstructure in as processed condition and post processing heat treatments are discussed in the following sections.

The following phases are found in Inconel 718:
γ' **phase** is a intermetallic phase having a fcc lattice structure ($L1_2$) and stoichiometric composition given by $Ni_3(Al, Ti)$. The precipitate is coherent with the matrix and has the orientation relationship <100>$_{\gamma'}$ // <100>$_{\gamma}$ and <010>$_{\gamma'}$ // <010>$_{\gamma}$[18]. Aluminium and Titanium are the main alloying elements added for the precipitation of this phase and it is one of the primary strengthening phases in Inconel 718 [19]. The difference in lattice parameters of the γ matrix and the γ' precipitate results in lattice mismatch and to maintain coherency tetragonal distortion is introduced at the interface. The morphology of the precipitate is dependent on the degree of mismatch, during the initial phase of precipitation when the lattice mismatch is in the range of 0-0.2% it has spherical morphology, this transitions into a cuboidal morphology as the misfit increases to 0.5-1% and for misfit greater than 1.25% it becomes a plate-like precipitate. To optimise the strength and performance of the material the size and morphology of the precipitate needs to be controlled, which is done by heat treatment at suitable ageing temperature and time (referred to as coarsening process)[19].
γ" **phase** is the other primary strengthening phase in Inconel 718 and is formed due to the presence of niobium. The precipitate is coherent with the matrix and has $D0_{22}$ fcc lattice structure with stoichiometric composition Ni_3Nb. Prolonged exposure of the material to temperatures in the range of 650-900°C leads to the transformation of γ" to δ phase, thereby depleting the matrix of γ" strengthening phase. The precipitate has a disk-shaped morphology with thickness ~ 10nm and diameter of ~ 50nm and has the <001>$_{\gamma"}$//<001>$_{\gamma}$ and <100>$_{\gamma"}$//<100>$_{\gamma}$ orientation relationship with the matrix[18].
δ **phase** forms on prolonged thermal exposure of γ" phase, it has a $D0_a$ orthorhombic lattice structure and is incoherent with the matrix. The strength of the material does not increase in the presence of the δ phase as it is incoherent, however the increased quantity of the δ phase can lead to severe degradation of properties. The precipitate has needle-like or globular morphology and has a solvus temperature of ~1000 °C[18].
Laves Phase is a topologically close-packed structure having C_{14} hexagonal lattice structure with the chemical formula $(Fe,Ni,Cr)_2(Nb,Ti)$. The precipitation of Laves phase occurs by the segregation of Nb or Ti in the interdendritic regions during solidification, which leads to a depletion of Nb in the matrix needed for the precipitation of strengthening phases. The Nb depleted regions serve as the crack initiation and propagation sites resulting in poor tensile strength and ductility. It is possible to eliminate Laves phase by homogenisation treatments above 1160°C, which allows for the back diffusion of segregated Nb[20, 21].
MC carbides similar to Laves phase are discrete blocky particles formed in the interdendritic region due to the segregation of Nb and Ti. It forms during the solidification stage

and is distributed heterogeneously through the alloy. MC is considered as a primary carbide and its role in strengthening is indirect, i.e. it provides carbon for the precipitation of secondary carbides such as $M_{23}C_6$ carbide which in a polycrystalline material serves as pinning points for the grain boundaries and prevents grain boundary sliding thus enhancing the rupture strength[18]. MC carbides on the other hand act as the crack initiation and crack propagation path during fracture making them an undesirable phase.

Microstructure of As-processed Inconel 718
In the as-processed state of the wrought and cast material, the microstructure consists of segregation and undesirable phases, like the δ phase or Laves phase. Figure 2.4 a) and b) shows a typical as-cast microstructure with macro-segregation in the interdendritic regions, this is due to the rejection of heavy elements like Nb, W, Mo and Ti from the matrix during the solidification process.

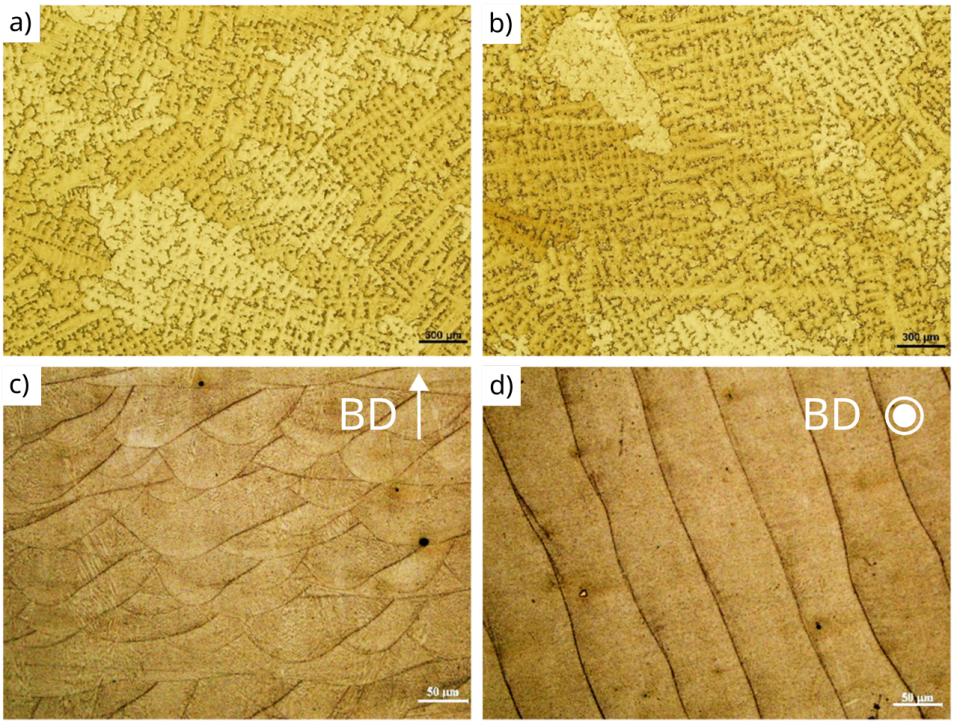

Figure 2.4: Microstructure of as-cast Inconel 718 a) transverse direction b) vertical direction and L-PBF Inconel 718 c)parallel to the building direction d)transverse to the building direction. Reproduced from [22]

The microstructure of L-PBF produced Inconel 718 is distinct from the cast or wrought components: on a macro scale it shows melt pool boundaries along the build direction and scan tracks in the transverse direction. The rapid cooling inherent to the process induces epitaxial growth of fine columnar dendritic structures across the melt pool boundaries. At high magnification (Figure 2.5 c, d), the dendritic structure is clearly visible (yellow arrows show the direction of dendrite growth) with Laves phase precipitated in the interdendritic region. The excess Nb segregation also leads to the formation of δ precipitates in the interdendritic region[23].

Microstructure of post-process heat treated Inconel 718
Post-processing treatments are often required to tailor the microstructure of as-processed

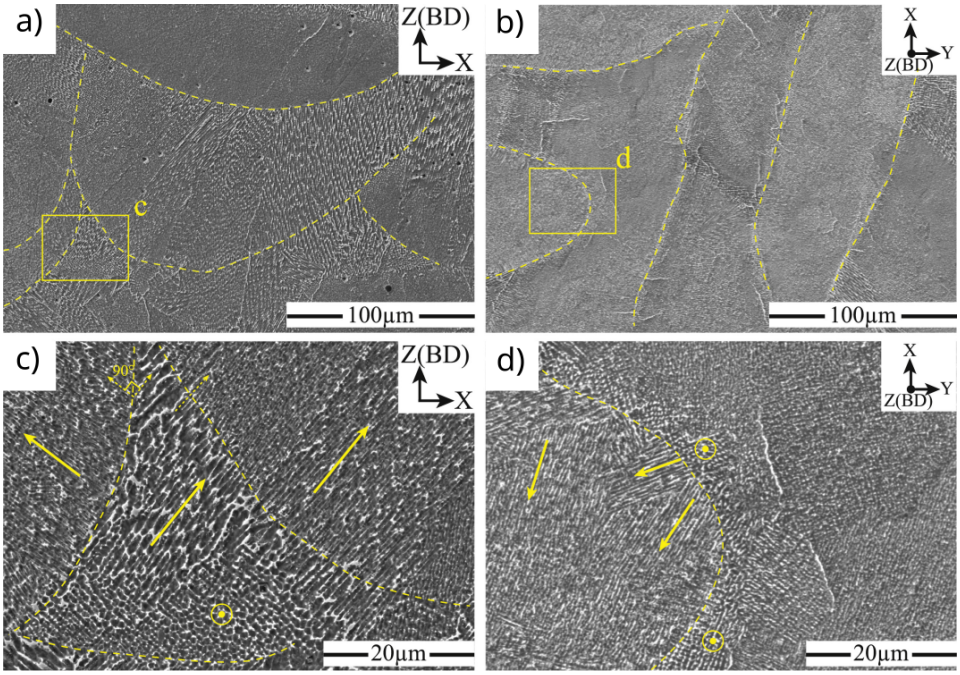

Figure 2.5: Microstructure of L-PBF produced Inconel 718 at high magnification a) parallel to build direction b) perpendicular to build direction. (c) and (d) are the magnified areas marked in (a) and (b) respectively. Arrows indicate dendrite growth direction. Reproduced from [24]

components. As there is a need for stringent control of properties for most applications, standard heat treatments (Table 2.2) have been developed after extensive research. The choice of heat treatments is dependent on the mode of production and the required final properties. For wrought components solutionising heat treatment (SA) at nearly 980°C, for dissolving the existing precipitates, followed by double ageing (DA) for the nucleation and growth of γ' and γ" in a controlled manner is done[19, 25].

In components produced by casting, segregation of elements occurs during solidification making it necessary to homogenise the element distribution before SA and DA. This is done by holding it at elevated temperatures (~1060°C), to allow diffusion of elements, for a period of time and is referred to as homogenisation heat treatment (HSA). The ageing temperature and time are chosen using the time temperature transformation (TTT) diagram (Figure 2.6)[26], the first ageing treatment (at ~720°C) is aimed to precipitate the strengthening phases and the temperature is slightly higher than the second ageing treatment (~ 620°C) where coarsening of the precipitates occur. It can be seen that holding for a longer duration in the first ageing treatment could lead to the formation of the δ phase at the expense of the γ" phase.

A typical microstructure of conventionally produced Inconel 718 post heat treatment is as shown in Figure 2.7, γ' and γ" precipitates can be seen in the matrix and δ phase on the grain boundaries. δ phase in moderate amounts promote grain boundary pinning which improves the high-temperature properties[30]. The beneficial effects of the δ phase also depend on the morphology of the precipitates, acicular shaped precipitate is found to show lower ductility than particle shaped. Hence, an appropriate choice of heat treatment is required to allows for the control of the phases present in the material and this is based on the necessary properties for the end application.

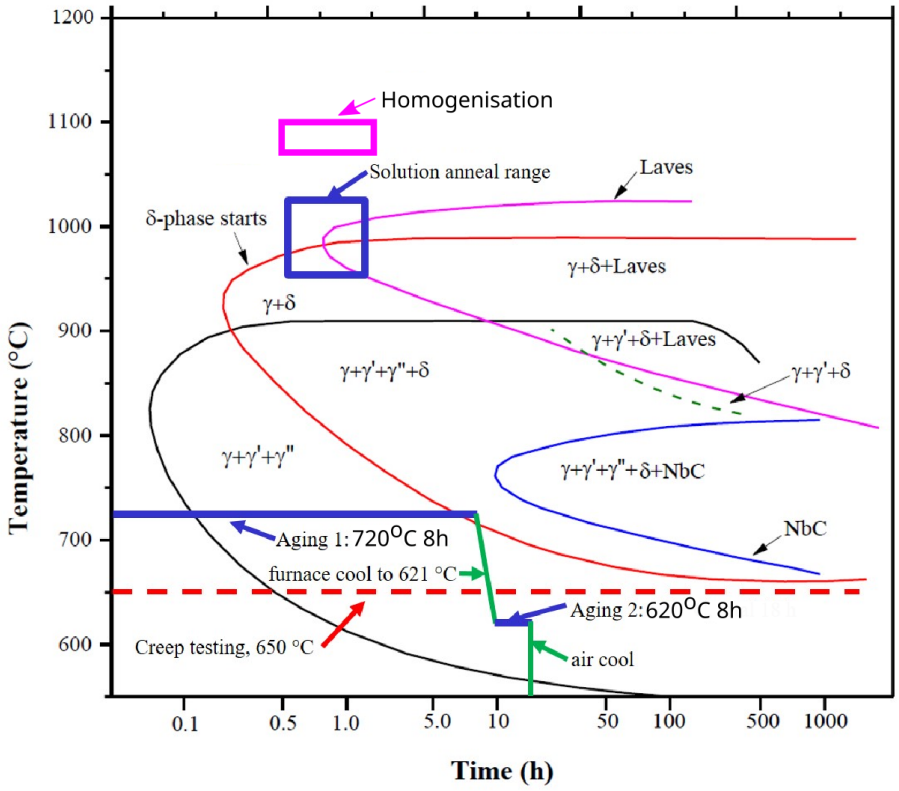

Figure 2.6: TTT diagram of Inconel 718. Reproduced from [26]

Table 2.2: Standard heat treatments for Inconel 718 as per SAE(Society of Automotive Engineers[27, 28, 29].)

Standard	Heat Treatment	Temperature	Holding Time	Cooling
AMS 5663 [27]	Solutionising	980°C	1 h	AC
	Ageing	720°C	8h	FC to 620°C @55°C/h
		620°C	8h	AC
AMS 5383 [28]	Homogenisation	1080°C°C	1.5h	AC
	Solutionising	980°C	1 h	AC
	Ageing	720°C	8h	FC to 620°C @55°C/h
		620°C	8h	AC
AMS 5664E [29]	HIP	1180°C @ 150MPa	3h	FC
	Homogenisation	1065°C	1.5h	AC
	Ageing	720°C	8h	FC to 620°C @55°C/h
		620°C	8h	AC

AC - Air Cooling, FC-Furnace Cooling, HIP-Hot isostatic Pressing

Similar to conventional components, post-processing heat treatment is required for L-PBF components to dissolve the Laves and δ phase and also to precipitate the strengthening phases[17]. Zhang et al.[25] studied the effect of standard heat treatments on L-PBF produced samples and found that homogenisation at 1080°C before solutionising (980°C) and double ageing led to a lower fraction of δ phase. This is because at 1080°C there is a strong driving force for the diffusion of Nb thus homogeneously distributing it in the matrix. Homogenisation and solution heat treatments are found to also induce partial re-

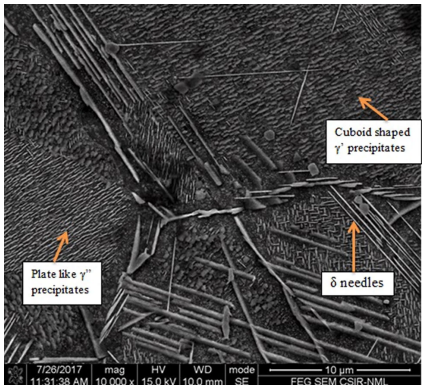

Figure 2.7: Microstructure of conventional Inconel 718 showing the different phases. Reproduced from [31]

crystallisation, the residual stress is believed to provide the driving force for recrystallisation[25], with the former showing more extensive recrystallisation[17]. Figure 2.8 shows the microstructure after homogenisation at 1065°C for 1.5 hr followed by double ageing heat treatment.

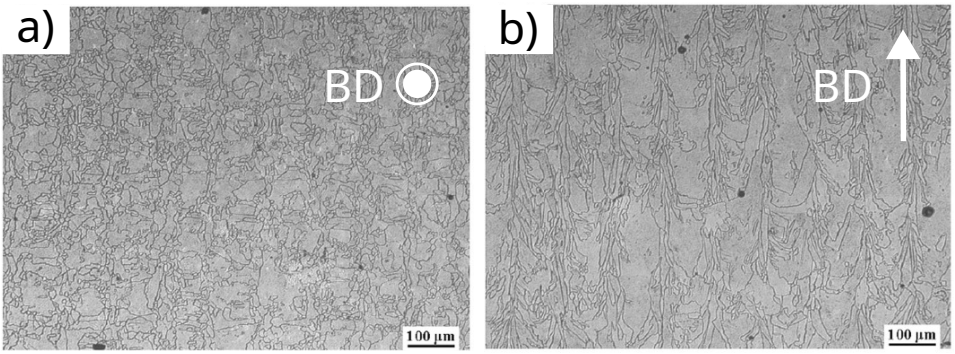

Figure 2.8: Microstructure of L-PBF produced Inconel 718 after homogenisation and double ageing a) perpendicular to build direction b) parallel to build direction. Reproduced from [32]

Hot Isostatic Pressing (HIP) is another post-processing treatment employed to reduce porosity by exposing the component to high temperature(1150-1280°C) and pressure(100-200MPa). HIP treatment alters the microstructure by inducing complete recrystallisation and dissolving Laves and δ phase. Some researchers studied direct ageing of the as-built samples and noted that the strengthening phases γ' and γ" precipitated, as the matrix is in the supersaturated state, without affecting the columnar structures and maintaining the melt pool boundaries[33, 34, 23]. This however is not preferred as the Laves and δ phase remain in the interdendritic region which affects the mechanical properties.

The directional cooling present in the L-PBF process also leads to the development of texture in the components[17], being an FCC phase the preferred growth direction is the <001> crystallographic direction which often forms in the direction parallel to build direction. By varying the process parameters, like laser powder density and scanning strategy, it is possible to tailor the texture or minimise it in the components[35].

2.1.3. Mechanical Properties

The room temperature tensile properties of conventional and L-PBF produced Inconel 718 are given in Table 2.3, the as-built L-PBF samples are found to have strength lower than the conventional counterpart while the ductility is higher[25, 33, 30]. This is because of the absence of strengthening phases in the as-built condition. Inconel 718 is designed such that multiple hardening mechanisms, like strain hardening, solid solution hardening and precipitation hardening, occur simultaneously to enhance its properties. The initial microstructure obtained in the L-PBF process does not contain any precipitation strengthening phases thus lowering the strength, however lower precipitates mean the dislocation can move more freely thus allowing for more deformation hence higher ductility[36]. Post heat treatment the tensile properties are comparable or higher than the conventional counterparts due to the precipitation of strengthening phases, the enhanced properties are attributed to the fine microstructure produced by the L-PBF process[37].

Some researchers argue that to optimise the properties of the L-PBF produced samples conventional heat treatments are not effective and that the heat treatment parameters need to be tailored[38, 39, 40]. Schneider et al. [38] observed that with optimised L-PBF process parameters DA heat treatment alone could enhance the tensile properties while SA or HSA did not improve it further. Huang et al.[39] attributes the enhanced strength of the DA sample to the high dislocation density that remains due to the low heat treatment temperature, however the ductility is considerably lowered as the Laves phase are not dissolved during the DA heat treatment. Zhang et al.[41] performed a similar study also including the effect of part orientation, it was shown that though DA showed similar tensile properties to HSA there was a difference of 114MPa between the DA horizontal and vertical samples, almost the same as the as-built samples, whereas the difference was only 48MPa in HSA samples.

A large scatter in tensile properties is observed in the literature, as seen in Table 2.3, this is majorly due to the differences in the process parameters. Apart from process parameters, the powder production route is also found to influence the tensile properties, Zhao et al.[43] studied Inconel 718 components produced from two different powders production routes. It was seen that components produced from gas atomised powder demonstrated higher porosity leading to an inferior mechanical property compared with plasma rotation electrode preparation (PREP) powders. Similar studies were done on reused powder and found that reusing powder leads to an increase in powder size nevertheless does not alter the chemical composition[44]. Up to 14 times of reuse, no impact on mechanical properties is observed[45, 46], however the experiments are restricted to static properties, i.e tensile tests. Further studies are needed to understand how powder properties affect the dynamic and environmental properties of L-PBF components.

Defects like porosity, anisotropy and residual stress strongly influence the tensile properties and are a major concern in the L-PBF process. Extensive studies have been done to minimise them in the Inconel 718 components[47, 48, 49, 50, 51], HIP treatment is found to reduce porosity considerably and by optimizing the scanning strategy and post heat treatment at elevated temperature it is possible to reduce the residual stress and anisotropy in the components.

2.2. Hydrogen Embrittlement

The presence of hydrogen in Inconel 718 detrimentally affects its mechanical properties[52, 53, 54]. However, the extent of embrittlement depends on the microstructure and environ-

Table 2.3: Tensile Properties of Inconel 718

Orientation	Heat treatment			Ys	UTS	Elongation	Reference
	Homogenisation	Solutionising	Double Ageing*	MPa	MPa	%	
H	-	-	-	849	1126	22.8	[25]
	1080°C,1.5h,AC	980°C,1h,AC	720°C,8h,FC,620°C,8h,AC	1046	1371	12.3	
		980°C,1h,AC	720°C,8h,FC,620°C,8h,AC	1084	1371	10.1	
A (0) -V	-	-	-	572	904	19	[33]
B(90)- H	-	-	-	643	991	13	
C(45)	-	-	-	590	954	20	
D(45x45)	-	-	-	723	1117	16	
A (0) -V	-	1100°C,1h,WC	720°C,8h,FC,620°C,10h,AC,	1074	1320	19	
B(90)- H	-			1159	1377	8	
C(45)	-			1152	1371	15	
D(45x45+)	-			1241	1457	14	
-	-	-	-	848	1126	22.8	[30]
	-	980°C 1hr,FC	720°C,8h,FC,620°C,8h,FC	1084	1370	10.1	
	-	1080°C,1hr,FC	720°C,8h,FC,620°C,8h,FC	1173	1450	13.5	
	1080°C,1.5h,FC	980°C,1hr,FC	720°C,8h,FC,620°C,8h,FC	1046	1370	12.3	
Wrought	-	980°C,1h,AC	720°C,8h,FC,620°C,8h,AC	1030	1280	12	
45x45	-	-	-	760	1335	21.3	[40]
	-	980°C 1hr	720°C,8h,FC, 620°C,8h,AC	1240	1560	11.6	
	-	-	720°C,24h,AC	1300	1580	9.6	
	-	1020°C,0.25h,WQ	720°C,24h,AC	1245	1640	16.6	
Wrought		980°C,1h,AC	720°C,8h,FC,620°C,8h,AC	1034	1276	12	[42]
Cast	1080°C,1.5h,AC	980°C,1h,AC	720°C,8h,FC,620°C,8h,AC	758	862	5	[28]

FC - Furnace cooling, AC - air cooling, WC - water cooling, V - vertical, H - horizontal

* FC from 720°C to 620°C is done at 55°C/h

+ 45x45 signifies 45°from horizontal and 45°from vertical

mental conditions. To better understand it it is necessary to know how hydrogen transports and interacts with the material. Hence, in the following sections; hydrogen transport, HE mechanisms and state-of-the-art testing methodologies for HE would be discussed.

2.2.1. Hydrogen Transport

The first stage of HE is the introduction of hydrogen into the material. This occurs through complex surface reactions, which depend on the hydrogen environments: gaseous or electrolyte. The surface reactions lead to the adsorption of atomic hydrogen into the surface and sub-surface of the material. The hydrogen then diffuses to the bulk due to the concentration gradient within the material. It should be noted that the main focus of the study is gaseous hydrogen embrittlement and the following sub-sections: entry, diffusion and effect of hydrogen traps in Inconel 718 are explained with this in mind. A brief description of electrochemical hydrogen embrittlement is also done for comparison when necessary.

Hydrogen Entry

Gaseous Hydrogen

Entry of gaseous hydrogen into a metal occurs in three steps: physisorption, chemisorption and absorption[55]. Physisorption involves Van der Waals interactions with the surface and hydrogen molecules(reversible process). It is followed by chemisorption: hydrogen molecule dissociates into atomic hydrogen and adsorbs onto the surface. This is a slow process owing to the high dissociation energy of hydrogen (4.47eV) and high adsorption energy (40-160 kJ mol^{-1})[56]. The chemically absorbed hydrogen atoms then diffuse into the bulk due to the hydrogen concentration gradient within the material. The equilibrium

concentration of hydrogen dissolved in a metal (C_L) for a given hydrogen partial pressure is (P_{H_2}) is determined by Sievert's law[57], represented with the equation:

$$C_L = K_L\sqrt{P_{H_2}} \tag{2.2}$$

where K_L is the hydrogen solubility in mass ppm/MPa$^{1/2}$ following Arrhenius-type equation ($K_L = K_0 e^{\frac{-\Delta H_S}{RT}}$), where K_0 is solubility constant, ΔH_S is dissolution enthalpy in J mol^{-1}, R is the universal Gas constant (8.314J mol^{-1} K^{-1}), T is the absolute temperature in K.

Hydrogen from Corrosion
Under certain environmental conditions hydrogen ions are formed on the metal surface due to corrosion reactions. The hydrogen ions that come from the partial reaction can either combine to form hydrogen gas or can enter into the metal through hydrogen absorption reactions[55]. The reactions occurring in acidic and alkaline medium is as given in Equation 2.3 and Equation 2.4, where $M \cdot H_{ads}$ represents adsorbed hydrogen atom on metal. The surface reactions occurring before absorption of hydrogen into bulk is quite complex and is not in the scope of this study, hence will not be discussed here. The hydrogen absorbed into the metal then diffuses into the bulk similar to the situation of gaseous hydrogen, this process continues till the solubility limit of Inconel 718 is reached, after which gas bubbles form on the surface.

$$H_3O^+ + M + e^- \rightarrow M \cdot H_{ads} + H_2O(\text{in acidic solution}) \tag{2.3}$$

$$H_2O + M + e^- \rightarrow M \cdot H_{ads} + OH^-(\text{in basic solution}) \tag{2.4}$$

These reactions are emulated in a laboratory using an electrochemical cell to study HE, it will be further elaborated later on.

Hydrogen Diffusion
Diffusivity is a measure of how fast the hydrogen atoms diffuse in a metal. It is a thermally activated process and can be expressed as[58]:

$$D = D_0 e^{\left(\frac{-H_D}{RT}\right)} \tag{2.5}$$

where D_0 is a constant in m^{2}s^{-1}, H_D is activation energy for diffusion, R is universal gas constant and T is temperature in K. The activation energy for diffusion is dependent on the type of lattice structure. In an fcc lattice such as Inconel 718, the hydrogen atom occupies the octahedral interstitial sites as it has the largest available interstitial volume, thereby minimising the lattice distortion. The diffusion of hydrogen from one octahedral site to other proceeds with an intermediate jump to a tetrahedral site. This is because the jump with an intermediate step has a lower energy barrier than a direct jump to an octahedral site [59].

He et al.[59] did first-principle calculations to determine the diffusivities of hydrogen in different Fe lattices, namely α-Fe, γ-Fe and ϵ-Fe, and found that the diffusion rates followed the order $D_{bcc} > D_{fcc} > D_{hcp}$. However, the values obtained deviated from the experimental observations because of not accounting for the lattice imperfections in the first principle calculations. Lattice defects like grain boundaries, vacancies, interface etc. act as hydrogen

traps preventing hydrogen atoms from further diffusion, thus leading to increased hydrogen concentration and lower hydrogen diffusivity measured in experiments[60, 58]. The values obtained in practical experiments are referred to as effective diffusivity. For Inconel 718, D_0 has a reported range of 1.6 - 6.16 $\times 10^{-7} m^2/s$[61].

Hydrogen Traps

Traps can be considered as locations in the lattice where hydrogen is immobilised and requires higher energy to participate again in diffusion, generally, these locations are lattice defects like grain boundaries, vacancies, interfaces, inclusion and so on(Figure 2.9). The binding energy of traps defines the characteristics of the trap, it is generally classified into reversible and irreversible hydrogen traps. Reversible traps have low binding energies (<60kJ mol^{-1}) whereas irreversible traps have high binding energies (>60kJ mol^{-1}). Irreversible traps cause a decrease in apparent diffusivity as they act as sinks for hydrogen. Nevertheless, this is relative as at elevated temperatures irreversible traps can become reversible traps[62]. A schematic of the available trapping sites in a metal is shown in Figure 2.9. Thermal Desorption Spectroscopy is the method commonly employed to determine the binding energies of various traps, the increasing order of strength of the traps determined by Lynch[63] is as given below:

1. Solute atoms
2. Free surface and sites between few atomic layers below surface
3. Vacancies
4. Dislocation cores
5. Grain boundaries
6. Precipitate/ matrix interface
7. Inclusion/matrix interface
8. Voids and internal cracks

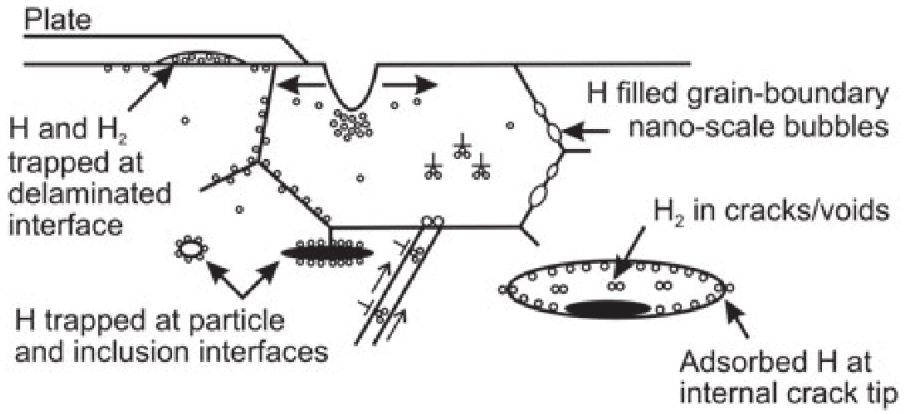

Figure 2.9: Schematic of hydrogen trapping sites in a metal at a micro-scale. Reproduced from [63]

In the case of Ni-based alloys, the carbonitride and δ phase are the primary trap sites and have binding energies in the range of 30-87 kJ/mol[64].

2.2.2. Hydrogen Embrittlement Mechanism

Various models like hydrogen enhanced localised plasticity (HELP), hydrogen enhanced decohesion (HEDE), hydride formation and fracture, and adsorption induced dislocation emission (AIDE) have been proposed to understand the deformation mechanisms in metals in the presence of hydrogen [63]. It is noted that there is a competition between different mechanisms and the one that dominates depends on the existing conditions[65]. In Inconel 718 HEDE and HELP are the majorly reported mechanisms, AIDE is not commonly reported as most experiments are performed ex-situ after pre-charging[66, 52]. In this section, the models are briefly summarised, for a detailed explanation the reader can refer [63, 65].

Hydrogen Enhanced Decohesion

HEDE involves sequential tensile separation of atoms in preference to slip due to weakening of interatomic bonds due to adsorption of hydrogen as shown in Figure 2.10[63]. Strain-gradient hardening could increase the concentration of hydrogen ahead of the crack due to very high elastic stresses. The presence of hydrogen weakens the bond by decreasing the electron charge density between metal-metal atoms. Nevertheless, a direct experimental evidence for the mechanism is difficult to obtain.

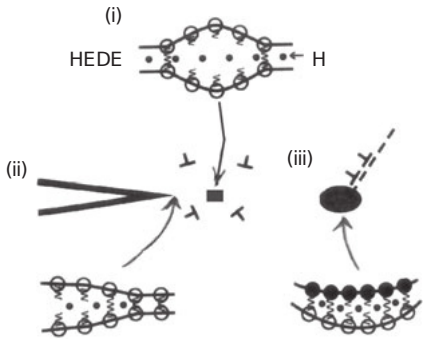

Figure 2.10: HEDE mechanism, Weakening of interatomic bonds leading to tensile separation of atoms by (i) hydrogen in lattice (ii) adsorbed hydrogen (iii) hydrogen at particle-matrix interface. Reproduced from [63]

Hydrogen Enhanced Localised Plasticity

HELP is based on the observation that the presence of solute hydrogen facilitated the movement of dislocations. Localised hydrogen concentration is observed near to crack tip and this is a result of either hydrostatic stresses in front of the crack tip or hydrogen entry at the crack tip[63]. This leads to localised deformation in front of the crack tip as shown in Figure 2.11. In-situ transmission electron microscopy study of thin foils in hydrogen environment shows dislocation motion at lower stress states supporting the hydrogen dislocation interaction theory[65].

Adsorption Induced Dislocation Emission

In the AIDE model, it is proposed that adsorption of hydrogen onto the surface facilitates the nucleation of dislocations[63]. This is attributed to the weakening of atomic bonds by adsorbed hydrogen enabling dislocation emission from the crack tip. Increase in dislocation activity leads to crack growth as the number of dislocations on suitably inclined slips

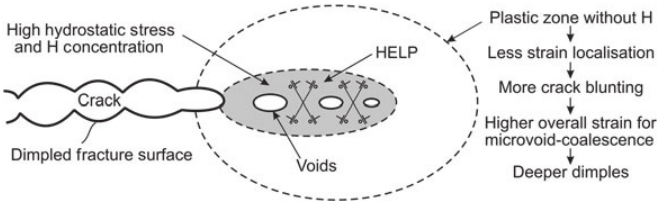

Figure 2.11: Schematic of HELP mechanism. Reproduced from [63]

planes also increases. The crack coalesce with voids at a lower strain giving rise to shallow dimples in comparison to ductile failure on the fracture surface[65].

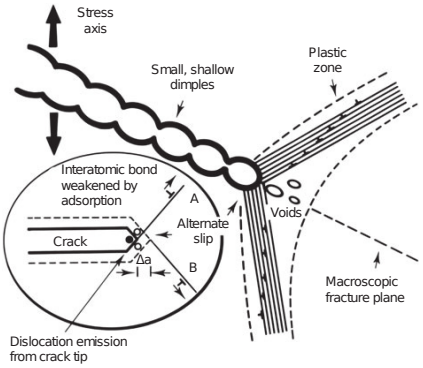

Figure 2.12: Schematic of AIDE mechanism. Reproduced from [63]

2.2.3. Characterisation of Hydrogen Embrittlement

Characterisation of hydrogen embrittlement involves exposing Inconel 718 to hydrogen environments and performing tensile tests. On a laboratory scale, hydrogen is introduced into the material by artificial pre-charging (gaseous or electrochemical means) before testing or in-situ hydrogen environment during testing. Pre-charging of hydrogen into the sample is representative of the internal hydrogen effect, whereas the in-situ hydrogen environment is representative of the external hydrogen effect. The effect of hydrogen is found to be more pronounced at strain rates of 10^{-5} /s and negligible for strain rates higher than 10^{-3} /s[66]. This is because at fast strain rates the hydrogen diffusion is not fast enough to reach ahead of the crack interact with it. Hence, slow strain rate tensile tests are conducted with strain rate in the range of 10^{-3} - 10^{-5} /s to quantify the degree of hydrogen embrittlement. In the following sections different charging methods, effect of charging methods and slow strain rate tensile test of Inconel 718 is discussed.

Electrochemical Pre-charging

As explained earlier electrochemical pre-charging involves introducing hydrogen by electrochemical reactions at the surface of the sample. The sample is set as a cathode in an electrochemical cell and constant current or potential is applied. The protons (H^+ ions) present in the electrolyte adsorb onto the metal surface and diffuse to the bulk. The hydrogen concentration is varied by changing the composition of the solution, charging current, charging potential or charging time. Researchers have found that generally the concentration is given by[56]:

$$C_H = K\sqrt{i} \tag{2.6}$$

where C_h is the concentration of hydrogen, K is a constant and i is charging current density. It is found that electrochemical pre-charging gives high effective pressure on the sample surface leading to a higher hydrogen concentration and also to surface cracking and phase transformation[67]. Compounds like As_2O_3 or NH_4SCN (referred to as poison) is added into the electrolyte to prevent the formation of H_2 gas at the electrodes thereby preventing surface damage. This test conditions represent the worst-case scenario that might occur due to HE.

Thermal Pre-charging

Thermal pre-charging involves exposing the specimens to high-pressure hydrogen gas at elevated temperatures in an enclosure. The high temperature allows for the faster diffusion of hydrogen into the specimen after adsorption occurs and obtain homogeneous distribution in a shorter time scale of days. This is useful especially for materials with fcc matrix phase, as diffusion is very slow at room temperatures. The temperature is usually in the range of 200-350°C so that there are no microstructural changes in the specimen. By choosing a suitable pressure and temperature it is possible to produce hydrogen concentration representative of gaseous hydrogen service[67]. Marchi et al.[68] found that for 22Cr-13Ni-5Mn austenitic stainless steel (fcc matrix) pre-charging at 138MPa and 573 K for 10 days gave a uniformly supersaturated hydrogen concentration in specimens of diameter 4mm.

In-situ Gaseous Hydrogen Charging

External hydrogen testing closely replicates the actual working environment of hydrogen pressure vessels, pipelines and so on. However, due to the safety precautions required the experimental setup is quite sophisticated. As per ASTM-G142[69], the testing is done in an autoclave with high purity hydrogen gas under pressure.To maintain high hydrogen gas purity during the testing the enclosure is purged with pure helium(99.9%) twice and then purged with high purity hydrogen gas (99%) at least thrice before the start of the test. Hydrogen gas pressure, gas purity and testing temperatures strongly influence the results, hence stringent control of these parameters are needed to obtain reliable results. The surface kinetics and hydrogen uptake into the material are affected by the hydrogen gas pressure and testing temperature, it is generally observed that as the pressure increases susceptibility to HE also increases[70]. The temperature on the other hand has many effects on the hydrogen-metal interactions like surface reaction, dissolution, diffusion and so on. Due to the need for sophisticated setups not much literature is available for Inconel 718 in in-situ testing conditions. Boot et al.[71] developed a test setup that does not require a sophisticated and expensive setup to perform in-situ hydrogen testing. This was done by using a hollow specimen and exposing the interior of the sample to high-pressure hydrogen gas as shown in Figure 2.13.

Effect of Charging method

The mechanisms leading to HE in both internal hydrogen and external hydrogen are the same[72, 73]. However, in order to obtain realistic experimental results, the method of testing needs to be carefully chosen based on the practical scenario that is being emulated. Internal hydrogen testing closely represents the cases where the material is not in a hydrogen gas environment but hydrogen is introduced during processes like electroplating solutions, cathodic cleaning, welding in moist atmospheres and so forth[63]. The hydrogen atom dif-

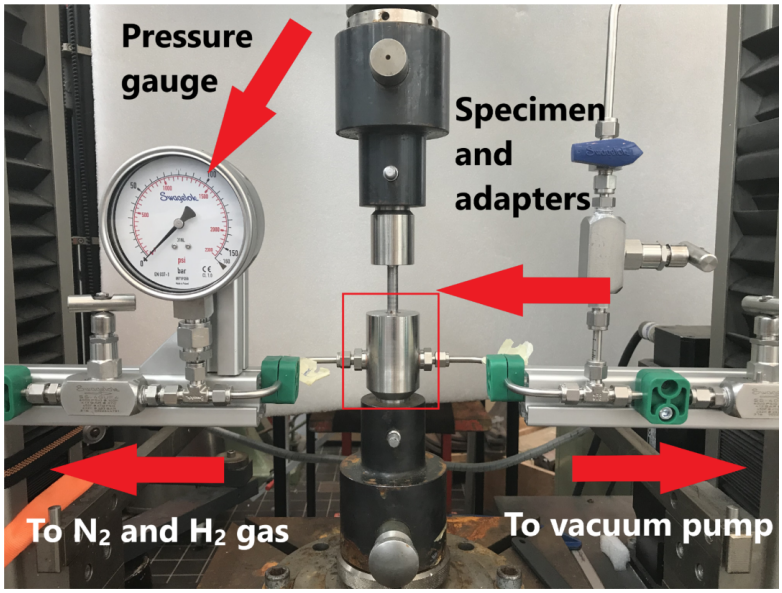

Figure 2.13: Laboratory in-situ gaseous hydrogen setup that does not require autoclave. Reproduced from [71]

fuses into the bulk of the material leading to HE. External hydrogen testing is often done to replicate scenarios of materials exposed to hydrogen gas under load (hydrogen gas storage or hydrogen gas transport).

Apart from the similarity in the HE mechanism, the concentration of hydrogen introduced in the test samples differs for each testing method. Zhao et al.[74] found that electrochemical charging led to a hydrogen concentration of 3.94 weight ppm whereas gaseous charging only showed 0.24 weight ppm in steels. This difference in hydrogen concentration can lead to varying degrees of HE during testing. In external hydrogen testing, the hydrogen is introduced into the specimen during the test, making it highly sensitive to strain rates. A key limitation in external hydrogen testing is that HE can be kinetically limited by hydrogen adsorption, i.e. hydrogen adsorption might not be fast enough to supply hydrogen ahead of the crack tip. This is not the case in practical situations where there is sufficient time to reach the hydrogen concentration needed to cause HE. Hence, it is not advisable to have a quantitative comparison with test results obtained from different testing methods; though the basic trends like the temperature at which the ductility is minimum for a material remain the same.

Slow Strain Rate Tensile Test (SSRT)

To characterise the effect of hydrogen on mechanical properties slow strain rate tensile (SSRT) tests are used with a strain rate of 10^{-5} /s[66]. The SSRT test results of conventional and L-PBF produced Inconel 718 are given in Table 2.4 for the uncharged condition (UC) and electrochemical hydrogen charged (HC). It can be seen that there is a loss of ductility in the presence of hydrogen; whereas no softening or hardening is observed i.e. there is no change in the yield strength. The slow strain rate tensile test results of conventional and L-PBF produced Inconel 718 are given in Table 2.4 for hydrogen charged and the uncharged condition. It can be seen that there is a loss of ductility in the presence of hydrogen; whereas no softening or hardening is observed i.e. there is no change in the yield strength.

Table 2.4: HE behaviour of Inconel 718 produced by L-PBF after cathodic charging of the samples

Processing	Orientation	Heat Treatment	Specimen Condition	Ys(MPa)	UTS(MPa)	$\epsilon_{(f,h)}/\epsilon_{(f,0)}$	C_H	Reference
L-PBF		-	UC	721		0.77	-	
			HC	~721			-	
L-PBF + DA	Horizontal	720C 8h + furnace Cooling 50C/h + 620C8h	UC	1215		0.41	-	[75]
			HC	~1215			-	
L-PBF + HA		1150C 2h + 720C 8h + furnace Cooling 50C/h + 620C8h	UC	1098		0.65	-	
			HC	~1098			-	
Wrought (age hard--ened to 36 HRC)		NA	UC	898	1170	0.42	-	
			HC				-	
L-PBF + HT	Vertical	1030C, 1 h 55 m + 783 °C for 6 h 45 m, argon gas quenched	UC	1048	1255	0.53	-	[75]
			HC				-	
	Horizontal		UC	1119	1349	0.23	-	
			HC				-	
L-PBF	Horizontal	1100C,1.5 h,AC +960C,1 h,AC +720C,8 h,FC + 620C,8 h,AC	UC	737	1078	0.72	-	[76]
			HC	647	897		-	
L-PBF + HT			UC	1260	1475	0.62	-	
			HC	1196	1353		-	
L-PBF	Vertical		UC				-	[77]
			HC			0.77	2.7	
			HC			0.85	3.9	
			HC			0.85	4.8	
			HC			0.71	7.2	
			HC			0.65	7.8	
			HC			0.52	17.4	
			HC			0.45	28	

Ys and UTS are approx as they are extrapolated from the graphs provided in the references

HT - Heat treatment, V - vertical, Hz1 - horizontal with short side parallel to build direction, hz2 - horizontal with long side parallel to build direction

FC - Furnace cooling, AC - air cooling, DA - Direct Ageing, HA - homogenisation+ageing

HC - Hydrogen charged, UC - Uncharged specimen

$\epsilon_{(f,0)}$ - elongation at failure in ambient condition

$\epsilon_{(f,h)}$ - elongation at failure in hydrogen environment

C_H - Hydrogen concentration reported

The mechanisms used to explain hydrogen embrittlement in Inconel 718 are Hydrogen Enhanced Localised Plasticity (HELP) and Hydrogen Enhanced Decohesion (HEDE)[78]. As discussed earlier, the presence of hydrogen increases the mobility of dislocation and stabilises the edge component of the dislocation thus locally increasing plasticity. This is not visible in Inconel 718 as the fracture surface shows brittle transgranular features in the presence of hydrogen as shown in Figure 2.14[52]. On taking a closer look, a large number of dislocation slip bands are visible on the cleaved surface and it is believed that the nucleation of cracks occurs at the intersection of these slip bands and propagates along them[52]. Various studies have found that the presence of secondary phases increases the susceptibility of Inconel 718 to HE, among them δ phase is found to be the most detrimental[78, 79, 53, 80]. It is proposed that the weak binding energy of hydrogen to the δ phase leads to the segregation of hydrogen at the interface of the matrix and the δ phase resulting in decohesion. First-principle calculations of the influence of hydrogen in the lattice have shown that the cohesive energy of grain boundaries decreased by ~40% signifying the possibility of HEDE mechanism[78]. The HE behaviour of Inconel 718 is believed to be a result of a complex interaction between HEDE and HELP mechanisms.

Only a limited number of literature is available for L-PBF Inconel 718, as it is a more recent technology[75, 81, 76, 77]. The HE behaviour is found to be similar to that of the conventional counterpart, nevertheless, the degree of HE is different depending on the post-processing treatments. Hesketh et al.[81] studied the effect of hydrogen on the part orientation of L-PBF produced samples after non-standard heat treatment (1030°C for 1 hr and aged at 783°C for 6 h 45 m) and also compared with wrought specimen with identical heat treatment. The experiment was conducted with in-situ hydrogen charging by electrochemical means, it was reported that the vertical samples showed higher HE resistance

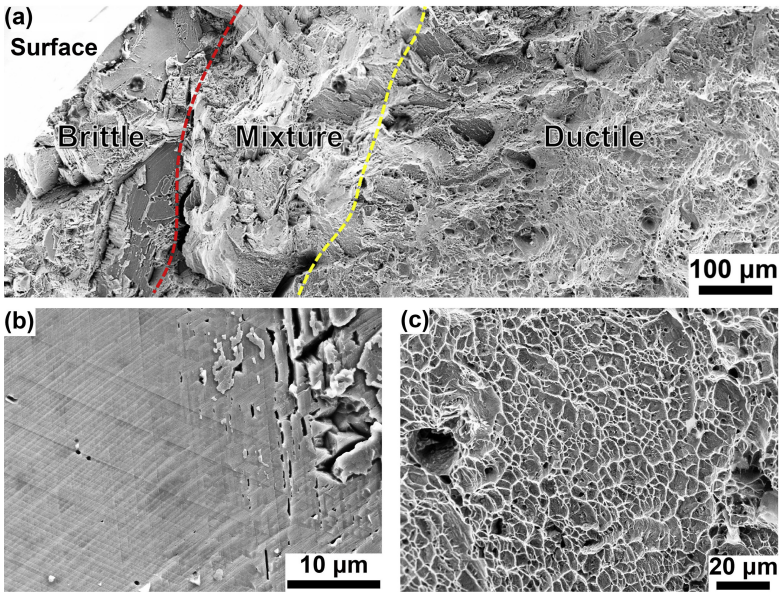

Figure 2.14: Fracture surface of conventional Inconel 718 a)Overview b) brittle region c) ductile region. Reproduced from [52]

compared to the horizontal sample, having higher yield and tensile strength, and wrought samples. This is due to the microstructural differences in the horizontal and vertical samples and the higher strength of horizontal samples leading to higher stress concentrations. From the fractography, Hesketh concludes that the effect of porosity, found to be around 0.18%, is negligible. However, no mention of the effect of residual stress is present which can lead to varying concentrations of hydrogen in the specimen.

Lee et al.[75] studied the effect of solidification sub-structure arising from L-PBF on HE behaviour. This was done by comparing samples subjected to two different heat treatments: Direct Ageing (DA) and Homogenisation + Ageing (HA). DA samples show higher susceptibility to HE because of its higher strength, which leads to higher stress concentration. This is corroborated by Hesketh et al.[81] and Li et al. [76] where higher strength samples demonstrated higher susceptibility to HE. However, the influence of residual stress is not accounted for in the experiments. Lee observed that during HA treatment recrystallisation occurred, which signifies the removal of residual stress. This is not the case in the DA samples, as no recrystallisation occurred. The residual stress could induce a heterogeneous distribution of hydrogen that leads to a local spike in concentration and cause crack initiation at an earlier stage. Apart from this, the microstructural differences in both sets of samples are not accounted for. In addition, due to the difficulty of performing in-situ gaseous charging experiments, only information for tests with electrochemical charging could be found for AM Inconel 718. Among them no studies were found looking into the effect of recycled powder in HE.

2.3. Conclusions and Research Objectives

2.3.1. Conclusions

Based on the literature study performed the following conclusions can be made:

- L-PBF process produces fine microstructure due to the rapid cooling inherent to the

process, with elongated grains along the build direction. This unique microstructure provides good mechanical properties.

- The properties of L-PBF produced Inconel 718 highly depend on the process parameters and careful control of these parameters is required to have reproducible results.
- Variation in powder properties is found to be less influential during testing of static properties. However, the density of components is dependent on the powder production route.
- Conventional heat treatments for L-PBF produced Inconel 718 provide mechanical properties comparable to conventional counterparts. Further enhancement requires optimisation of post-processing heat treatment parameters specific for components produced by the L-PBF process.
- Hydrogen Embrittlement of materials depends on the microstructure of Inconel 718 and the hydrogen charging method used: electrochemical or gaseous.
- Contrasting observations have been reported for HE of L-PBF produced Inconel 718, which results from differences in processing parameters and testing conditions. Currently, no standard exists for processing parameters. The primary goal is to achieve maximum densification.
- Hydrogen embrittlement with respect to defects inherent in the L-PBF process on Inconel 718 is not considered in the literature, such as the influence of porosity and residual stress. Hydrogen can diffuse into the pores and recombine to form H_2 gas, which leads to internal cracks. Residual stress, on the other hand, can influence the distribution of hydrogen within the sample.
- Similarly the influence of powder properties on HE of L-PBF-produced components needs to be looked into, some researchers have found a detrimental effect of using recycled powder on dynamic properties though limited information is available regarding exposure of these specimens to corrosive environments; and no studies were found for gaseous hydrogen environment.
- Most experiments for HE evaluation are done by pre-charging the samples and ex-situ testing in an inert atmosphere, limited literature is available regarding in-situ experiments. As explained earlier different testing methods lead to varying hydrogen concentrations which can cause significant variation in the observed effect of HE.

2.3.2. Research Objective

Gaseous hydrogen embrittlement of 3D-printed Inconel 718 manufactured from sustainable feedstock.

To answer this objective the following research questions were set:

1. To determine the gaseous HE of L-PBF Inconel 718 fabricated from recycled powder.

2. To investigate the effect of process induced microstructural anisotropy on HE of L-PBF Inconel 718.

3. To determine the effect of post processing heat treatment on in-situ hydrogen response of conventional and L-PBF Inconel 718.

4. To study the dominant HE mechanisms in L-PBF Inconel 718.

3

Materials and Methods

3.1. Materials

In this research, hydrogen embrittlement of Inconel 718 processed by Laser powder bed fusion (L-PBF) is studied and compared with its commercial hot rolled counterpart. The conventional hot-rolled samples after heat treatment are supplied by VDM metals GmbH [82] with the composition given in Table 3.1. The heat treatment parameters are given in Table 3.3. The conventional samples represent commercially used Inconel 718 in the industries as per ASTM B 637 standard[83]. The AM samples are fabricated using F3nice Inconel 718 powder produced from recycled materials[84].

Table 3.1: Composition of Inconel 718 obtained from X-Ray fluorescence spectroscopy (XRF).

Sample	**Composition**												
	Ni	**Cr**	**Fe**	**Nb**	**Mo**	**Ti**	**Al**	**Si**	**Mn**	**Mg**	**V**	**Co**	**Cu**
Conventional	54.90	17.55	17.55	4.66	2.86	0.94	0.45	0.09	0.09	-	0.03	0.37	0.15
AM	54.84	18.25	17.4	4.71	3.01	1.09	0.36	0.12	0.11	0.05	0.02	-	-

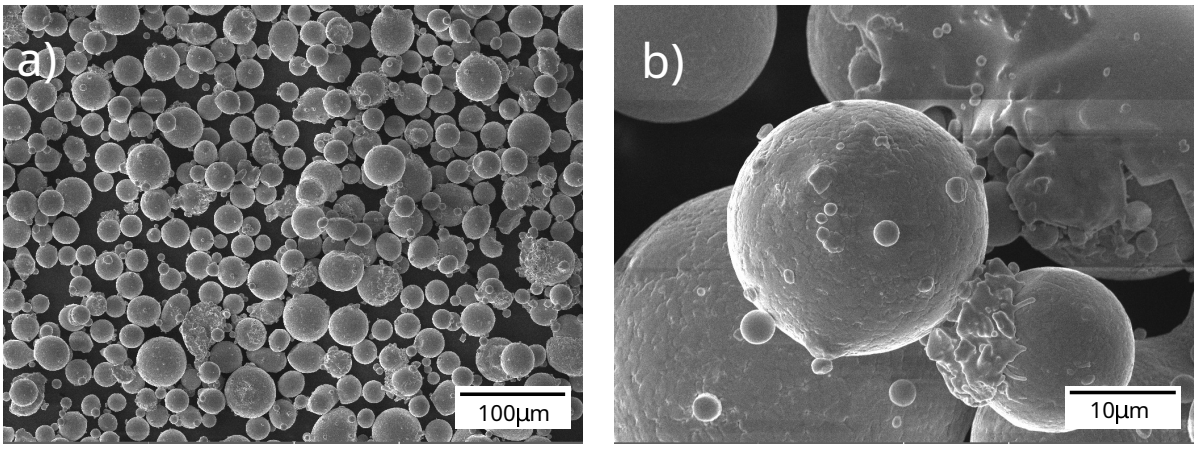

Figure 3.1: a) Powder particles as viewed through an SEM b) high magnification image showing satellite particles on the surface.

The AM samples are manufactured in AMCM M290 (customised EOS M290) machine equipped with 1070 nm wavelength Ytterbium fibre laser. A stripe scanning strategy with

laser power of 285 W is used in combination with 960 mm/s scan speed and 0.11 mm hatch distance to obtain a volumetric energy density (VED) of 67 J/mm^3. To prevent oxidation during the L-PBF process, inert argon gas environment is used. The process parameters are summarised in Table 3.2. The size distribution of recycled powder as per D90, D50 and D10 was found to be 55.5 μm, 36μm, and 23.2μm respectively. D90, D50 and D10 represent that the 90%, 50% and 10% of particles are below the respective sizes. The SEM micrographs showing the particle morphology is given in Figure 3.1. It can be seen that the particles are not completely spherical and satellite particles are present on the surface, which can affect the flowability and packing density. In the current study, significant influence of the morphology is not expected to occur as it adheres to ASTM F3055[85] standard.

Table 3.2: Process parameters used for L-PBF of Inconel 718.

Laser Power (W)	**Scan Speed (mm/s)**	**Hatch Distance (mm)**	**Laser Spot Diameter (μm)**	**Layer Thickness (μm)**	**Volumetric Energy Density (VED) (J/mm^3)**
285	960	0.11	80	40	67

Table 3.3: Post processing heat treatments used for the Inconel 718 samples.

Sample	**Heat Treatment**	**Temperature**	**Holding Time**	**Cooling**
Conventional	Solutionising	1032 °C	1 h	WC
	Aging	791°C	6 h	AC
AM (AMS5663[27])	Solutionising	980 °C	1 h	AC
	Aging	720 °C	8 h	FC to 620 °C @ 55 °C/h
		620 °C	8 h	AC

AC - Air Cooling, FC-Furnace Cooling, WC-Water Cooling

Degree of hydrogen embrittlement (HE) is found to be higher in materials with higher yield strength[86]. So in L-PBF, horizontally built samples are found to be more susceptible to (HE) than vertically built samples[81]. In this research, the hollow cylindrical samples are additively manufactured in the horizontal direction (as shown in Figure 3.2) to evaluate the worst-case scenario. The AM samples are studied both in as-processed and heat treated condition, in the remainder of the thesis they would be referred to as AM-AP and AM-HT respectively. The heat treatment involves solutionising at 980 °C for 1 h followed by double ageing at 720°C for 6 h furnace cooled to 620 °C and held for 10 h. The AM-AP, AM-HT and conventional cylindrical samples are then machined to the required dimensions for mechanical testing.

3.2. Experimental Methods

3.2.1. Microstructural Analysis

For microstructure and porosity analysis the sample surface needs to have a mirror-like appearance (i.e. without any scratches). To achieve this, the region of interest in the samples were identified and then it was cut and mounted in a conductive resin. SiC abrasive papers of increasing grit size (from 80 to 2000) were used to grind the specimens; after which, it was polished using 3μ and 1μ diamond slurry to achieve the mirror-like finish. To reveal the microstructure the specimens were etched with Kalling's reagent (5g $CuCl_2$, 100ml HCl and 100ml ethanol). The microstructure was analysed using Olympus optical microscope

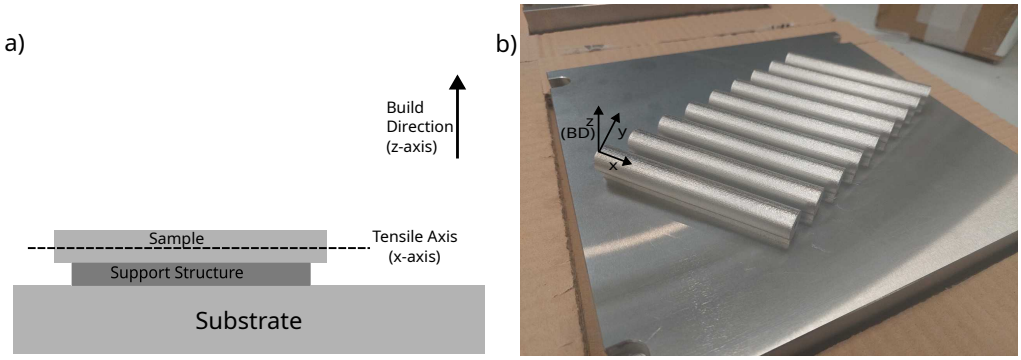

Figure 3.2: a) Sample orientation (horizontal) for the L-PBF process b) AM samples. z-axis is the building direction (BD) and x-axis is the tensile axis.

and to determine the morphology of the precipitates Jeol JSM IT-100 scanning electron microscope (SEM) equipped with energy dispersive spectroscopy (EDS) was used.

For the AM samples, porosity measurement were additionally done on the polished surface using a Keyence VHX-5000 digital microscope. A rectangular region of 2000x2000 μm^2 is defined and the porosity within this region is determined using the area measurement feature. The resolution of the pore size is limited to 1 μm. This is repeated in three different regions and the average porosity is calculated.

Vicker's hardness tests were performed on the samples as a preliminary estimate of mechanical properties. The hardness tests are performed on a Struers Durascan hardness tester with HV5 (5kgf) scale to obtain the average hardness of the material. Five measurements are taken close to the centre of the sample in the direction perpendicular to the tensile axis (XY-plane in Figure 3.2), which is the build direction in the case of the AM samples.

X-Ray Diffraction Analysis (XRD) is done to qualitatively determine the different phases precipitated in the conventional, AM and AM-HT samples. The XRD measurements are performed in a Bruker D8 Advance diffractometer with Co kα radiation. A step size of 0.035° 2θ with 45 kV and 40 mA is used. The peak identification is done in Bruker software Diffrac.EVA.

3.2.2. In-situ Gaseous Hydrogen Mechanical Testing

Test Setup

To characterise the effect of gaseous hydrogen on Inconel 718, the sample design developed by Boot et al. [71] (shown in Figure 3.3) for slow strain rate tensile (SSRT) test was used. This design has the advantage that the sample acts as the gas containment volume throughout the experiment, thus avoiding the need for autoclaves and sophisticated equipments. A standard hydraulic 4-column load frame (MTS 311.21 ServoHydraulic Load Frame) with a load capacity of 350kN and modified adapters as shown in Figure 3.3 was used to perform the experiments. The supply of gas during testing was provided through the top adapters connected to gas cylinders of hydrogen and nitrogen, each with a purity of 99%.

A polycarbonate shield is set up around the testing area for safety as the experiment is done till failure and hydrogen gas is released into air upon fracture. The volume of hydrogen released on failure is small for combustion to occur and it disperses fast in the absence of an ignition agent [87]. Multiple valves are also installed on either side of the adapters to prevent flow of hydrogen from the cylinder during failure.

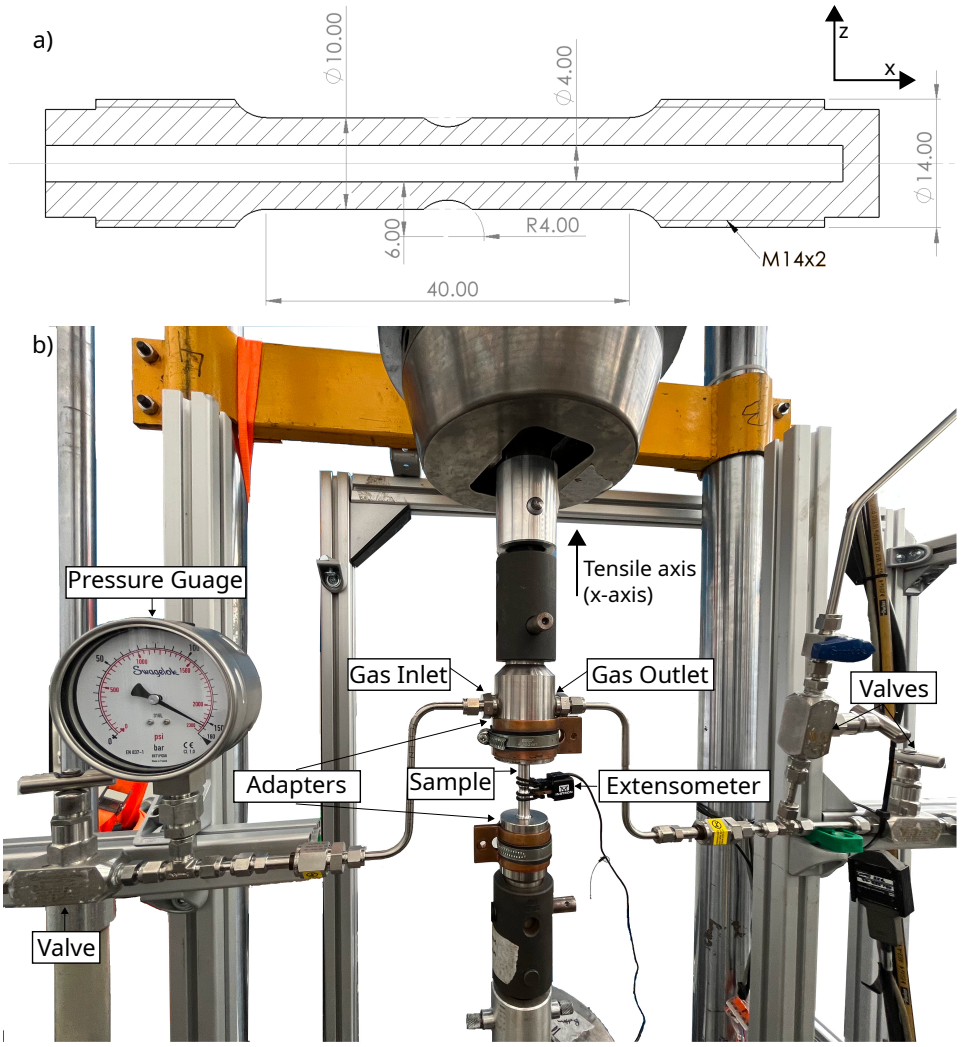

Figure 3.3: a)Sample dimensions b)Test setup for SSRT. The tensile loading direction is the x-axis.

Test Procedure

The oil and dirt which comes from the machining process affects the adsorption of hydrogen into the sample during HE testing; therefore, it is necessary to clean the samples before the test. All samples were cleaned before testing to keep it consistent. Initially, a cotton swab was used to wipe the inner surface to remove the oil and dirt; after which it was placed in an ultrasonic bath with isopropanol for at least 5 minutes. A brush with 600 grit SiC particles was then used to sand the inner surface to remove the oxide layer. It was again cleaned in the ultrasonic bath for 5 minutes.

After this, the air and nitrogen samples were placed in the experimental setup and tested in the respective environments. In the case of hydrogen environment samples, an additional step of charging is present. The internal hydrogen samples were charged in an oven at 300°C and 1 bar pressure in 99% pure hydrogen environment. A charging time of 14 hours was chosen based on diffusion simulation to homogeneously distribute the hydrogen within the sample. After charging, the experiment was done within a day: as the diffusion of hydrogen at room temperature is slow, only a negligible amount of hydrogen

is lost from desorption in this duration. If the experiment was not done within a day, the samples were stored in a freezer at -80°C till the day of the experiment. The specimen for the in-situ test, after cleaning, was directly placed in the test setup. It is initially flushed with nitrogen and vacuumed for three times to remove all traces of oxygen. It is then filled with hydrogen at 150 bar and left for 48 hours of charging.

Before the beginning of the experiment, after pre-charging a pre-load of 500 N was approached to align and remove all clearance in the machine and adapters. An Instron extensometer (model no: 2620-603) with 10 mm gauge length was then placed on the specimen over the notch. During the test when the specimen begins to yield the extensometer was removed to avoid damage during failure and then the crosshead displacement was used to determine the final strain in the material. As an Instron extensometer is used in the MTS machine a calibration experiment was separately done to correct the extensometer signal. The procedure for the same is provided in Appendix A.

The crosshead speed is set to 1.5 mm h^{-1} to let hydrogen diffuse and interact with the material during the test. The test is set to end when fracture has occurred: the criteria set for failure detection is a load drop of 20% between two acquisition points.

Test Matrix

The test matrix for the SSRT tests is shown in Table 3.4. The primary aim of the experiments is to characterise the HE behaviour of AM-produced Inconel 718 using recycled powder. Initially, the conventional samples are tested in four environments: air, N_2 150 bar, H_2 150 bar and H_2 oven charged. This is to understand the influence of pressure, and the effect of internal and external hydrogen. Then the testing conditions representing the highest hydrogen embrittlement are chosen for the AM samples. Additionally, for AM samples to represent non-hydrogen conditions N_2 at 150 bar is chosen to also account for the effect of pressure. Two repetitions are performed for each testing condition for reproducibility.

Table 3.4: Test matrix for the SSRT experiment of Inconel 718.

Sample	Environment	Charging Condition	Repetitions	Purpose
Conventional	Air	1 bar 25 °C	2	Baseline
	Nitrogen in-situ	150 bar 25 °C	2	Effect of pressure
	Hydrogen in-situ	150 bar 25 °C	2	Effect of in-situ gas
	Hydrogen ex-situ	1 bar 300 °C	2	Effect of internal hydrogen
AM	Nitrogen	150 bar 25 °C	2	Evaluate performance of
	Hydrogen in-situ	150 bar 25 °C	2	AM samples
AM+HT	Nitrogen	150 bar 25 °C	2	Evaluate performance of
	Hydrogen in-situ	150 bar 25 °C	2	heat treated AM sample

Data Analysis

The extensometer is placed on the sample as shown in Figure A.2. The cross-sectional area is not uniform throughout the notch, i.e. the deformation is non-uniform during the experiment. In addition, it also measures strain from a part of the non-notch region. For simplicity, the strain measurement is assumed to be from a uniform cross-section corresponding to the notch root diameter. The measured yield and ultimate tensile strength would be higher than the actual values, whereas it would be lower in the case of elongation. The strain is measured using the extensometer until the specimen yields, after which

it is removed and the crosshead displacement is used to determine the strain. The detailed procedure is explained in Appendix A

The elongation at failure measured is not accurate as the extensometer is not used throughout the experiment. So, the area of fracture surface is used as a measure of ductility: higher the ductility smaller the area of fracture surface. The reduction in fracture surface area(% A_{red}) is determined using Equation 3.1[71]:

$$A_{red} = \frac{A_{before} - A_{after}}{A_{before}} \times 100 \tag{3.1}$$

where A_{before} is the initial cross section of the sample before testing and A_{after} is the cross sectional area measured after failure. The % A_{red} is then used to estimate the hydrogen embrittlement index (HEI) in the hydrogen samples as per Equation 3.2[71]:

$$HEI = \frac{(A_{red})_{N_2} - (A_{red})_{H_2}}{(A_{red})_{N_2}} \tag{3.2}$$

It should be noted that a higher HEI would signify a higher degree of embrittlement.

Fractography
After the SSRT testing, to analyse the fracture surface features, the samples are cleaned in an ultrasonic bath with isopropanol for 2 minutes and investigated in the SEM. Reduction in cross-sectional area is a measure of ductility and to determine it, the fracture surface area is measured using the Keyence VHX-5000 digital microscope. The interaction of microstructure and crack propagation during failure is of interest; therefore, representative fracture samples for each testing condition are cut in the direction parallel to the tensile axis (yz-plane). It is subsequently mounted in a conductive resin and prepared for microstructure analysis.

3.3. Computational Methods

The diffusion of hydrogen in Inconel 718 at room temperature is of the order of 10^{-9} mm^2/s [54], this means that to diffuse a distance of 2mm it would approximately take 100 years ($\sim \sqrt{Dt}$, where D is diffusion coefficient in mm^2/s and t is times in seconds). Hence, a homogeneous distribution of hydrogen is not achieved for testing at room temperature. However, computational methods can be employed to have an estimate of the concentration profile of hydrogen within the sample. To identify the pre-charging conditions and the concentration profile a computational simulation is employed using FiPy (an open source finite volume PDE solver in python), GMSH(an open source finite element mesh generator) and Paraview (an open source data visualisation tool)[88, 89, 90].

The axisymmetric nature of the geometry is utilised to approximate the specimen as a 2-D model for the simulation. As the geometry is also symmetric, the 2-D model is further reduced to half; increasing the computational efficiency. GMSH is used to create the 2-D model and generate structured mesh for the simulation. It is known that mesh size is a key parameter for accurate results in a simulation: the smaller the mesh size more accurate the result is; however, this comes at a higher computational cost. A compromise between computational cost and accuracy is achieved by dividing the geometry into two regions of coarse mesh and fine mesh. At the notch root, a fine mesh is generated as it is the region

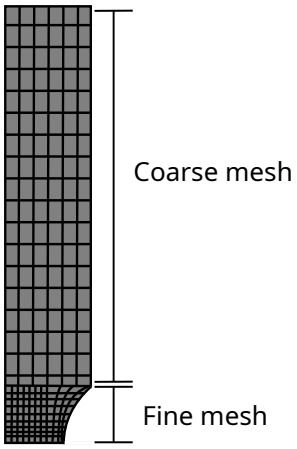

Figure 3.4: Mesh for the 2D simulation model (the mesh size is not to scale).

of focus, and away from the notch region a coarse mesh is used. Mesh convergence is achieved by refining the mesh and the final mesh parameters are saved in the geometry (.geo) file and imported into python using the FiPy package. A schematic of the geometry and structured mesh generated from GMSH is given in Figure 3.4(the geometry file for the same is available in Appendix C).

Different boundary conditions exist for both in-situ and oven-charged samples: in the case of the in-situ sample, hydrogen is only present on the inner surface at 298 K and 150 bar pressure, whereas in the case of oven-charging hydrogen is present in both the inner surface and outer surface at 598 K and 1 bar pressure. Sievert's law (Equation 2.2) is used to determine the concentration of hydrogen at the surfaces. This gives the concentration values at the surface as 7.329×10^{-10} mol/mm^3 and 8.67×10^{-9} mol/mm^3 for the in-situ and oven-charged samples respectively. It is assumed that the no hydrogen is present in the bulk before testing, hence it is set to 0. The diffusion parameters needed for the simulation are given in Table 3.5, diffusivity at the respective conditions are determined using Equation 2.5.

Table 3.5: Diffusion parameters for the simulation[54].

Sample	$\mathbf{D_0}$ mm^2/s	$\mathbf{H_D}$ J/mol	**R** J/K.mol	$\mathbf{H_s}$ J/mol	**T** K	**P** MPa (bar)	$\mathbf{K_0}$ mol/mm^3.MPa $^{1/2}$
In-situ	0.68	48.63×10^3	8.314	8075	298	15 (150)	4.92×10^{-9}
Oven-Charged	0.68	48.63×10^3	8.314	8075	573	0.1 (1)	5.23×10^{-8}

D_0 - Diffusion coefficient, H_D - Activation energy for diffusion

R - Universal Gas constant , H_s - Dissolution enthalpy

T - Temperature , P - Pressure

K_0 - Solubility constant

A stable timestep of 500 s is chosen to prevent numerical instabilities, the simulation is run for different number of iterations and the concentration of hydrogen at each node is saved into a tab separated file (.tsv). The file is then imported into ParaView and the concentration profile at the notch root is plotted.

4

Results and Discussions

4.1. Results

4.1.1. Microstructural Characterisation

The composition of the conventional and AM samples, as measured by X-Ray fluorescence spectroscopy, is given in Table 3.1. A slight variation in the composition of the major alloying elements is noted but is within the allowed limits as per ASTM B637 standard[83]. The elements Co and Cu are not detected in the AM samples, these elements are added to impart solid solution strengthening in Ni-based superalloys, and are not expected to majorly influence the precipitation of phases in this study[91].

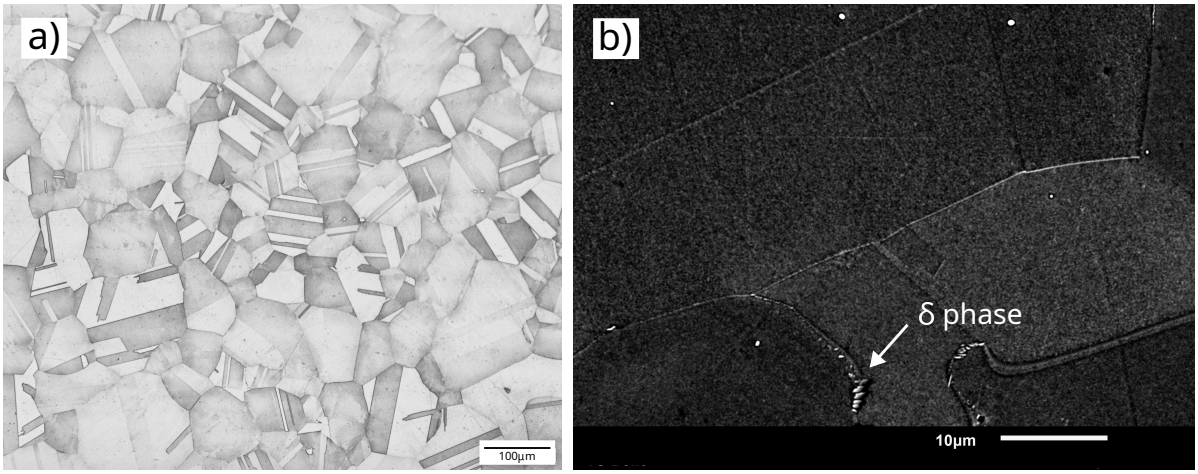

Figure 4.1: a) Optical image of conventional Inconel 718 showing equiaxed grains b) SEM image showing δ phase precipitated at the grain boundaries.

Figure 4.1 shows the microstructure of the conventional Inconel 718 sample after heat treatment with equiaxed grains and annealing twins. During the heat treatment, the solutionising temperature of 1032°C is higher than the δ solvus temperature (~1000 °C)[18], resulting in the dissolution of the δ phase. Cai et al.[92] reported that after 1 hour of holding time at 1020°C the δ phase fully dissolves in the matrix. In the current study at high magnification (Figure 4.1 b), precipitates of δ phase with a size of ~0.8 μmare seen along the grain boundaries. Nevertheless, the fraction of the δ phase observed is small, as it is found

only in certain regions and not throughout the grain boundaries. The γ' and γ" strengthening phases forms during the subsequent ageing heat treatment at 790°C for 6 hours. As these strengthening phases precipitate in the nanometre range, they are hard to discern in a scanning electron microscope. In the case of AM samples (both AM-AP and AM-HT), the microstructure appears distinct as seen in Figure 4.2 and Figure 4.3.

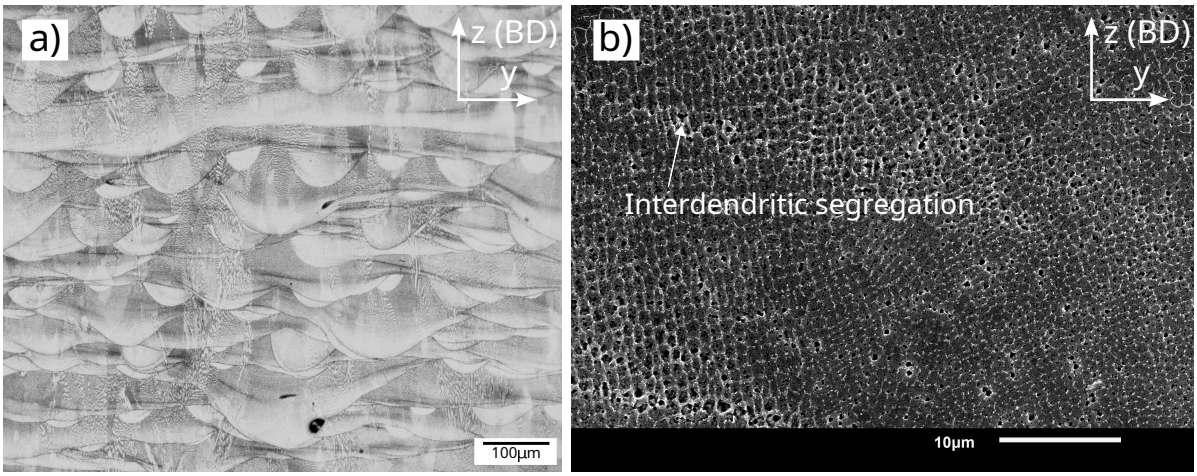

Figure 4.2: Meltpool boundaries of AM-AP samples as viewed in an OM b)Cellular substructures with segregation along the boundaries.

Along the building direction the AM-AP sample shows fish-scale-like morphology (Figure 4.2a), arising from the melting of previous layers during layer-wise deposition of material. Due to the presence of solidified layers, grain growth in L-PBF occurs epitaxially; this is seen as dendritic structures spanning multiple melt pools in the microstructure[7]. Figure 4.2 b) shows the cellular structures of the columnar dendrites. Laves phase (marked by arrows) forms in the interdendritic regions due to the micro-segregation of Nb and Ti during solidification[32]. As these segregations are detrimental to mechanical properties post heat treatments are recommended[7].

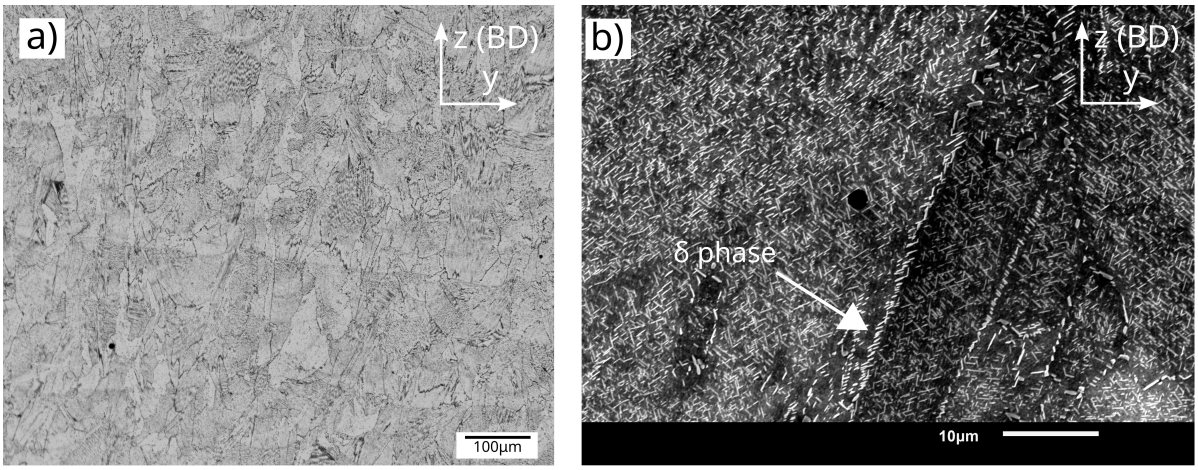

Figure 4.3: Microstructure of Heat-treated AM samples in a)Optical microscope b)SEM.

For AM-HT samples, solutionising temperature (980 °C) and time (1 h) during the SA heat treatment are insufficient for complete recrystallisation. It is evident from the microstructure shown in Figure 4.3, where partial melt pool boundaries are still visible. In

addition, at 980°C only partial dissolution of Laves phase occurs and diffusion of Nb is inadequate for homogenisation. The partial dissolution of Laves phase leads to an increase in the concentration of Nb in the neighbourhood, which results in the formation of the acicular delta phase with a size of ~1.1 μm along the grain boundaries, as seen in Figure 4.3 b). It is in agreement with the observations of Chlebus et al.[33], Li et al.[32]and Zhang et al.[25]. A two-step ageing heat treatment is also performed for the precipitation and coarsening of γ' and γ" strengthening phases. It is found that SA heat treatment doesn't eliminate the anisotropy in microstructure entirely, as complete recrystallisation does not occur. Sabelkin et al.[93] recommends a non-traditional heat treatment ,which involves annealing at 1160 °C for 4 h to allow complete recrystallisation and eliminate anisotropy.

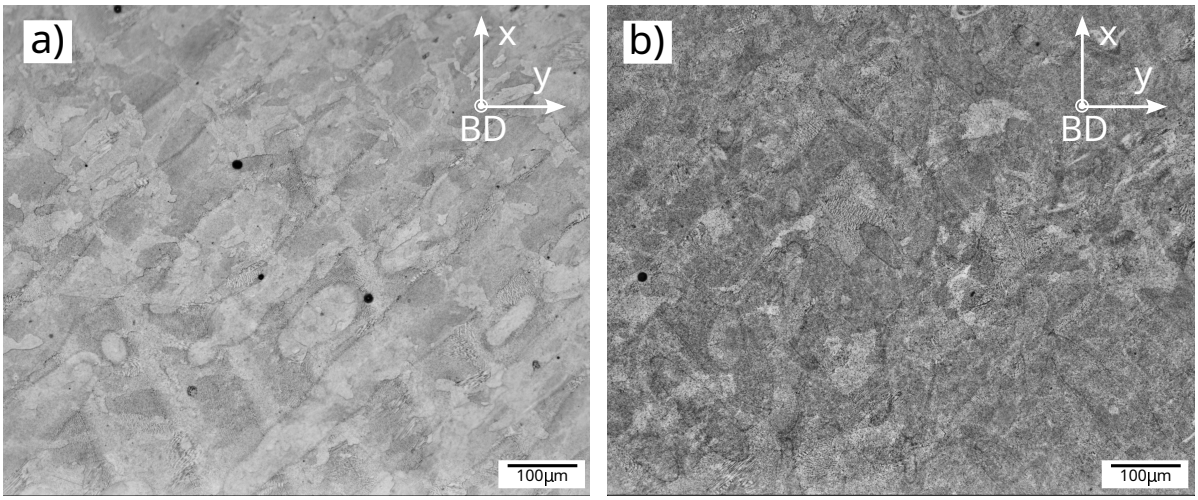

Figure 4.4: Microstructure of AM samples in the xy-plane a) AM-AP b) AM-HT.

Perpendicular to the build direction (xy-plane), the microstructure of AM-AP and AM-HT are shown in Figure 4.4. Scan tracks representative of the scanning strategy used is visible in the AM-AP samples; which become vaguely visible after heat treatment. The small grain size in this plane makes it difficult to be identified in Figure 4.4. Wang et al.[94] performed EBSD analysis and reported that the grains appeared equiaxed in this plane. The directional cooling in the L-PBF process is responsible for the anisotropy in AM microstructure.

As the size of precipitates are small, it is difficult to perform energy dispersive x-ray spectroscopy (EDS) analysis to identify the phases. So, XRD analysis is performed to confirm the presence of different phases.

XRD Characterization

Figure 4.5 shows the XRD measurement results for conventional, AM, and AM-HT. For all samples, the primary matrix phase (γ) shows the strongest peaks. Only qualitative phase analysis is performed as most of the phases give peaks which overlap with the primary matrix, thus making it hard to distinguish them. In the conventional samples, small peaks identified as γ" are seen close to the γ matrix peaks. Additionally, peaks corresponding to Ti, Nb - carbides are also visible. Even though the microstructure shows the presence of the δ phase, corresponding peaks were not identified in the XRD measurement; this is due to the poor resolution of XRD when the phase fractions are less than 5%.

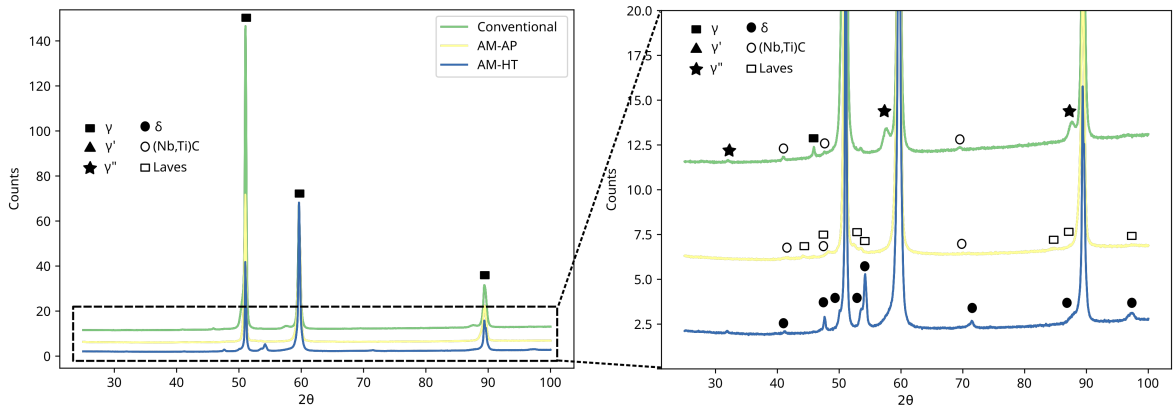

Figure 4.5: XRD measurement results.

For the AM samples in the as-processed condition in addition to the matrix phase, small peaks corresponding to Ti, Nb - carbides and Laves phase are seen. As explained in the previous section, the micro-segregation of Nb and Ti at the interdendritic regions is the reason for the precipitation of these phases.

In the heat-treated samples, the peaks for Laves phase are no longer visible; this is because during the heat treatment laves phase partially dissolves, thus reducing the fraction of phase present. In addition, the dissolution leads to an increase in Nb concentration in the neighbourhood, and the temperature is insufficient for the homogenisation of the elements in the matrix. The δ phase forms in these regions during heat treatment due to the higher concentration of Nb[25]. Small peaks corresponding to the δ phase are visible for the AM-HT sample in Figure 4.5, confirming the same.

The peaks of γ' and γ" are difficult to separate from the primary γ matrix, as they are coherent precipitates[18]. However, as the fraction of the precipitates increases, the strength of the material also increases significantly. Thus, hardness measurements can serve as a first estimate for the precipitation of the strengthening phases.

Hardness Measurements

The Vickers hardness measurements of the samples are given in Figure 4.6. The conventional sample shows a hardness of 380 ± 13 HV, which is in the expected range for the heat-treated wrought alloys[17]. In the case of AM samples, after heat treatment, the sample shows a hardness of 476±8 HV, which is 53% higher than the hardness of the AM-AP sample (310 ± 39 HV). This is expected, as the heat treatment introduces γ' and γ" strengthening phases, which are absent in the as-processed condition[33]. On the other hand, even after the precipitation of γ' and γ" phases, the conventional sample shows a hardness value lower than AM-HT samples. The difference in the hardness of AM-HT and conventional samples can be attributed to the fine microstructure induced by the L-PBF process. This is evident when comparing Figure 4.1 and Figure 4.3, and is in agreement with data reported by Tanja et al.[95]: where the grain size of L-PBF Inconel 718 is reported to be finer than the forged counterpart by a factor of 10.

Hardness measurements are not found to be influenced by the presence of porosity in the L-PBF samples[96]. However, depending on the shape and size of the pores, they can be detrimental to mechanical properties.

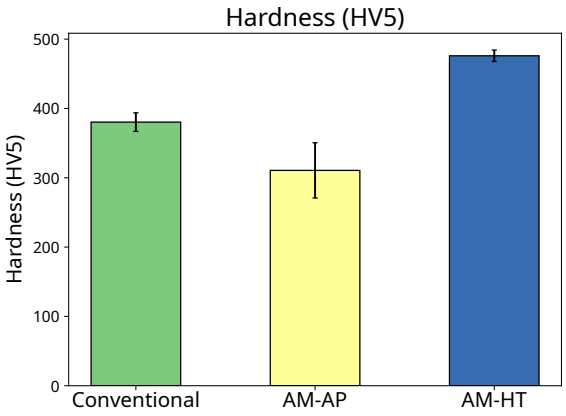

Figure 4.6: Hardness measurement values.

Porosity Measurements

Porosity is a defect commonly observed in the components produced from the L-PBF process and is absent in the wrought counterpart, as observed in Figure 4.7. The AM as-processed and heat-treated samples show comparable porosity values of 0.09±0.02 and 0.05±0.01 % respectively, making it nearly defect-free (99.9% density) material. Spherical pores signifying gas entrapment were the most commonly seen pore morphology, with the largest pore size being 45μm. The spherical pores form during the L-PBF process, when the inert gas used to prevent oxidation of powder or the gas already entrapped in the powder feedstock gets trapped in the melt pool during solidification[7]. A few lack of fusion defects (LOF) were also seen; as the name suggests these defects arise due to insufficient bonding between two layers or scan tracks. These defects are usually not observed when optimised process parameters are used[51]. Due to their shape they are detrimental to the mechanical properties as crack initiation can occur at these locations.

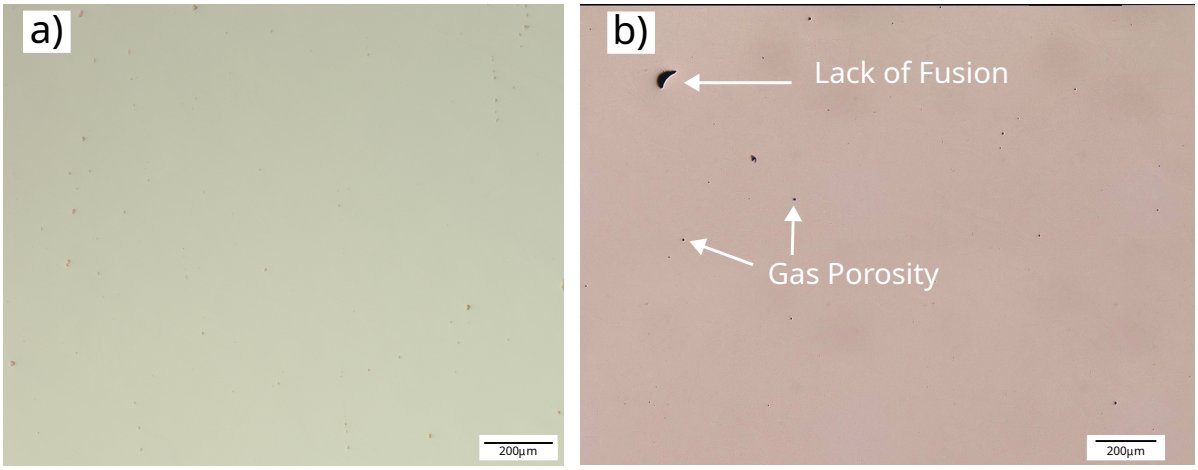

Figure 4.7: Representative images of porosity for a) Conventional and b) AM Inconel 718.

4.1.2. Diffusion Simulation

The diffusion simulation results for the in-situ gas charged and oven charged samples are given in Figure 4.8. As the diffusion coefficient of hydrogen at room temperature is only $2.3 \times 10^{-}9$ m^2s^{-1}: hydrogen only diffuses a distance of 50 μm. Whereas in the case of oven charging, hydrogen is more or less uniformly distributed in the notch root of the sample after 12 hours because of the high diffusion coefficient at 300°C. Also, the boundary conditions in both oven charging and In-situ are different. As oven charging is done at 1 bar pressure at 300°C, the concentration of hydrogen at the surface is an order of magnitude higher than the In-situ condition (150 bar, 25°C). It should be noted that the sample doesn't immediately cool down to room temperature after 12 hours of charging, as it is difficult to remove it from the oven. So, it is allowed to cool down in the oven. Slow cooling of the sample could result in a decrease of hydrogen concentration at the surface, as it is temperature-dependent, which could further lead to a decrease in hydrogen concentration within the sample. To accurately estimate the concentration of hydrogen in this case, a technique like thermal desorption spectroscopy should be employed[97]. In this study, it is reasonable to assume that the hydrogen concentration does not vary much in the bulk of the sample during the cooling stage, because hydrogen diffusion decreases exponentially with decreasing temperature.

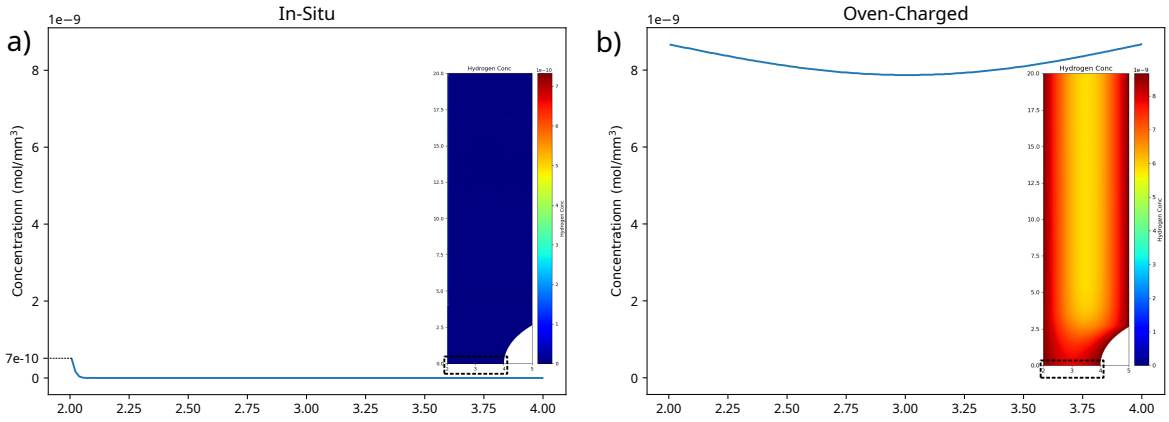

Figure 4.8: Concentration profile after gaseous hydrogen charging for a) In-situ b) Oven-Charged.

The AM samples' diffusion coefficient is found to be higher than the conventional counterparts but is of the same order of magnitude[77]. Hence, the hydrogen concentration profile of AM samples is expected to be similar to the conventional sample in In-situ condition before the start of the SSRT test.

4.1.3. In-situ Gaseous Hydrogen Mechanical Testing

The results of the SSRT test are summarised in Table 4.1 and representative plots for each testing condition is given in Figure 4.9. Due to the notch, all samples show tensile strength higher than the actual values; whereas the elongation is found to be lower.

A direct comparison of AM properties with the conventional sample is difficult due to the difference in heat treatments. However, a general trend can be obtained and compared with literature for a deeper insight. The major difference occurs with the AM heat treated samples where the double ageing with longer duration is employed. As accurate quantifi-

cation of the strengthening phases is not performed in this study, information from the literature is used to reference.

Table 4.1: SSRT test results.

Specimen	Environment	Y_s (MPa)	UTS (MPa)	Elong (%)	A_{red} (%)
Conventional	Air	1083 ± 34	1446 ± 14	11.3 ± 0.4	28.5 ± 0.5
	Nitrogen in-situ*	1069 ± 4	1474 ± 28	12.7 ± 1.4	30.6 ± 1.4
	Hydrogen ex-situ+	1116 ± 01	1493 ± 62	7.7 ± 0.7	20.5 ± 2.5
	Hydrogen in-situ**	1059 ± 34	1308 ± 01	5.8 ± 0.1	17.2 ± 2.1
AM-AP	Nitrogen in-situ*	898 ± 11	1129 ± 11	7.5 ± 0.05	24.0 ± 1.3
	Hydrogen in-situ**	897 ± 12	1153 ± 05	5.4 ± 0.1	19.5 ± 0.6
AM-HT	Nitrogen in-situ*	1462 ± 08	1776 ± 07	4.5 ± 0.3	11.7 ± 1.8
	Hydrogen in-situ**	1409 ± 10	1610 ± 3	2.8 ± 0.2	10.8 ± 0.3

* in-situ - 150 bar, 25 °C during the test.

+ ex-situ - precharged at 1 bar, 300 °C for 12 h before test.

** in addition to in-situ condition it was precharged for 48 h in hydrogen at 25 °C.

In the conventional samples (Figure 4.9 a), for both nitrogen and air conditions, the tensile curves were similar and were well within the margin of error. This shows that the presence of internal nitrogen pressure does not influence the mechanical properties in Inconel 718. Figure 4.9 b) shows the representative SSRT plots for AM samples, along with conventional samples in the same conditions. The measured strain values and reduction in cross-sectional area for the AM samples vary from the values in literature[17], this is attributed to the presence of notch in the sample. In addition, AM-AP samples shows much lower ductility compared to the conventional ones.

Among the AM samples in nitrogen condition, there was a clear difference in the tensile strength and ductility. The AM samples show a 62% increase in yield strength and a 57% increase in ultimate tensile strength after heat treatment; this was expected, as in the as-processed condition the γ' and γ" strengthening phases are absent. The 51% loss of ductility in the AM samples after heat treatment can be attributed to the strength ductility trade-off and precipitation of the δ phase. Similar trends were also observed in the literature[98, 33, 25].

Embrittlement is observed in all samples when hydrogen was introduced irrespective of the type of charging. However, the degree of hydrogen embrittlement varies. A general observation in the SSRT curves for all hydrogen In-situ samples, which was not found in the literature, was the drop in load after reaching particular stress. In a uniaxial tensile test, a load drop before failure signifies a reduction in load-bearing cross-sectional area. The load drop is not observed in the nitrogen or air samples which demonstrated higher ductility. Hence, the possible cause for the load drop in hydrogen In-situ samples is the beginning of decohesion during HE. This can be confirmed through fractography, as will be done in a later section. The loss of ductility in the presence of hydrogen is a measure of degree of HE (HE index), and can serve as a measure to compare the HE in different samples.

The hydrogen embrittlement index (HEI) of samples is provided in Figure 4.10, it should be noted that higher values signify a higher degree of embrittlement. In the conventional samples, the oven-charged samples representing internal hydrogen showed a lower degree of hydrogen embrittlement as can be seen in Figure 4.10 a). Tarzimoghadam et al.[99]

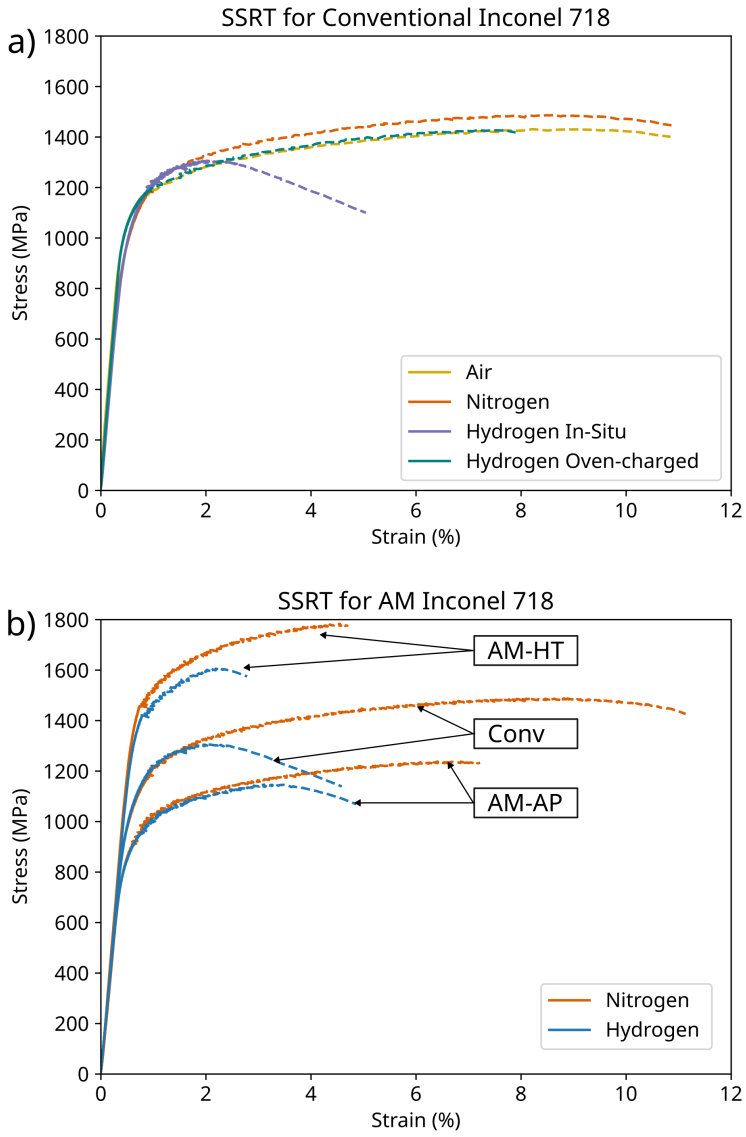

Figure 4.9: Representative SSRT curves for a) Conventional and b) AM Inconel 718.

reported that when in-situ electrochemical charging is performed the hydrogen concentration in the sample was much higher than in pre-charged condition. The simulation in subsection 4.1.2 only accounts for the pre-charging condition and not during the SSRT test. Whereas in reality, the continuous supply of hydrogen combined with the stress state in the sample could lead to a higher concentration of hydrogen for the in-situ condition.

In the case of AM samples, AM-AP samples show a lower HEI in comparison to the conventional ones, this difference can be majorly attributed to the absence of γ" precipitates. Rezende et al.[79] studied the influence of γ" precipitates on the HE behaviour and reported that it's presence aggravated hydrogen embrittlement. similar observations were seen by Hesketh et al. [81], where the lower degree of HE was attributed to the lower tensile strength of AM-AP samples. In general metals having high tensile strength show a higher degree of hydrogen embrittlement[86]. Surprisingly in this study, the AM-HT samples which demonstrate the highest yield strength, show the least degree of embrittlement

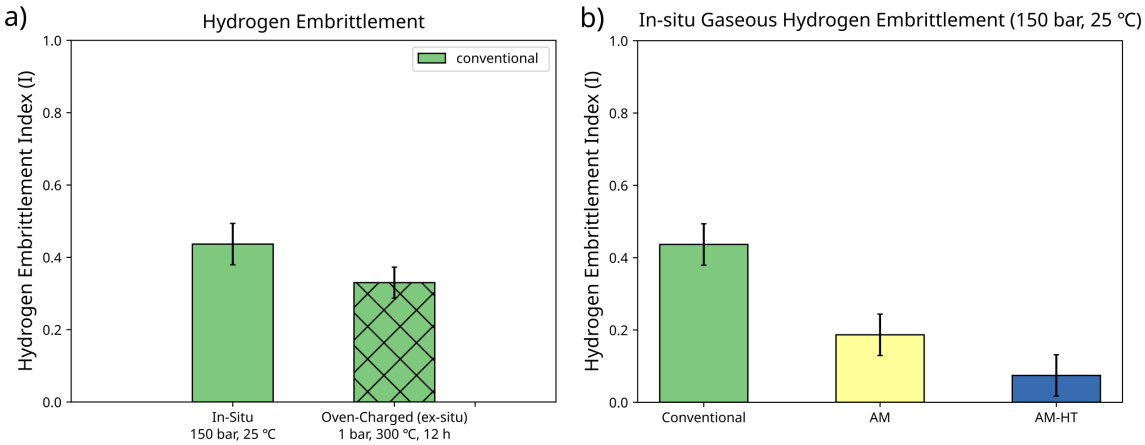

Figure 4.10: HE index for all studies herein Inconel 718 samples. The in-situ samples were also additionally charged for 48 h at 150 bar and 25 °C before the in-situ experiment.

compared to AM-AP and conventional samples, thus deviating from the earlier mentioned trend. This behaviour could arise due to the unique microstructure inherent to the L-PBF process, which could affect how hydrogen interacts with the material. To better understand this the fracture surface is looked into to help identify the HE mechanisms.

4.1.4. Fractography

The fracture surfaces of the conventional and AM samples tested in ambient conditions are given in Figure 4.11 and Figure 4.12 respectively. Considering the conventional samples, the ones tested in air and nitrogen environment (Figure 4.11 a), shows features of a typical ductile failure, i.e. failure by micro-void coalescence (Figure 4.11 b). The void size was determined to be ~4.5 μm. Only a representative fracture surface of sample tested in nitrogen is provided, additional fracture surface images for the samples tested in air is provided in Appendix B.

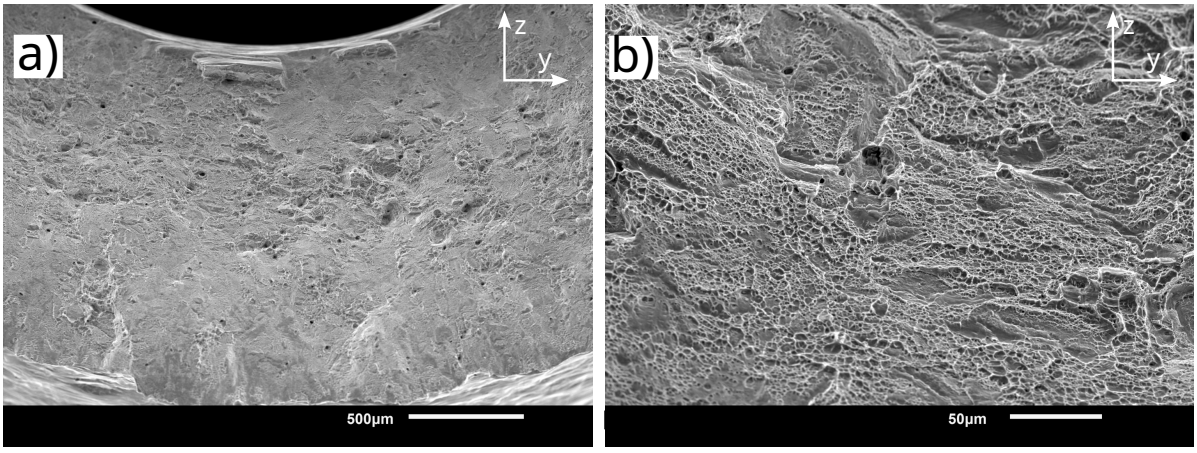

Figure 4.11: a) Zoomed-out overview b) zoomed-in view showing characteristic ductile fracture with micro voids.

The AM samples, both AM-AP and AM-HT in the nitrogen environment show a ductile mode of failure; however, the micro-voids appear to be ~65% smaller than the conven-

tional samples. The smaller dimple size (~1.5 μm) is attributed to the fine microstructure produced from the L-PBF process[22, 25]. As no significant variation is noted in the fracture surface of AM-AP and AM-HT samples, only one representative surface is shown here (Figure 4.12). If needed the fracture surface images of AM-HT are provided in Appendix B

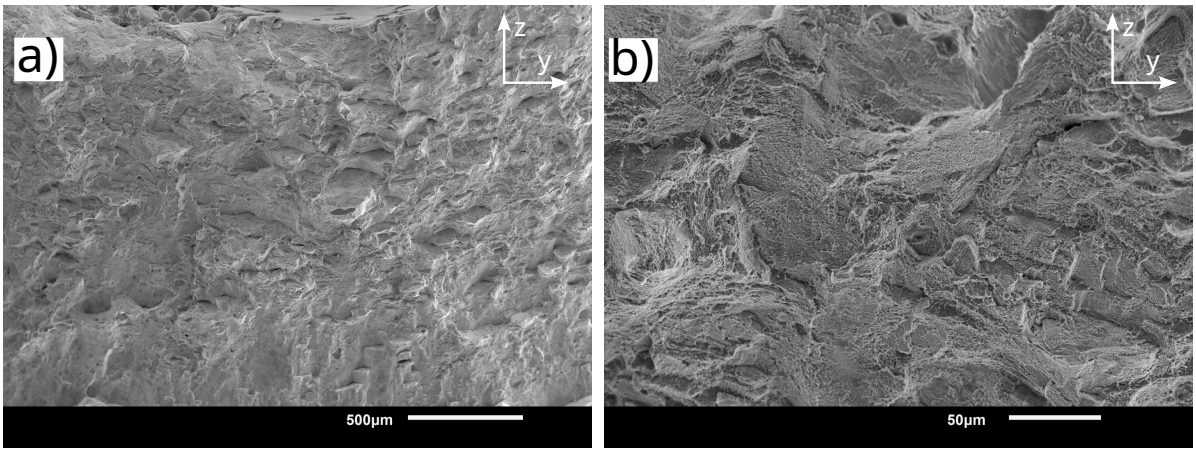

Figure 4.12: Fracture surface of AM-AP tested in Nitrogen at 150 bar. a) low magnification b) High magnification.

Additionally, for the AM samples process-induced defects are observed on the inner surface (as shown in Figure 4.13). L-PBF process is known for dimensional inaccuracy when building hollow cylinders horizontally (axis in XY plane)[100]. As in this study, the samples were built to near net shape the dimensional inaccuracy was higher than expected leading to unmachined regions during post processing; referred to as defects from here on. These defects are seen in the inner surface of all AM samples; thus, only a representative image is depicted here. Additionally, only one such defect is observed for a given fracture surface meaning just one side remained unmachined throughout the inner surface for a given sample. The lower ductility in the AM samples compared to the conventional ones could be attributed to these defects and porosity, as crack initiation could occur at a much earlier stage resulting in premature failure.

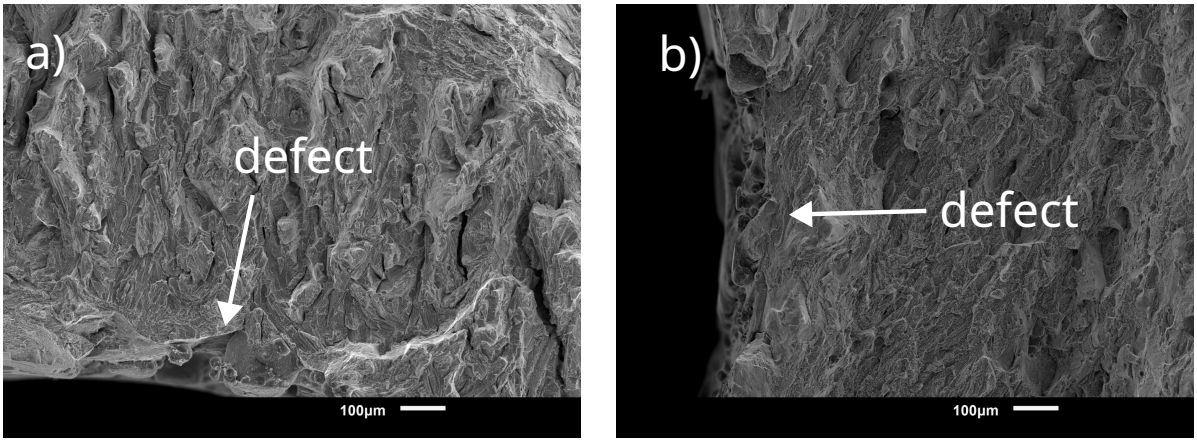

Figure 4.13: Unmachined regions in the inner surface of AM samples. a) AM-AP b) AM-HT

In the case of hydrogen charged samples (Figure 4.14 and Figure 4.15), the fracture surfaces show embrittlement, with the in-situ samples showing severe embrittlement. Addi-

tionally, for all hydrogen in-situ samples, fracture initiates from the inner surface of the sample instead of the notch. Three distinct regions can be observed on the surface of In-situ samples (Figure 4.15): 1) brittle intergranular region, 2) quasi-cleavage region and 3) ductile region. Severe cracking (marked by arrows) on the fracture surface is also seen. The hydrogen oven-charged samples show only quasi-cleavage-like features (facets surrounded by dimpled regions) similar to region 2 of In-situ samples. This difference in the oven-charged and in-situ samples could be due to the difference in underlying HE mechanisms, which is discussed in a later section.

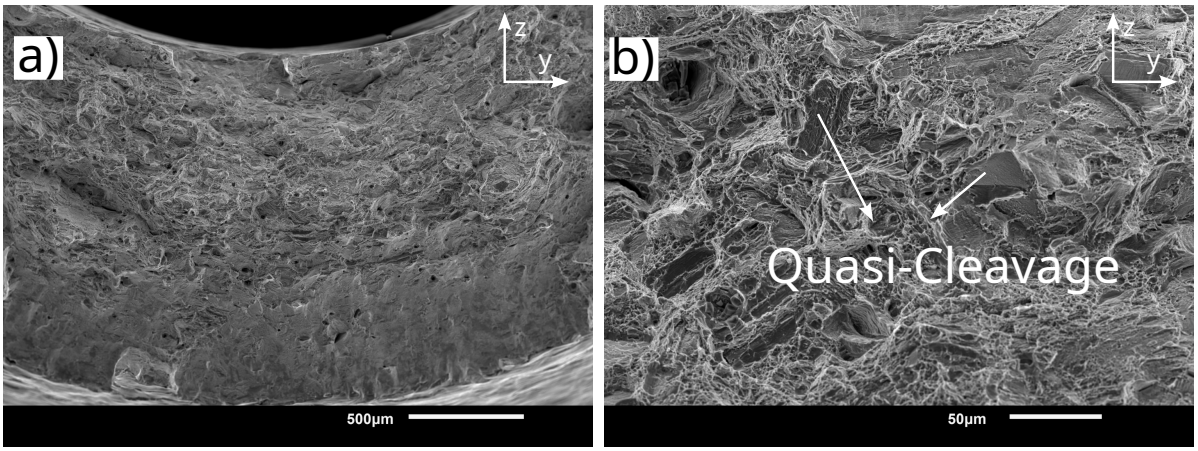

Figure 4.14: Quasi-cleavage features on the fracture surface of conventional samples tested after hydrogen oven charging. a) low magnification b) high magnification.

The brittle region in the in-situ sample consisted of features representative of the grain structure. Tear ridges signifying plasticity is also visible in this region. Several researchers have reported fracture surfaces similar to this after electrochemical charging[52, 101]. Zhang et al.[101] reported that though the features show an intergranular mode of failure, the crack initiates and propagates through dislocation slip bands and hence is actually transgranular in nature. A key issue with this mechanism is that, in this study as seen in the simulation results (subsection 4.1.2), hydrogen diffusion distance during charging is only 50 μm but the embrittled region extends $\approx$ 1.5 mm. It is possible that, as fracture initiates from the inner surface there is a continuous supply of hydrogen at the crack tip from gaseous hydrogen; thus leading to a larger embrittled region. In this case, the proposition by Zhang et al.[101] that failure initiates at the slip bands requires further analysis, as whether hydrogen has sufficient time for diffusing within the grain is questionable.

Similar to the conventional samples, the hydrogen in-situ AM samples show a severely embrittled region. A distinct difference observed here is that; the HE region is directional as shown in Figure 4.18, unlike the conventional samples, which show homogeneous embrittlement throughout the fracture plane. This difference could arise due to the microstructural anisotropy in the sample. Features representative of elongated grains is visible in the HE region for both AM-AP and AM-HT samples. Further, these HE regions appear to be oriented along the build direction as can be deduced from these elongated features. The lower degree of HE in AM samples compared to the conventional samples could be a consequence of this anisotropy; as only a small region is embrittled and the remainder of the sample retains its ductility. This is unanticipated as additional defects seen on the inner surface is expected to aggravate HE.

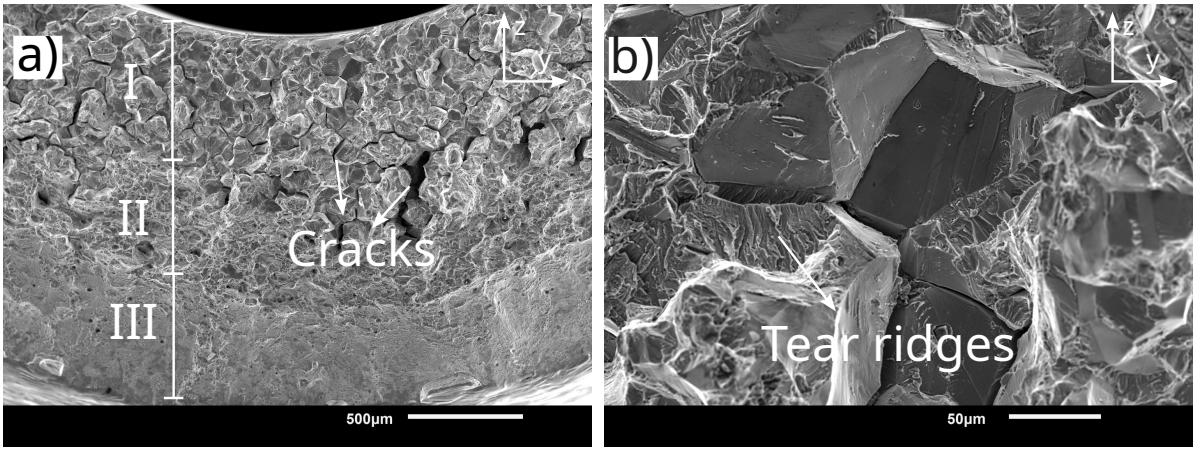

Figure 4.15: Three distinct regions on the fracture surface of conventional samples tested in hydrogen in-situ condition. a) low magnification b) high magnification at region of intergranular failure.

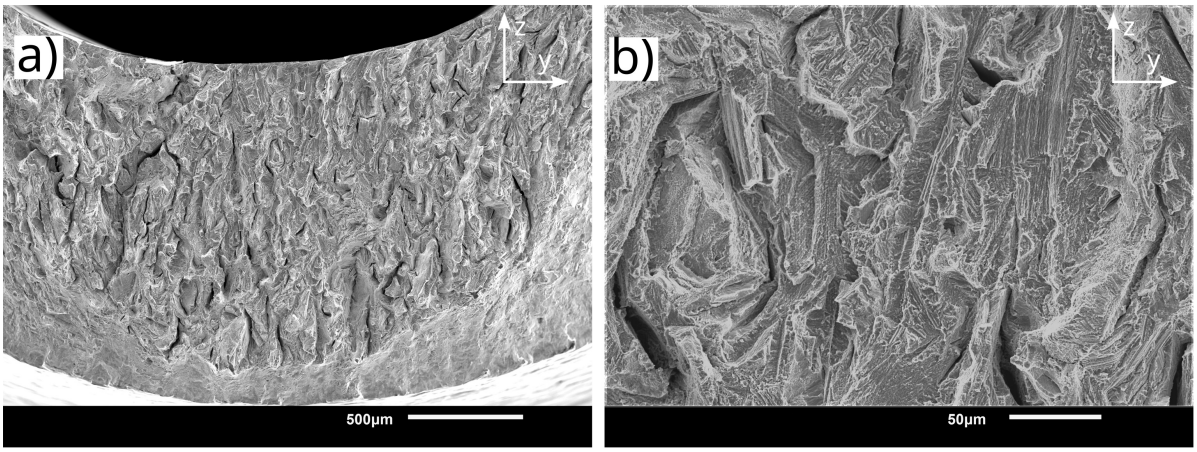

Figure 4.16: Hydrogen embrittled fraction region in AM-AP sample a) low magnification b) high magnification.

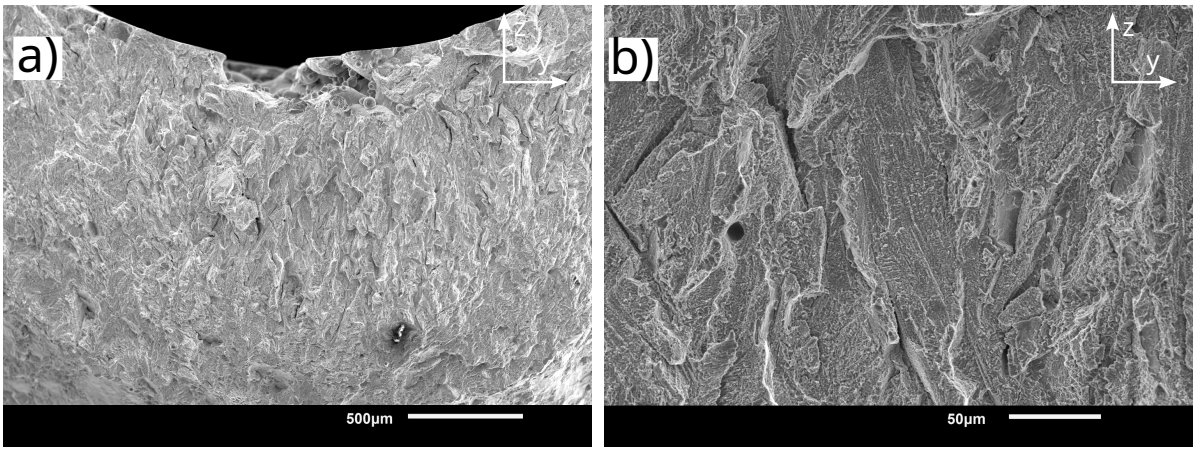

Figure 4.17: Hydrogen embrittled fraction region in AM-HT sample a) low magnification b) high magnification

Due to the presence of defects as shown in Figure 4.13, it would be expected that the HE region would be aligned with the defects, however, that is not observed. The elongated

features appear to be consistent with the building direction irrespective of the location of the defect in the inner surface. This signifies that anisotropy plays a more dominant role.

Among the AM-AP and AM-HT samples (Figure 4.16 and Figure 4.17 respectively), the former shows prominent brittle features and cracks on the fracture surface. This is in line with the observation of higher HEI for the AM-AP compared to AM-HT in the previous section. Porosities are observed on the fracture surface of AM samples, they however don't appear to influence HE, this could be because the porosity is negligible. Hesketh.et al [81] also reported similar findings. In theory, porosity would be detrimental as it would reduce the cross sectional area and can act as stress concentrators aggravating hydrogen embrittlement.

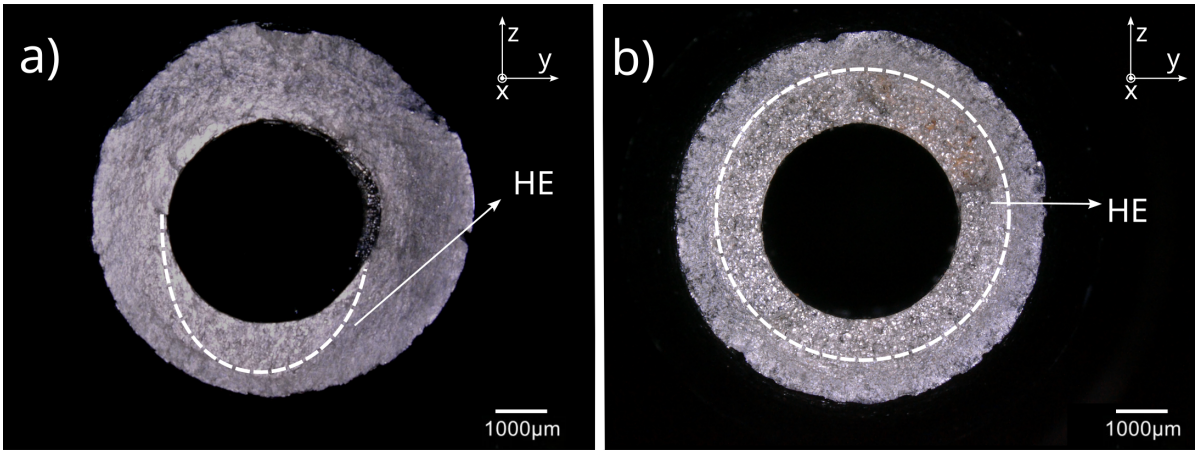

Figure 4.18: a) Anisotropy in HE region of the AM sample b) Homogeneous HE region in conventional sample. X-axis is the tensile load direction and z-axis is the build direction.

4.2. Discussion

4.2.1. Effect of recycled powder in AM of Inconel 718

The preliminary microstructure analysis of AM-AP and AM-HT samples show comparable results to the ones found in literature[25, 34, 102]. Due to the fine microstructure from the L-PBF process and the resolution limit of SEM; it is difficult to observe the morphologies of the precipitated phases, which is influenced by material composition. Even though the compositional range of the elements are within the limits defined by ASTMF 3055[85]. The variation could alter the precipitation behaviour of different phases[103]. This in turn could affect the mechanical properties as it is dependent on the morphologies and fraction of these phases[18]. Here, hardness measurements are used as a first estimate for the precipitation of γ' and γ" strengthening phases. The increase in hardness confirms the presence of the strengthening phases, though the fraction of these phases are difficult to estimate.

The volumetric energy density (VED) is a key parameter that influences the porosity in L-PBF process. Porosity is generally found to decrease when VED is increased, but increasing it too high again increases porosity[96]. VED in this study is determined from the process parameters given in Table 3.2 and Equation 2.1, it was found to be 67 J/mm^3. For this VED, Caiazzo et al.[96] reported a porosity fraction of 0.11 % which is comparable to the values in this study. In L-PBF process it is impossible to prevent gas porosities,

irrespective of VED used, however the fraction of these voids decrease when high VED is used. On the other hand, lack of fusion defects can be eliminated by optimising the process parameters[51]. In this study lack of fusion defects were observed in the AM samples even though sufficiently high VED is used. The powder particles distribution, powder packing density, composition of powder, and VED are some of the key parameters affecting the porosity development in AM[7]. As the process parameters used in this study are optimised for the commercially available powder, a study aimed to optimise the process parameters as per the powder properties is recommended to eliminate lack of fusion defects. Unlike gas porosities, these defects are detrimental to the mechanical properties and hence should be eliminated entirely.

With respect to the mechanical properties, the sample shows a higher yield strength and UTS but a lower elongation when compared with the literature[30, 25, 17]. The variation could arise due to the presence of the notch. To determine strain, a uniform cross-section is assumed, which is not the case in reality. The cross-sectional area in the notch increases from the notch root to the outer region, this means that the extensometer measures a non-uniform elongation. But to determine strain a uniform elongation is assumed for simplicity. So, the determined strain would be lower than the actual strain in the material. This results in a higher slope in the stress strain curve, and leads to reporting a higher yield strength and lower elongation to failure. The higher UTS is commonly observed in notched tensile specimens of Inconel 718 when sufficient amount of δ phase is present [92].

Another aspect that could affect the mechanical properties is the effect of powder. Bhowmik et al.[104] studied the effect of reusing powder feedstock on mechanical properties of Inconel 718. It was observed that the reused powder showed a slightly higher yield and ultimate tensile strength when compared with components from virgin powder. It was attributed to the difference in dislocation density and solute distribution in the two sets of samples. In this study, though a virgin batch of powder is used, a similar difference could be present as the powder produced from recycled raw materials. An in depth analysis comparing the recycled powder with commercially available powder is required to identify variations arising from the powder feedstock.

However, this does not explain the trend of lower elongation of AM-AP samples when compared with the conventional counterpart with similar geometry. It is generally reported that in the as-processed state the AM samples have higher elongation than the age hardened conventional alloy. This is because of the absence of strengthening phases[17]. The defects reported on the inner surface of AM samples in subsection 4.1.4, are the possible reason for this observation.

4.2.2. Effect of testing conditions in HE of Conventional Inconel 718

From the fractographs in subsection 4.1.4, it is evident that the dominant mode of HE mechanism in the oven-charged and in-situ conditions are different. The quasi-cleavage failure seen in oven-charged samples denotes that plasticity plays a significant role during failure, so the dominant mechanism is likely to be hydrogen-enhanced localised plasticity (HELP). Further, the mode of failure from quasi-cleavage to intergranular is reported to be dependent on the concentration of hydrogen and yield strength of the material[86, 105, 106]. This is because the equilibrium concentration of hydrogen in the lattice scales exponentially with increasing stress[107].

Both the in-situ and oven-charged samples undergo the same post-processing heat treatment, meaning they have similar yield strength. So the cause of variation can be attributed to the concentration of hydrogen in both set of samples. This would appear counter-intuitive as in the simulation(subsection 4.1.2) it was reported that the concentration of hydrogen in the oven-charged condition is higher than in-situ charging. To understand the cause of this variation, concentration of hydrogen at the crack tip needs to be considered as it plays the dominant role.

For the oven-charged sample, increase in the concentration of hydrogen at the crack tip occurs by diffusion. As the diffusion of hydrogen at room temperature is very slow, it is likely that the concentration at the crack tip doesn't vary during the SSRT test. Dexler et al. [108] on studying the stress induced diffusion of hydrogen in nickel, reported that stress driven diffusion only plays a minor role in hydrogen transport. Hence, it is safe to assume that there is no increase in concentration at the crack tip during the experiment. A qualitative value for the hydrogen concentration can be determined from the simulation, and was found to be ≈ 7.1 ppm. Hicks et al.[105] reported that for hydrogen concentrations less than 16 wt ppm, the dimpled regions in between the facets increased. The observations in Figure 4.14 conforms to this trend, though the difference in heat treatment and alloy composition in Hicks study makes it difficult for a direct comparison. Accordingly, this should also be seen in in-situ samples, which shows an order of magnitude lower hydrogen concentration.

For the in-situ samples in addition to charging, there is also a continuous supply of hydrogen at the surface of cracks as shown in Figure 4.19. The crack initiation is observed to occur from the inside possibly due to machining marks acting as stress concentrators. After the crack initiates, the hydrogen at the crack surface can be adsorbed, increasing the sub-surface hydrogen concentration. Tarzimoghadam et al.[99] performed a similar in-situ electrochemical SSRT test and reported that hydrogen concentration increased by 200% (40 wt ppm from 13 wt ppm) during the test. The increase was attributed to the continuous supply of hydrogen at the crack surfaces. In this study, a similar increase in concentration is expected. It is difficult to quantify it, as no hydrogen concentration measurements were performed. A more detailed study of hydrogen interaction at the crack surface is needed.

To identify the dominant mechanism in in-situ condition, the intergranular fracture surface is analysed. On a macro scale, the brittle features point towards HEDE mechanism. But on taking a closer look at the facets, dislocation slip lines signifying plastic deformation are visible (Figure 4.20). This indicates a possibility for HELP or adsorption induced dislocation emission (AIDE) mechanism. AIDE is considered here as the hydrogen is present on the surfaces of the crack, and it can be adsorbed leading to dislocation emission from the crack tip.

However, before concluding on the dominant mechanism, the load drop observed in the SSRT curves (Figure 4.9) needs to be considered. It was found that the drop in load occurred only after a particular stress level is reached, as explained earlier this means a reduction in load bearing area, here it signifies the beginning of decohesion. The strain at this point was determined to be 2%. As Inconel 718 has a low stacking fault energy, it is found to show planar deformation[109]. The slip lines visible on the facets could be a consequence of this 2% strain. Further, it could also be possible that the decohesion occurred where the slip lines intersected with the grain boundaries. A cross-section of the fracture surface is analysed to understand it better.

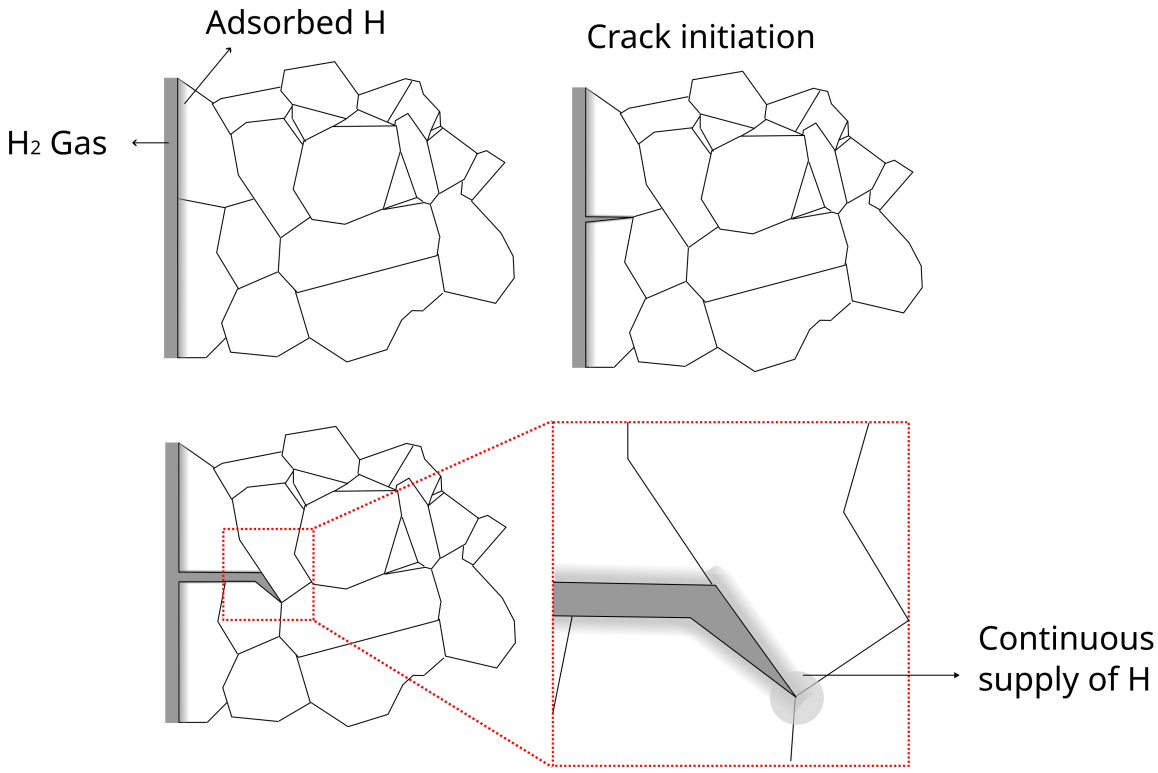

Figure 4.19: Schematic of intergranular failure in conventional Inconel 718 seen in this study. A higher concentration of hydrogen at crack tip due to adsorption from crack surface.

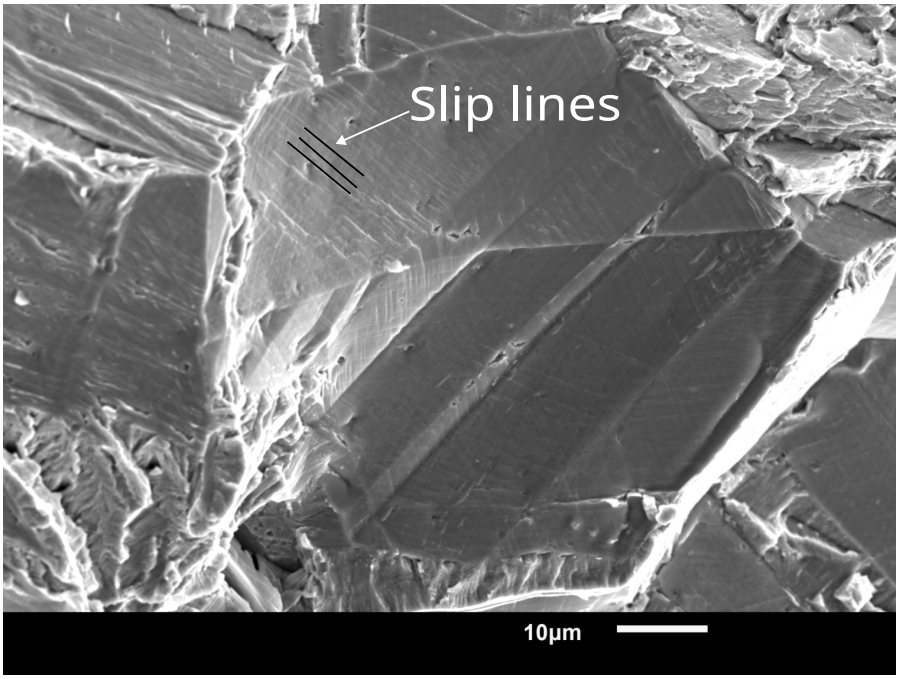

Figure 4.20: Slip lines along the brittle facets of in-situ hydrogen embrittled samples.

Figure 4.21 shows the cross-section of fracture at the brittle region, both intergranular and transgranular mode of failure is observed. A large number of dislocation slip lines are

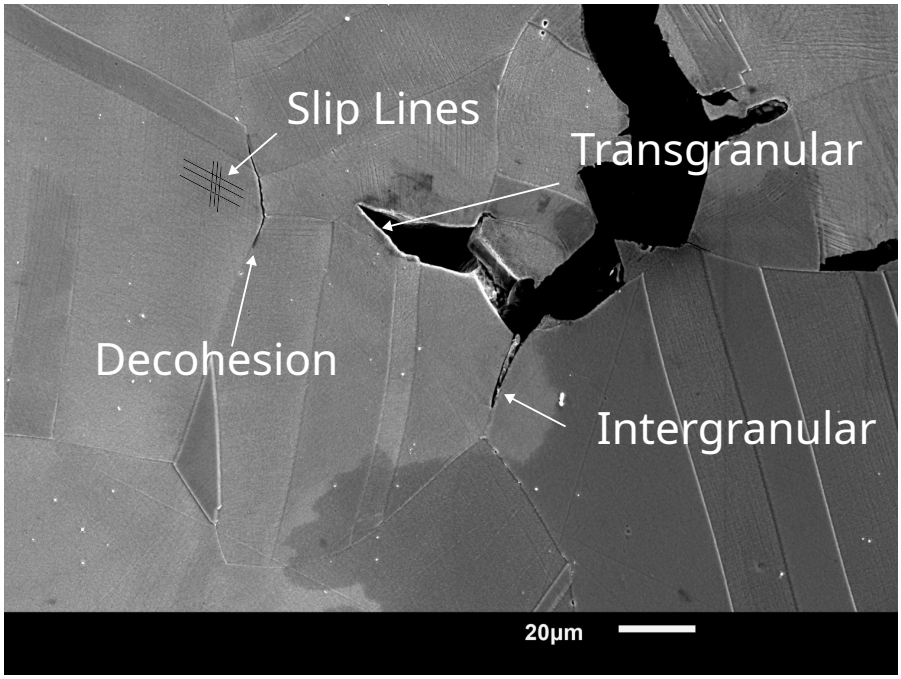

Figure 4.21: Cross-sectional image of fracture surface showing different modes of failure in conventional Inconel 718.

also visible, the transgranular failure could have occurred through these slip lines. The tear ridges seen in Figure 4.15 confirm this. A closer look with a higher resolution electron microscope could help better understand why there was a transition from intergranular to transgranular mode of failure. Decohesion along grain boundary ahead of the crack is also seen. This makes it quite difficult to make a conclusion on whether HEDE or HELP or AIDE is the dominant mode of failure as features representative of all modes of failure are visible. For now, it is likely that the mode of failure is an interplay between HEDE, HELP and AIDE mechanisms.

4.2.3. HE in AM Inconel 718

From the macroscopic fracture surfaces, it can be concluded that the HE mechanism in both AM and conventional samples are the same. Similar features that are representative of their respective microstructures are seen in both sets of samples. However, the AM samples only show embrittlement in a narrow region, unlike the conventional samples which show uniform embrittlement(Figure 4.18). This difference is due to the anisotropy in the microstructure of AM samples. As the fracture features of both AM-AP and AM-HT are similar, they are not distinguished in this section and would be in general referred to as AM samples, unless otherwise specified.

In the conventional sample, in all planes (xy, xz and yz-planes) a uniform equiaxed microstructure is observed. Microstructure along the fracture plane (yz-plane) is shown in Figure 4.22a). This means that after crack initiation, its propagation occurs the same way in all the directions of the fracture plane (yz-plane). Even if multiple cracks initiate at the inner surface as seen in the case of conventional samples, the energy required for crack propagation remains the same.

As seen in subsection 4.1.1, it is clear that the AM samples show different microstruc-

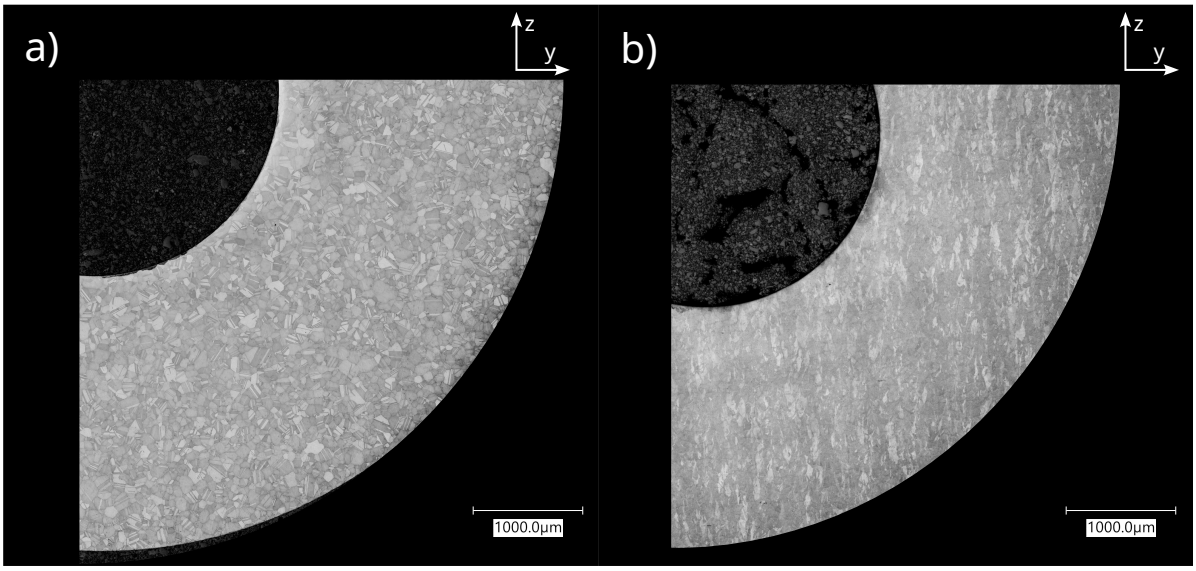

Figure 4.22: Microstructure in the fracture plane a) Conventional with equiaxed grains b) AM-HT with elongated grains. As AM-HT clearly shows elongated grains without meltpools, it is used as representative image for AM samples.

tures along different planes. The microstructure along the fracture plane (yz-plane) is shown in Figure 4.22b): elongated grains oriented along the build direction are visible. A similar microstructure is also seen in the xz-plane; however, in the xy-plane the microstructure is different. As explained in subsection 4.1.1, it is because xy-plane is the laser scanning plane. A schematic representation of this difference in the fracture plane is given in Figure 4.23.

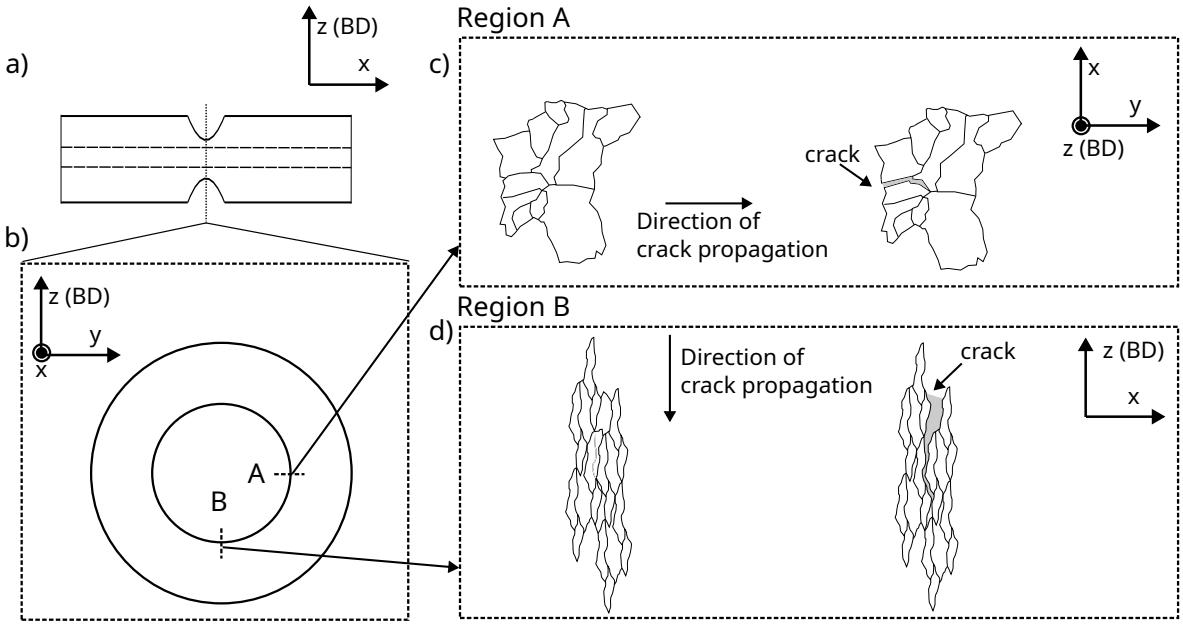

Figure 4.23: a) Schematic of sample showing area of interest (notch) b) cross-sectional view of the notch c) Crack propagation in xy-plane d) Crack propagation in xz-plane. z-axis is the build direction (BD) and x-axis is the tensile axis. The microstructure schematic is not to scale.

Crack propagation occurs in material when there is sufficient energy for creating two

new surfaces[110]; as it is a brittle mode of failure energy for plastic deformation is not considered here. In an uniaxial tensile test this energy is provided by the tensile load. If E_s is the energy required to create two new surfaces and assuming that the elongated grains are of the similar grain boundary area. The energy required for the crack to travel across a grain boundary surface would be the same in both region A and B (Figure 4.23). This is because the area of the two new surfaces created by the crack would be the same. However, the distance the crack travels by expending this energy is much larger in the z-direction (build direction) than in the y-direction; because the longer axis of elongated grains is oriented in the crack propagation direction as shown in Figure 4.23c). This is confirmed from the fracture surfaces, where along the y-direction the embrittled region is found to be $\approx$ 175 μm wide while along the z-direction the embrittled region is an order of magnitude higher ($\approx$ 1.5 mm). A more in-depth analysis is required to understand why there is an order of magnitude difference in the embrittled region; and why sometimes embrittlement is observed only on one side of the build direction.

Anisotropy in the vertically (tensile axis along the z-axis) and horizontally built samples (tensile axis along the x or y-axis) are commonly reported in the literature[7]. Hesketh et al.[81] studied the effect of orientation on hydrogen embrittlement of L-PBF Inconel 718 by in-situ electrochemical charging, and reported that the horizontal cylindrical samples exhibited higher degree of embrittlement compared to vertically built ones. The differences in the experimental conditions in the two studies makes it difficult to perform a quantitative analysis. Nevertheless, the trend in anisotropy is established. A similar study was done by Li et al.[76], where the HE behaviour of AM-produced Inconel 718 on dog bone specimens with two different horizontal orientations was looked into, keeping the long axis parallel to the tensile axis. It was reported that the sample with a microstructure similar to the Figure 4.23c)showed a higher degree of HE. This confirms the anisotropy in flat specimens built in two different horizontal directions. In a ductile mode of failure it is difficult to observe features on the fracture surface which could be a result of this anisotropy within a horizontally built sample. This would require careful analysis and it now raises the question whether cylindrical samples built horizontally are representative of properties.

4.2.4. Effect of heat treatment in HE of AM Inconel 718

Experimental observations show that the AM-AP samples have a higher degree of HE than AM-HT. This is quite unexpected as the yield strength of AM-AP samples is 65% lower than the AM-HT samples. The fracture surface features also appear similar at low magnification. At high magnification (Figure 4.24), continuous dendritic structures are visible in the AM-AP samples inside the grain-like features. Whereas, in the AM-HT samples the dendritic structures appear discontinuous. Li et al.[76] reported that in the as-processed state the hydrogen assisted cracking originated between γ matrix and Laves phase. Hence, failure may occur more easily along the dendritic structures in the as-processed state thus leading to a higher degree of embrittlement. This is also supported by the observation of Lin et al. [111], where it was reported that the cellular structures in L-PBF produced 316l stainless steel enhanced the diffusion of hydrogen and induced defects. This could be the reason for the features to be less prominent in heat treated condition as, partial dissolution of Laves phase occurs[112], as seen in the microstructure section (subsection 4.1.1). This requires further analysis as quantitative measurements of the phases are not done in this study.

Li et al.[76] and Lee et al.[75] reported that cellular dendritic structures in the AM as-

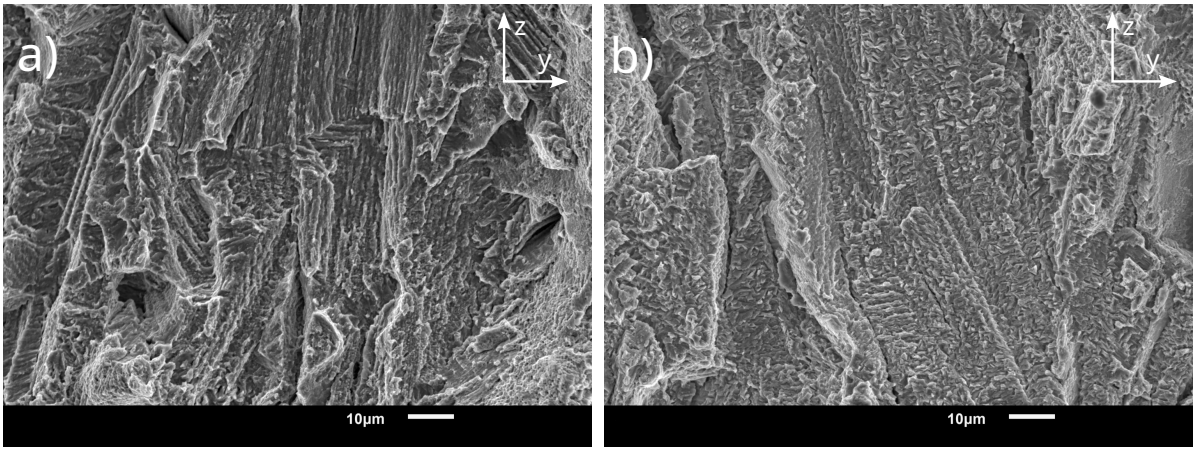

Figure 4.24: High magnification image of grain like features on the fracture surface of AM samples. a) AM-AP b) AM-HT

processed state did not influence HE. The contrasting results could be a consequence of testing conditions, sample geometry and orientations. As seen here, the anisotropy led to directional crack growth in hollow cylindrical samples. These features would not be clearly evident in flat dog-bone specimens. Additionally in these studies, SSRT tests were performed after electrochemical pre-charging which means the concentration of hydrogen remained similar in both as-processed and heat-treated conditions. As the yield strength of the as-processed samples are low, for the same hydrogen concentration as heat treated samples the degree of embrittlement would be low. However, in this study, there is a continuous supply of hydrogen at the crack surfaces leading to a higher degree of embrittlement.

Another aspect that needs to be considered is the experiment duration. As the strain rate is kept constant, the duration of experiment for each set of samples is different. This is more pronounced for samples with different yield strengths, as they begin to strain plastically at different times. To understand this better, consider an elongation of 1mm, the time taken for this elongation is same for all samples, as it is displacement controlled. However, as each sample set have different elongations, the duration of experiment is different for each sample sets. This would lead to a difference in the hydrogen uptake and diffusion during the experiment. The elongation of the AM-AP samples at failure was ≈5.4%, where as for AM-HT it was only 2.8%. This means after yielding, HE in AM-AP sample occurs in a longer duration than the AM-HT samples. This could be the major reason why higher degree of embrittlement is observed. Tarzimoghadam [99] had similar observation, where it was reported that the annealed specimens shows a ~ 70% drop in elongation even though the intermetallic precipitates were absent and the yield strength was only 400 MPa. Hence, it was concluded that a quantitative comparison between samples with different heat treatments is difficult.

4.2.5. HE in conventional and AM heat treated Inconel 718

The HEI values show that the HE resistance of AM-HT samples are much higher than the conventional samples. As the load drop marks the beginning of decohesion, the elongation at this point and total elongation at failure can also be used as a measure for better performance. Elongation is considered here, because it is difficult to measure the cross-sectional area during the experiment. Figure 4.25 shows the elongation at load drop and

total elongation at failure. A key observation is that both AM-HT and conventional sample shows similar elongation (~2%) at the start of load drop. However, the elongation at failure is 5.8% and 2.8% for conventional and AM-HT respectively. Contrary to the HEI, this shows that the conventional samples have a better HE resistance compared to AM-HT. The higher elongation to failure for conventional sample could be a consequence of uniform crack propagation along all directions in the fracture plane. Whereas, in the AM-HT sample as the crack propagation is directional the failure could occur at a faster rate.

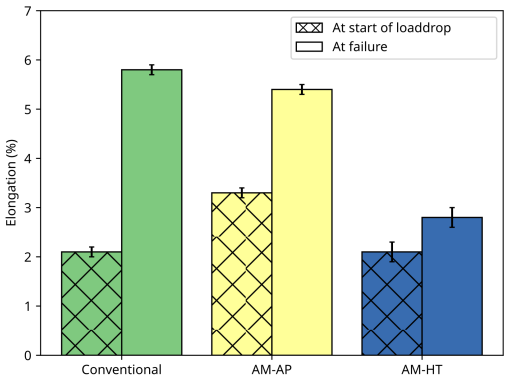

Figure 4.25: Elongation of samples at beginning of HE and total elongation at failure.

As the conventional samples are tested in the as-received condition, the difference in heat treatment with AM sample gives rise to microstructural differences. It has been reported that the fraction of γ" (the major strengthening phase) and δ phase strongly influence the HE behaviour of Inconel 718[113, 53, 80, 79]. From the microstructural analysis it was evident that AM-HT samples had higher γ" and δ phase compared to conventional sample. These phases are found to aggravate HE, but the observation of lower HEI for AM-HT contradicts this. This observation could be a result of variation in morphologies of these phases in conventional and AM-HT samples. A more detailed phase analysis (morphology and fraction of phases) can provide a deeper insight into the HE resistance of AM-HT samples with respect to the conventional counterpart.

5

Conclusion and Future Recommendations

5.1. Conclusions

Based on the research objectives defined in Chapter 2, the following conclusions were made:

- **To determine the gaseous HE of L-PBF Inconel 718 fabricated from recycled powder.**
  The L-PBF Inconel 718 produced from recycled powder shows severe embrittlement in the presence of in-situ gaseous (150 Bar) hydrogen. However, in the as-processed state the degree of embrittlement (HEI) is 50% lower compared to the conventional Inconel 718.

  Furthermore, it should be noted that L-PBF Inconel 718 fabricated in this study from recycled powder demonstrated an ultimate tensile strength in ambient conditions higher than those found in literature, 1129 ± 11 MPa and 1776 ± 7 MPa for as-processed and heat treated state, respectively. It shows that components additively manufactured from recycled Inconel 718 powder could have properties comparable or even superior to commercial powder.

- **To investigate the effect of process induced microstructural anisotropy on HE of L-PBF Inconel 718.**

  L-PBF Inconel 718 was found to have coarse grained microstructure with columnar grains elongated along the building direction (BD). Microstructural anisotropy with respect to BD was observed in both as-processed and after post-processing heat treatment states. Such anisotropy has led to a narrow hydrogen embrittlement zone along the build direction. It should be noted that even in the presence of defects, HE occurred along the build direction irrespective of where the defect was present.

- **To determine the effect of post processing heat treatment on in-situ hydrogen response of conventional and L-PBF Inconel 718.**
  Despite the higher yield strength, AM-HT Inconel 718 showed the least degree of hydrogen embrittlement (64% lower than conventional Inconel 718). The better resistance compared to the conventional Inconel 718 could be attributed to the AM-induced microstructural anisotropy. As hydrogen embrittlement occurs only in a

narrow region along the build direction, the remainder of the material retains its ductility. Unlike the conventional sample where a uniform and wide HE region is observed.

- **To study the dominant HE mechanisms in L-PBF Inconel 718.**
  Fracture surface of AM Inconel 718 was found similar to that of the conventional samples. It can thus be expected that the same HE mechanisms is occurring in both conventional and AM samples. For the conventional samples brittle cleavage facets and presence of dislocation slip lines signifying plasticity were found on the fracture surface. It was concluded that the HE mechanism includes an interplay between HEDE, HELP and AIDE.

Additionally, some general conclusions can also be made:

- The AM produced samples were near defect free, with 99.9% density. Some lack of fusion defects were observed, which can be eliminated by further optimising the L-PBF process parameters.
- The presence of defects on the inner surface has led to a lower ductility of AM samples in ambient conditions.
- The HE samples demonstrated a drop in load after a particular strain (~2 % for conventional and AM-HT) signifying the start of decohesion.

5.2. Future Recommendations

The future recommendations for further analysis

- As different heat treatment is used in the current study, a future study with similar heat treatment for the conventional and AM samples is recommended to provide a better comparison in HE performance.
- An in depth TEM phase analysis for the AM components to identify variation in nano-scale precipitates.
- A quantitative measurement of hydrogen concentration in samples and, compare properties with similar hydrogen concentration in oven-charged samples to delineate the effect of hydrogen on the crack surface.
- Utilise computational means to understand the stress state within the sample and its interaction with hydrogen.
- As concentration of hydrogen dissolved in the material is dependent on hydrogen pressure, quantifying the effect of pressure variation is recommended.
- Study the HE behaviour of AM samples produced from conventional powders, to identify the effect of powder source on HE.
- Quantitatively study the anisotropy in crack propagation and hydrogen transport in two directions of horizontally built cylindrical samples.

- For future application it might be interesting to also study hydrogen-enhanced fatigue of AM Inconel 718, especially considering observed herein microstructural anisotropy.

A

Additional information on mechanical testing

A.1. Calibration of Instron Extensometer in MTS

Due to unavailability of MTS extensometer, an instron extensometer is used to measure the elongation in the samples. A separate calibration is required as it is not fully compatible. To calibrate it, a separate experiment where signal from the extensometer is collected for a known displacement. At least 10 known displacement values are selected. The calibration graph (shown in Figure A.1) is plotted to verify that the extensometer signals correspond linearly with the elongation. Linear regression is then used to determine the coefficient of the line, and was found to be 8.1. This coefficient is then used to determine the elongation of the samples during the experiment. The calibration is performed multiple times to check for any variations.

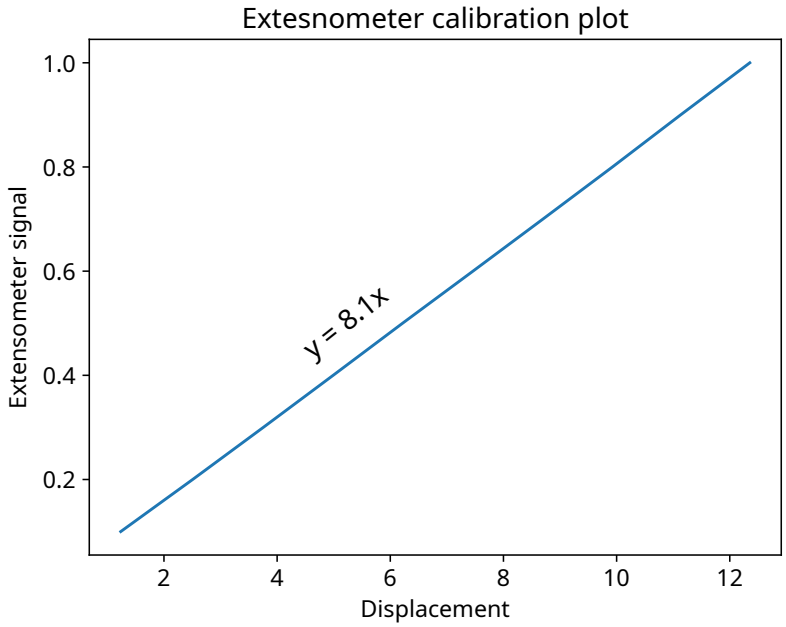

Figure A.1: Extensometer calibration curve.

A.2. Strain After Extensometer Removal

The cross head displacement can be written as :

$$\delta_{ch} = \delta_{sp} + \delta_{mach} \tag{A.1}$$

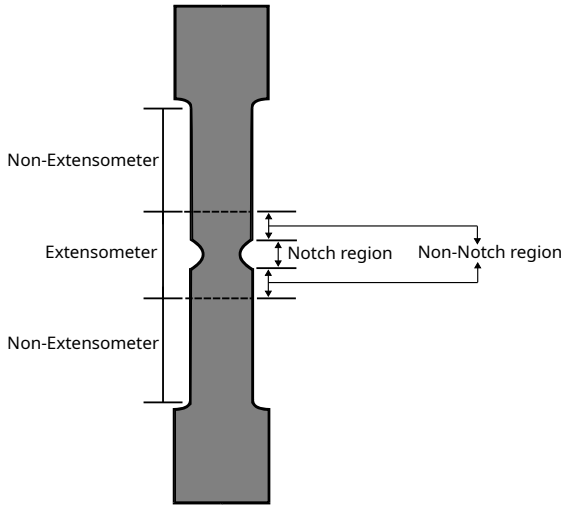

Figure A.2: Position of extensometer during the experiment.

where δ_{ch}, δ_{sp} and δ_{mach} are crosshead displacement signal, displacement contribution from specimen and the displacement contribution from the machine components respectively. The following assumptions are made to determine the strain after extenso removal:

- The non-notch region remains elastic throughout the experiment.
- The machine components remain elastic throughout the experiment.
- The displacement contribution from machine and non-notch region is negligible compared to the displacement due to plastic strain from the notch region.
- The elastic modulus of the material is known.

Equation A.1 is rewritten as

$$\delta_{mach} = \delta_{ch} - \delta_{sp} \tag{A.2}$$

From Figure A.2,the total displacement form the sample contains contribution from the extensometer measurement and non-extensometer region and can be written as:

$$\delta_{sp} = \delta_{extenso} + \delta_{non-extenso}$$

$$\delta_{non-extenso} = \frac{l_{non-extenso}\,\sigma}{E_{mod}}$$

where $l_{nonextenso}$ is 30 mm, σ is the stress acting in the non-notch region and E_{mod} is the elastic modulus determined from the non notch region of the material. A python script is utilised to perform a linear regression using the data points of the experiment in the linear region to determined the machine coefficient. It is then used to find the strain in the sample after extensometer removal.

B

Fracture surface

B.1. Fracture Surface

B.1.1. Samples tested in ambient conditions

Additional fracture surfaces images of samples tested in ambient conditions are provided here.

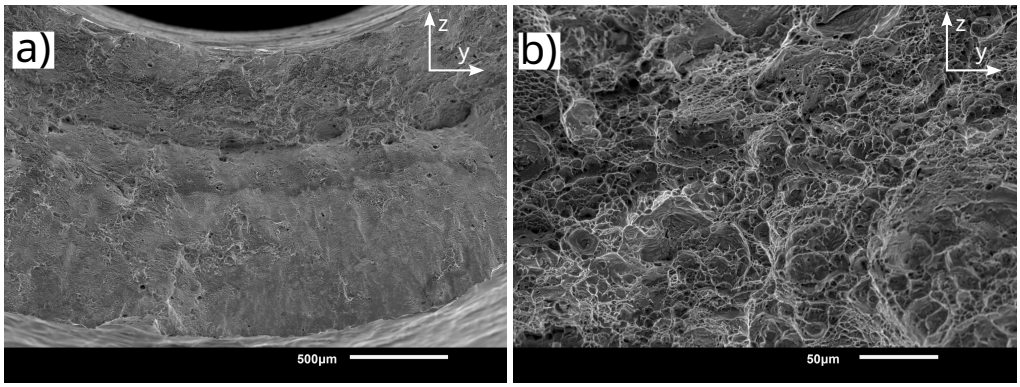

Figure B.1: Fracture surface of conventional samples tested in air showing ductile failure. a) overview b) Micro Voids.

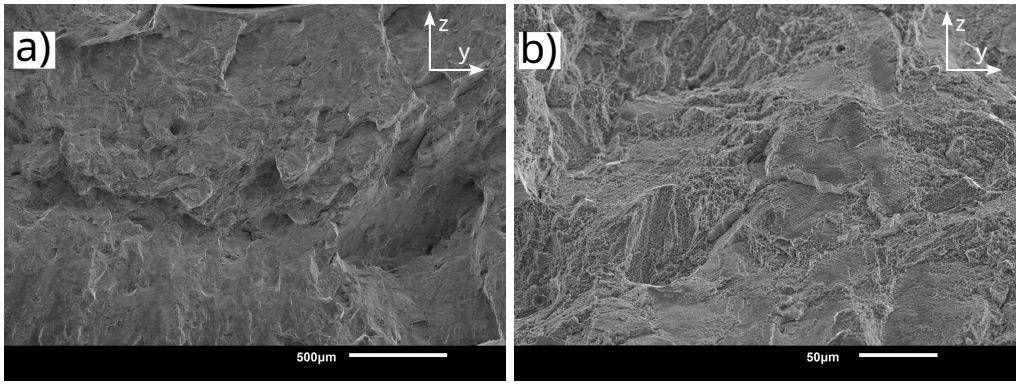

Figure B.2: Fracture surface of AM-HT samples tested in air showing ductile failure. a) overview b) Micro Voids.

B.1.2. HE in AM samples

Fracture surfaces of same AM sample showing anisotropic embrittled region. In Figure B.3, it can be seen that the HE region aligns with the build direction (z-axis) and no significant embrittlement is observed in other direction (y-axis). This occurs even though a defect is seen along y direction Figure B.3d). This shows that the HE is more influenced by the build direction than the presence of inner defects.

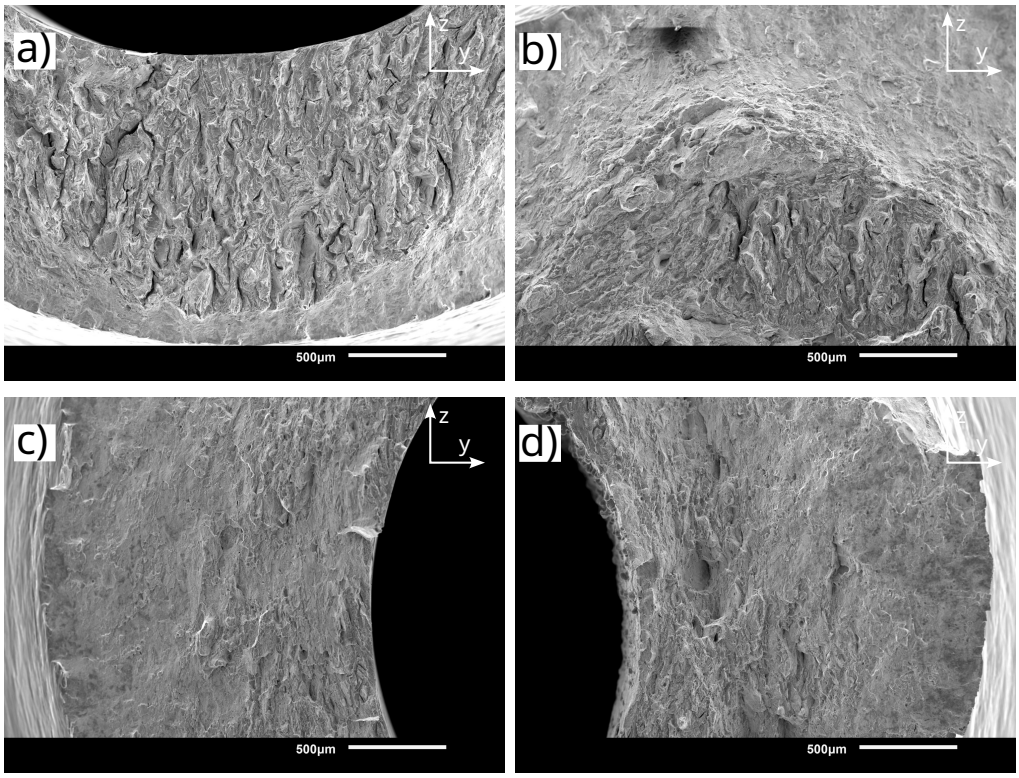

Figure B.3: Different regions of a single hydrogen embrittled AM sample.

B.2. Defects from Machining in AM samples

Non-machined regions in the inner-surface of AM samples due to dimensional inaccuracy. They are referred to as defects in the sample.

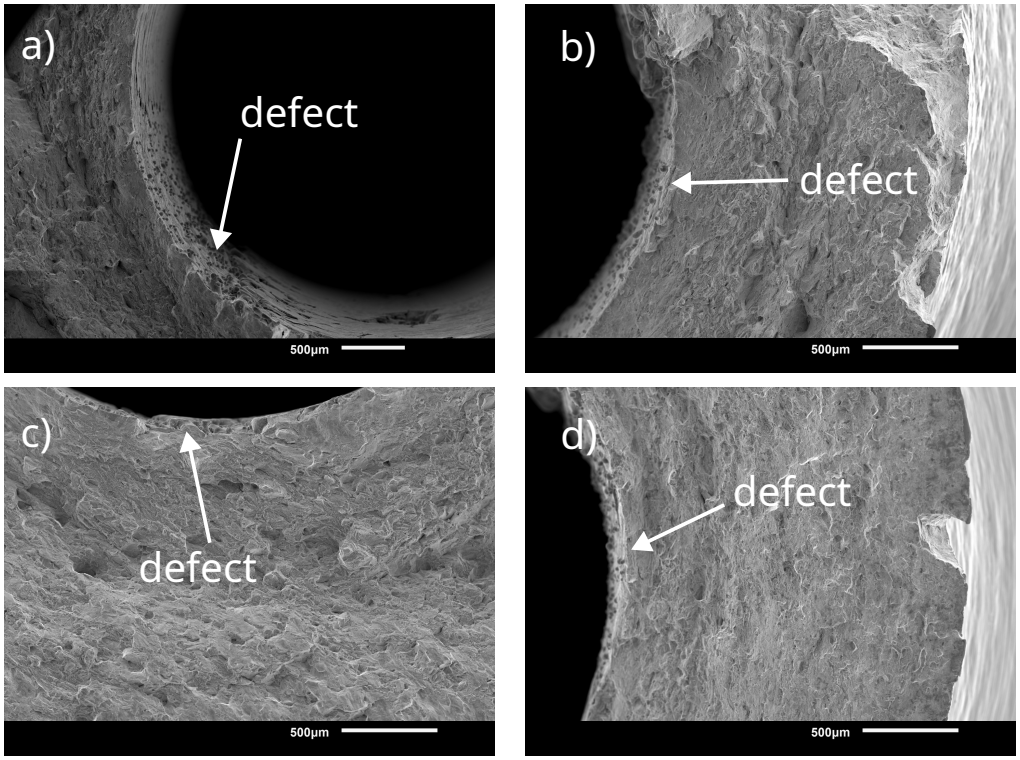

Figure B.4: Defects observed on the inner surface of various samples.

C

Geometry file for diffusion simulation

The gmsh script for generating the geometry for the simulation of diffusion is provided below. It is saved as a .geo file in the python script directory.

```
SetFactory("OpenCASCADE");
//+ Define the boundary points
Point(1) = {2, 0, 0, 1.0};
Point(2) = {5, 0, 0, 1.0};
Point(3) = {5, 20, 0, 1.0};
Point(4) = {2, 20, 0, 1.0};
Circle(1) = {8, 0, 0, 4, 0, 2*Pi};
//+ Connect the points
Line(2) = {2, 1};
Line(3) = {1, 4};
Line(4) = {4, 3};
Line(5) = {3, 2};
//+ define centre for the circle
Point(6) = {2, 4, 0, 1.0};
Point(7) = {5, 4, 0, 1.0};
Point(9) = {3.5, 4, 0, 1.0};
Line(6) = {6, 9};
Line(7) = {9, 7};
Point(10) = {4.5, 1.5, 0, 1.0};
Point(11) = {3.5, 1.5, 0, 1.0};
Point(12) = {3.5, 0, 0, 1.0};
Point(13) = {3.5, 2.64, 0, 1.0};
Line(8) = {12, 11};
Line(9) = {11, 13};
Line(10) = {13, 9};
Line(11) = {11, 10};
//+ Generate points at the point of intersection
Coherence;
Line(25) = {13, 15};
//+ remove the unnecessary parts
```

```
Recursive Delete {
  Curve{24}; Curve{16}; Curve{22}; Curve{11}; Curve{14};
}
//+
Curve Loop(1) = {20, -7, -6, 19, 4};
//+ generate surface
Plane Surface(1) = {1};
Curve Loop(2) = {18, 6, -10, -9, -8, 15};
Plane Surface(2) = {2};
Curve Loop(3) = {21, -25, 10, 7};
Plane Surface(3) = {3};
Curve Loop(4) = {12, -23, 9, 25};
Plane Surface(4) = {4};
Curve Loop(5) = {8, 23, 13, 17};
Plane Surface(5) = {5};
//+ generate names for the Surface
Physical Curve("outside", 26) = {20, 21, 12, 13};
Physical Curve("inside", 27) = {18, 19};
Physical Surface("bulk1", 28) = {1};
Physical Surface("bulk2", 29) = {3};
Physical Surface("bulk3", 30) = {4};
Physical Surface("bulk4", 31) = {5};
Physical Surface("bulk5", 32) = {2};
# defining the mesh
Transfinite Curve {20} = 600 Using Progression 0.997;
Transfinite Curve {19} = 600 Using Progression 1.003;
Transfinite Curve {6, 15} = 100 Using Progression 1;
Transfinite Curve {21, 10} = 50 Using Progression 1;
Transfinite Curve {7, 25, 23, 17} = 100 Using Progression 1;
Transfinite Curve {10, 21} = 150 Using Progression 1;
Transfinite Curve {9, 12} = 150 Using Progression 1;
Transfinite Curve {8, 13} = 150 Using Progression 1;
Transfinite Curve {18} = 448 Using Progression 1;
Transfinite Curve {4} = 199 Using Progression 1;
Transfinite Surface {1}={3, 7, 6, 4};
Transfinite Surface {3};
Transfinite Surface {4};
Transfinite Surface {5};
Transfinite Surface {2} = {6, 9, 12, 18};
Recombine Surface {1};
Recombine Surface {3};
Recombine Surface {4};
```

Bibliography

[1] Ellen MacArthur et al. “Towards the circular economy”. In: *Journal of Industrial Ecology* 2.1 (2013), pp. 23–44.

[2] G.W. Crabtree and M.S. Dresselhaus. “The Hydrogen Fuel Alternative”. In: *MRS Bulletin* 33.4 (2008), pp. 421–428. DOI: 10.1557/mrs2008.84.

[3] Jianhong He et al. “Effect of Hydrogen on Deformation Structure of Inconel 718”. In: *Materials Transactions, JIM* 35.10 (1994), pp. 689–694. DOI: 10.2320/matertrans1989.35.689. URL: https://doi.org/10.2320/matertrans1989.35.689.

[4] RP Jewett and JA Halchak. “The use of alloy 718 in the space shuttle main engine”. In: *Superalloys* 718.625 (1991), pp. 749–760.

[5] Sebastian Soller et al. “Selective laser melting (SLM) of Inconel 718 and stainless steel injectors for liquid rocket engines”. In: *Space Propulsion 2016 Proceedings* (2016).

[6] Mohd Javaid et al. “Role of additive manufacturing applications towards environmental sustainability”. In: *Advanced Industrial and Engineering Polymer Research* 4.4 (Oct. 2021), pp. 312–322. DOI: 10.1016/j.aiepr.2021.07.005. URL: https://doi.org/10.1016/j.aiepr.2021.07.005.

[7] T. DebRoy et al. “Additive manufacturing of metallic components – Process, structure and properties”. In: *Progress in Materials Science* 92 (2018), pp. 112–224. ISSN: 0079-6425. DOI: https://doi.org/10.1016/j.pmatsci.2017.10.001. URL: https://www.sciencedirect.com/science/article/pii/S0079642517301172.

[8] *A Review of Hydrogen Embrittlement of Nickel-Based Alloys for Oil and Gas Applications*. NACE CORROSION. Apr. 2021. URL: https://onepetro.org/NACECORR/proceedings-pdf/CORR21/10-CORR21/D101S039R005/2446778/nace-2021-16705.pdf.

[9] J.R. Davis. *Metals Handbook, Desk Edition (2nd Edition)*. ASM International, 1998. Chap. Nickel and Nickel Alloys. ISBN: 978-0-87170-654-6. URL: https://app.knovel.com/hotlink/khtml/id:kt010QU1A6/metals-handbook-desk/uses-of-nickel.

[10] Enes Akca and Ali Gürsel. “A review on superalloys and IN718 nickel-based INCONEL superalloy”. In: *Periodicals of Engineering and Natural Sciences (PEN)* 3.1 (2015). DOI: 10.21533/pen.v3i1.43.

[11] Xiaoliang Liang, Zhanqiang Liu, and Bing Wang. “State-of-the-art of surface integrity induced by tool wear effects in machining process of titanium and nickel alloys: A review”. In: *Measurement* 132 (2019), pp. 150–181. ISSN: 0263-2241. DOI: 10.1016/j.measurement.2018.09.045.

[12] Ian Gibson, David Rosen, and Brent Stucker. *Additive Manufacturing Technologies 3D Printing, Rapid Prototyping, and Direct Digital Manufacturing Second Edition*. Second. Springer-Verlag New York, 2010. ISBN: 978-1-4939-4455-2. DOI: 10.1007/978-1-4939-2113-3.

[13] D D Gu et al. “Laser additive manufacturing of metallic components: materials, processes and mechanisms”. In: *International Materials Reviews* 57.3 (2012), pp. 133–164. DOI: 10.1179/1743280411Y.0000000014. eprint: https://doi.org/10.1179/1743280411Y.0000000014. URL: https://doi.org/10.1179/1743280411Y.0000000014.

[14] Wakshum M. Tucho et al. “Investigation of effects of process parameters on microstructure and hardness of SLM manufactured SS316L”. In: *Journal of Alloys and Compounds* 740 (2018), pp. 910–925. ISSN: 0925-8388. DOI: https://doi.org/10.1016/j.jallcom.2018.01.098. URL: https://www.sciencedirect.com/science/article/pii/S0925838818300999.

[15] William E Luecke and John A Slotwinski. “Mechanical properties of austenitic stainless steel made by additive manufacturing”. In: *Journal of research of the National Institute of Standards and Technology* 119 (2014), p. 398.

[16] J.P. Kruth et al. “Selective laser melting of iron-based powder”. In: *Journal of Materials Processing Technology* 149.1 (2004). 14th Interntaional Symposium on Electromachining (ISEM XIV), pp. 616–622. ISSN: 0924-0136. DOI: https://doi.org/10.1016/j.jmatprotec.2003.11.051. URL: https://www.sciencedirect.com/science/article/pii/S0924013604002201.

[17] E. Hosseini and V.A. Popovich. “A review of mechanical properties of additively manufactured Inconel 718”. In: *Additive Manufacturing* 30 (Dec. 2019), p. 100877. DOI: 10.1016/j.addma.2019.100877. URL: https://doi.org/10.1016/j.addma.2019.100877.

[18] Roger C. Reed. *Superalloys - Fundamentals and Applications*. Cambridge University Press, 2006. Chap. 2. The Physical Metallurgy of Nickel and its Alloys. ISBN: 978-0-521-85904-2. URL: https://app.knovel.com/hotlink/khtml/id:kt009AQKG1/superalloys-fundamentals/physical-metallurgy-nickel.

[19] Blaine Geddes, Hugo Leon, and Xiao Huang. *Superalloys*. ASM International, Nov. 2010. DOI: 10.31399/asm.tb.sap.9781627083133. URL: https://doi.org/10.31399/asm.tb.sap.9781627083133.

[20] Mohammad Javad Sohrabi, Hamed Mirzadeh, and Mohsen Rafiei. “Solidification behavior and Laves phase dissolution during homogenization heat treatment of Inconel 718 superalloy”. In: *Vacuum* 154 (Aug. 2018), pp. 235–243. DOI: 10.1016/j.vacuum.2018.05.019. URL: https://doi.org/10.1016/j.vacuum.2018.05.019.

[21] T. Antonsson and H. Fredriksson. “The effect of cooling rate on the solidification of INCONEL 718”. In: *Metallurgical and Materials Transactions B* 36.1 (Feb. 2005), pp. 85–96. DOI: 10.1007/s11663-005-0009-0. URL: https://doi.org/10.1007/s11663-005-0009-0.

[22] Dongyun Zhang et al. “Comparison of microstructures and mechanical properties of Inconel 718 alloy processed by selective laser melting and casting”. In: *Materials Science and Engineering: A* 724 (May 2018), pp. 357–367. DOI: 10.1016/j.msea.2018.03.073. URL: https://doi.org/10.1016/j.msea.2018.03.073.

[23] Yen-Ling Kuo, Shota Horikawa, and Koji Kakehi. "The effect of interdendritic δ phase on the mechanical properties of Alloy 718 built up by additive manufacturing". In: *Materials & Design* 116 (Feb. 2017), pp. 411–418. DOI: 10.1016/j.matdes.2016.12.026. URL: https://doi.org/10.1016/j.matdes.2016.12.026.

[24] Dunyong Deng et al. "Microstructure and mechanical properties of Inconel 718 produced by selective laser melting: Sample orientation dependence and effects of post heat treatments". In: *Materials Science and Engineering: A* 713 (Jan. 2018), pp. 294–306. DOI: 10.1016/j.msea.2017.12.043. URL: https://doi.org/10.1016/j.msea.2017.12.043.

[25] Dongyun Zhang et al. "Effect of standard heat treatment on the microstructure and mechanical properties of selective laser melting manufactured Inconel 718 superalloy". In: *Materials Science and Engineering: A* 644 (Sept. 2015), pp. 32–40. DOI: 10.1016/j.msea.2015.06.021. URL: https://doi.org/10.1016/j.msea.2015.06.021.

[26] David J Newell. *Solution Anneal Heat Treatment to Enhance Mechanical Performance of Additively Manufactured IN718*. Tech. rep. AIR FORCE INSTITUTE OF TECHNOLOGY WRIGHT-PATTERSON AFB OH WRIGHT-PATTERSON ..., 2020.

[27] *Nickel Alloy, Corrosion and Heat-Resistant, Bars, Forgings, and Rings 52.5Ni - 19Cr - 3.0Mo - 5.1Cb (Nb) - 0.90Ti - 0.50Al - 18Fe Consumable Electrode or Vacuum Induction Melted 1775 °F (968 °C) Solution and Precipitation Heat Treated*. DOI: 10.4271/ams5663n. URL: https://doi.org/10.4271/ams5663n.

[28] *Nickel Alloy, Corrosion and Heat-Resistant, Investment Castings 52.5Ni - 19Cr - 3.0Mo - 5.1Cb(Nb) - 0.90Ti - 0.60Al - 18Fe Vacuum Melted Homogenization and Solution Heat Treated*. DOI: 10.4271/ams5383f. URL: https://doi.org/10.4271/ams5383f.

[29] *Nickel Alloy, Corrosion and Heat Resistant, Bars, Forgings, and Rings, 52.5Ni - 19Cr - 3.0Mo - 5.1Cb - 0.90Ti - 0.50Al - 18Fe, Consumable Electrode or Vacuum Induction Melted, 1950 °F (1066 °C) Solution Heat Treated, Precipitation Hardenable*. DOI: 10.4271/ams5664e. URL: https://doi.org/10.4271/ams5664e.

[30] Yang Gao et al. "Effect of δ phase on high temperature mechanical performances of Inconel 718 fabricated with SLM process". In: *Materials Science and Engineering: A* 767 (Nov. 2019), p. 138327. DOI: 10.1016/j.msea.2019.138327. URL: https://doi.org/10.1016/j.msea.2019.138327.

[31] Davuluri Sindhura, Mantha Venkata Sravya, and G. V. S. Murthy. "Comprehensive Microstructural Evaluation of Precipitation in Inconel 718". In: *Metallography, Microstructure, and Analysis* 8.2 (Jan. 2019), pp. 233–240. DOI: 10.1007/s13632-018-00513-0. URL: https://doi.org/10.1007/s13632-018-00513-0.

[32] Xing Li et al. "Effect of heat treatment on microstructure evolution of Inconel 718 alloy fabricated by selective laser melting". In: *Journal of Alloys and Compounds* 764 (2018), pp. 639–649. ISSN: 0925-8388. DOI: https://doi.org/10.1016/j.jallcom.2018.06.112. URL: https://www.sciencedirect.com/science/article/pii/S0925838818322333.

[33] E. Chlebus et al. “Effect of heat treatment on the microstructure and mechanical properties of Inconel 718 processed by selective laser melting”. In: *Materials Science and Engineering: A* 639 (July 2015), pp. 647–655. DOI: 10.1016/j.msea.2015.05.035. URL: https://doi.org/10.1016/j.msea.2015.05.035.

[34] Peng Liu et al. “Microstructural evolution and phase transformation of Inconel 718 alloys fabricated by selective laser melting under different heat treatment”. In: *Journal of Manufacturing Processes* 39 (Mar. 2019), pp. 226–232. DOI: 10.1016/j.jmapro.2019.02.029. URL: https://doi.org/10.1016/j.jmapro.2019.02.029.

[35] V.A. Popovich et al. “Functionally graded Inconel 718 processed by additive manufacturing: Crystallographic texture, anisotropy of microstructure and mechanical properties”. In: *Materials & Design* 114 (Jan. 2017), pp. 441–449. DOI: 10.1016/j.matdes.2016.10.075. URL: https://doi.org/10.1016/j.matdes.2016.10.075.

[36] Zhichao Zhang et al. “Hydrogen diffusion under the effect of stress and temperature gradients”. In: *Journal of Physics: Conference Series* 2116.1 (Nov. 2021), p. 012037. DOI: 10.1088/1742-6596/2116/1/012037. URL: https://doi.org/10.1088/1742-6596/2116/1/012037.

[37] F. Brenne et al. “Microstructural design of Ni-base alloys for high-temperature applications: impact of heat treatment on microstructure and mechanical properties after selective laser melting”. In: *Progress in Additive Manufacturing* 1.3-4 (July 2016), pp. 141–151. DOI: 10.1007/s40964-016-0013-8. URL: https://doi.org/10.1007/s40964-016-0013-8.

[38] Judy Schneider, Benjamin Lund, and Myles Fullen. “Effect of heat treatment variations on the mechanical properties of Inconel 718 selective laser melted specimens”. In: *Additive Manufacturing* 21 (May 2018), pp. 248–254. DOI: 10.1016/j.addma.2018.03.005. URL: https://doi.org/10.1016/j.addma.2018.03.005.

[39] Wenpu Huang et al. “Heat treatment of Inconel 718 produced by selective laser melting: Microstructure and mechanical properties”. In: *Materials Science and Engineering: A* 750 (Mar. 2019), pp. 98–107. DOI: 10.1016/j.msea.2019.02.046. URL: https://doi.org/10.1016/j.msea.2019.02.046.

[40] Thomas G. Gallmeyer et al. “Knowledge of process-structure-property relationships to engineer better heat treatments for laser powder bed fusion additive manufactured Inconel 718”. In: *Additive Manufacturing* 31 (Jan. 2020), p. 100977. DOI: 10.1016/j.addma.2019.100977. URL: https://doi.org/10.1016/j.addma.2019.100977.

[41] Shuya Zhang et al. “Strengthening mechanisms in selective laser-melted Inconel718 superalloy”. In: *Materials Science and Engineering: A* 812 (Apr. 2021), p. 141145. DOI: 10.1016/j.msea.2021.141145. URL: https://doi.org/10.1016/j.msea.2021.141145.

[42] AMS F Corrosion Heat Resistant Alloys Committee. *Nickel Alloy, Corrosion and Heat-Resistant, Bars, Forgings, and Rings 52.5Ni - 19Cr - 3.0Mo - 5.1Cb (Nb) - 0.90Ti - 0.50AI - 18Fe Consumable Electrode or Vacuum Induction Melted 1775 °F (968 °C) Solution Heat Treated, Precipitation-Hardenable*. June 2016. DOI: https://doi.org/10.4271/AMS5662N. URL: https://doi.org/10.4271/AMS5662N.

[43] Xiaoming Zhao et al. "Study on microstructure and mechanical properties of laser rapid forming Inconel 718". In: *Materials Science and Engineering: A* 478.1-2 (Apr. 2008), pp. 119–124. DOI: 10.1016/j.msea.2007.05.079. URL: https://doi.org/10.1016/j.msea.2007.05.079.

[44] Konrad Gruber et al. "Evaluation of Inconel 718 Metallic Powder to Optimize the Reuse of Powder and to Improve the Performance and Sustainability of the Laser Powder Bed Fusion (LPBF) Process". In: *Materials* 14.6 (Mar. 2021), p. 1538. DOI: 10.3390/ma14061538. URL: https://doi.org/10.3390/ma14061538.

[45] Feng Yi et al. "Effect of powder reuse on powder characteristics and properties of Inconel 718 parts produced by selective laser melting". In: *Journal of Materials Research and Technology* 13 (July 2021), pp. 524–533. DOI: 10.1016/j.jmrt.2021.04.091. URL: https://doi.org/10.1016/j.jmrt.2021.04.091.

[46] L.C. Ardila et al. "Effect of IN718 Recycled Powder Reuse on Properties of Parts Manufactured by Means of Selective Laser Melting". In: *Physics Procedia* 56 (2014), pp. 99–107. DOI: 10.1016/j.phpro.2014.08.152. URL: https://doi.org/10.1016/j.phpro.2014.08.152.

[47] Mang Ni et al. "Anisotropic tensile behavior of in situ precipitation strengthened Inconel 718 fabricated by additive manufacturing". In: *Materials Science and Engineering: A* 701 (July 2017), pp. 344–351. DOI: 10.1016/j.msea.2017.06.098. URL: https://doi.org/10.1016/j.msea.2017.06.098.

[48] Dunyong Deng et al. "Microstructure and anisotropic mechanical properties of EBM manufactured Inconel 718 and effects of post heat treatments". In: *Materials Science and Engineering: A* 693 (May 2017), pp. 151–163. DOI: 10.1016/j.msea.2017.03.085. URL: https://doi.org/10.1016/j.msea.2017.03.085.

[49] Nadia Kouraytem et al. "A recrystallization heat-treatment to reduce deformation anisotropy of additively manufactured Inconel 718". In: *Materials & Design* 198 (Jan. 2021), p. 109228. DOI: 10.1016/j.matdes.2020.109228. URL: https://doi.org/10.1016/j.matdes.2020.109228.

[50] S.Y. Liu et al. "The effect of energy density on texture and mechanical anisotropy in selective laser melted Inconel 718". In: *Materials & Design* 191 (June 2020), p. 108642. DOI: 10.1016/j.matdes.2020.108642. URL: https://doi.org/10.1016/j.matdes.2020.108642.

[51] Pankaj Kumar et al. "Influence of laser processing parameters on porosity in Inconel 718 during additive manufacturing". In: *The International Journal of Advanced Manufacturing Technology* 103.1-4 (2019), pp. 1497–1507.

[52] Zhenbo Zhang et al. "Hydrogen assisted crack initiation and propagation in a nickel-based superalloy". In: *Acta Materialia* 113 (July 2016), pp. 272–283. DOI: 10.1016/j.actamat.2016.05.003. URL: https://doi.org/10.1016/j.actamat.2016.05.003.

[53] Liufa Liu et al. “Effects of precipitation phases on the hydrogen embrittlement sensitivity of Inconel 718”. In: *Science and Technology of Advanced Materials* 3.4 (Jan. 2002), pp. 335–344. DOI: 10.1016/s1468-6996(02)00039-6. URL: https://doi.org/10.1016/s1468-6996(02)00039-6.

[54] J. Xu et al. “Hydrogen permeation behavior in IN718 and GH761 superalloys”. In: *Metallurgical and Materials Transactions A* 25.3 (Mar. 1994), pp. 539–544. DOI: 10.1007/bf02651595. URL: https://doi.org/10.1007/bf02651595.

[55] Qian Liu and Andrej Atrens. “A critical review of the influence of hydrogen on the mechanical properties of medium-strength steels”. In: *Corrosion Reviews* 31.3-6 (2013), pp. 85–103. DOI: doi:10.1515/corrrev-2013-0023. URL: https://doi.org/10.1515/corrrev-2013-0023.

[56] Xinfeng Li et al. “Review of Hydrogen Embrittlement in Metals: Hydrogen Diffusion, Hydrogen Characterization, Hydrogen Embrittlement Mechanism and Prevention”. In: *Acta Metallurgica Sinica (English Letters)* 33.6 (Apr. 2020), pp. 759–773. DOI: 10.1007/s40195-020-01039-7. URL: https://doi.org/10.1007/s40195-020-01039-7.

[57] Adolf Sieverts. “Die Löslichkeit von Wasserstoff in Kupfer, Eisen und Nickel”. In: *Zeitschrift für Physikalische Chemie* 77U.1 (1911), pp. 591–613. DOI: doi:10.1515/zpch-1911-7737. URL: https://doi.org/10.1515/zpch-1911-7737.

[58] C. San Marchi, B.P. Somerday, and S.L. Robinson. “Permeability, solubility and diffusivity of hydrogen isotopes in stainless steels at high gas pressures”. In: *International Journal of Hydrogen Energy* 32.1 (2007), pp. 100–116. ISSN: 0360-3199. DOI: https://doi.org/10.1016/j.ijhydene.2006.05.008. URL: https://www.sciencedirect.com/science/article/pii/S0360319906001753.

[59] Yang He et al. “Diffusion coefficient of hydrogen interstitial atom in α-Fe, γ-Fe and ϵ-Fe crystals by first-principle calculations”. In: *International Journal of Hydrogen Energy* 42.44 (2017), pp. 27438–27445. ISSN: 0360-3199. DOI: https://doi.org/10.1016/j.ijhydene.2017.08.212. URL: https://www.sciencedirect.com/science/article/pii/S0360319917335577.

[60] Chris San Marchi and Brian P Somerday. “Thermodynamics of Gaseous Hydrogen and Hydrogen Transport in Metals”. In: *MRS Proceedings* 1098 (2008). DOI: 10.1557/proc-1098-hh08-01. URL: https://doi.org/10.1557/proc-1098-hh08-01.

[61] Niklas Ehrlin, Christina Bjerkén, and Martin Fisk. “Cathodic hydrogen charging of Inconel 718”. In: *AIMS Materials Science* 3.4 (2016), pp. 1350–1364. DOI: 10.3934/matersci.2016.4.1350. URL: https://doi.org/10.3934/matersci.2016.4.1350.

[62] I. Maroef et al. “Hydrogen trapping in ferritic steel weld metal”. In: *International Materials Reviews* 47.4 (Aug. 2002), pp. 191–223. DOI: 10.1179/095066002225006548. URL: https://doi.org/10.1179/095066002225006548.

[63] Stan Lynch. “Hydrogen embrittlement phenomena and mechanisms”. In: *Corrosion Reviews* 30.3-4 (2012), pp. 105–123. DOI: doi:10.1515/corrrev-2012-0502. URL: https://doi.org/10.1515/corrrev-2012-0502.

[64] A Turnbull et al. “Hydrogen transport in nickel-base alloys”. In: *Metallurgical Transactions A* 23.12 (1992), pp. 3231–3244. DOI: https://doi.org/10.1007/BF02663432.

[65] SP Lynch. “Progress towards understanding mechanisms of hydrogen embrittlement and stress corrosion cracking”. In: *CORROSION 2007*. OnePetro. 2007.

[66] L Fournier, D Delafosse, and T Magnin. “Cathodic hydrogen embrittlement in alloy 718”. In: *Materials Science and Engineering: A* 269.1 (1999), pp. 111–119. ISSN: 0921-5093. DOI: https://doi.org/10.1016/S0921-5093(99)00167-7. URL: https://www.sciencedirect.com/science/article/pii/S0921509399001677.

[67] C. San Marchi. “16 - Hydrogen embrittlement of stainless steels and their welds”. In: *Gaseous Hydrogen Embrittlement of Materials in Energy Technologies*. Ed. by Richard P. Gangloff and Brian P. Somerday. Vol. 2. Woodhead Publishing Series in Metals and Surface Engineering. Woodhead Publishing, 2012, pp. 592–623. ISBN: 978-1-84569-677-1. DOI: https://doi.org/10.1533/9780857093899.3.592. URL: https://www.sciencedirect.com/science/article/pii/B9781845696771500168.

[68] C. San Marchi et al. “Effect of High-Pressure Hydrogen Gas on Fracture of Austenitic Steels”. In: *Journal of Pressure Vessel Technology* 130.4 (Aug. 2008). 041401. ISSN: 0094-9930. DOI: 10.1115/1.2967833. eprint: https://asmedigitalcollection.asme.org/pressurevesseltech/article-pdf/130/4/041401/5875919/041401_1.pdf. URL: https://doi.org/10.1115/1.2967833.

[69] *Standard Test Method for Determination of Susceptibility of Metals to Embrittlement in Hydrogen Containing Environments at High Pressure, High Temperature, or Both*. ASTM G142-98. ASTM Standards, 2016.

[70] K.A. Nibur and B.P. Somerday. “7 - Fracture and fatigue test methods in hydrogen gas”. In: *Gaseous Hydrogen Embrittlement of Materials in Energy Technologies*. Ed. by Richard P. Gangloff and Brian P. Somerday. Vol. 2. Woodhead Publishing Series in Metals and Surface Engineering. Woodhead Publishing, 2012, pp. 195–236. ISBN: 978-1-84569-677-1. DOI: https://doi.org/10.1533/9780857093899.2.195.

[71] Tim Boot et al. “In-Situ Hollow Sample Setup Design for Mechanical Characterisation of Gaseous Hydrogen Embrittlement of Pipeline Steels and Welds”. In: *Metals* 11.8 (2021), p. 1242.

[72] JP Fidelle. “Closing Commentary—IHE-HEE: Are They the Same?” In: *Hydrogen Embrittlement Testing*. ASTM International, 1974.

[73] HG Nelson. “Closing Commentary—IHE-HEE: Are They the Same?” In: *Hydrogen Embrittlement Testing*. ASTM International, 1974.

[74] Yakai Zhao et al. “The role of hydrogen in hardening/softening steel: Influence of the charging process”. In: *Scripta Materialia* 107 (2015), pp. 46–49. ISSN: 1359-6462. DOI: https://doi.org/10.1016/j.scriptamat.2015.05.017. URL: https://www.sciencedirect.com/science/article/pii/S1359646215002031.

[75] Dong-Hyun Lee et al. “Hydrogen-assisted failure in Inconel 718 fabricated by laser powder bed fusion: The role of solidification substructure in the embrittlement”. In: *Scripta Materialia* 207 (Jan. 2022), p. 114308. DOI: 10.1016/j.scriptamat.2021.114308.

[76] Xinfeng Li et al. “Hydrogen-assisted failure of laser melting additive manufactured IN718 superalloy”. In: *Corrosion Science* 160 (Nov. 2019), p. 108171. DOI: 10.1016/j.corsci.2019.108171. URL: https://doi.org/10.1016/j.corsci.2019.108171.

[77] F Aiello et al. “Hydrogen diffusivity and tensile properties degradation in SLMed Inconel 718”. In: *IOP Conference Series: Materials Science and Engineering* 1214.1 (Jan. 2022), p. 012002. DOI: 10.1088/1757-899x/1214/1/012002. URL: https://doi.org/10.1088/1757-899x/1214/1/012002.

[78] Hamza Khalid and B. Mansoor. “Hydrogen Embrittlement in Nickel-Base Superalloy 718”. In: *Recent Developments in Analytical Techniques for Corrosion Research*. Springer International Publishing, 2022, pp. 279–306. DOI: 10.1007/978-3-030-89101-5_13. URL: https://doi.org/10.1007/978-3-030-89101-5_13.

[79] M.C. Rezende et al. “Hydrogen embrittlement in nickel-based superalloy 718: Relationship between $\gamma' + \gamma''$ precipitation and the fracture mode”. In: *International Journal of Hydrogen Energy* 40.47 (Dec. 2015), pp. 17075–17083. DOI: 10.1016/j.ijhydene.2015.07.053. URL: https://doi.org/10.1016/j.ijhydene.2015.07.053.

[80] Liufa Liu et al. “Study of the effect of δ phase on hydrogen embrittlement of Inconel 718 by notch tensile tests”. In: *Corrosion Science* 47.2 (Feb. 2005), pp. 355–367. DOI: 10.1016/j.corsci.2004.06.008. URL: https://doi.org/10.1016/j.corsci.2004.06.008.

[81] J. Hesketh et al. “Influence of additive manufacturing by laser powder bed fusion on the susceptibility of Alloy 718 to hydrogen embrittlement”. In: *Corrosion Engineering, Science and Technology* 56.6 (May 2021), pp. 565–574. DOI: 10.1080/1478422x.2021.1921336. URL: https://doi.org/10.1080/1478422x.2021.1921336.

[82] *VDM metals GmbH*. URL: https://www.vdm-metals.com/en/alloy718.

[83] *Book of Standards*. ASTMB637-18. West Conshohocken, PA: ASTM Standards, 2018. DOI: 10.1520/B0637-18.

[84] *Fenice*. URL: https://f3nice.com/.

[85] *Standard Specification for Additive Manufacturing Nickel Alloy (UNS N07718) with Powder Bed Fusion*. ASTMF3055-14. West Conshohocken, PA: ASTM Standards, 2021.

[86] Michihiko Nagumo. “Characteristic Features of Deformation and Fracture in Hydrogen Embrittlement”. In: *Fundamentals of Hydrogen Embrittlement*. Springer Singapore, 2016, pp. 137–165. DOI: 10.1007/978-981-10-0161-1_7. URL: https://doi.org/10.1007/978-981-10-0161-1_7.

[87] Tim Boot. “Assessing the susceptibility of existing pipelines to Hydrogen Embrittlement: A combined modelling and in-situ experimental approach”. In: (2020). URL: http://resolver.tudelft.nl/uuid:fa21ef89-cf8e-47ca-92fe-9301b23cfaa1.

[88] Jonathan E. Guyer, Daniel Wheeler, and James A. Warren. “FiPy: Partial Differential Equations with Python”. In: *Computing in Science and Engineering* 11.3 (2009), pp. 6–15. DOI: 10.1109/MCSE.2009.52. URL: http://www.ctcms.nist.gov/fipy.

[89] Christophe Geuzaine and Jean-François Remacle. “Gmsh: A 3-D finite element mesh generator with built-in pre- and post-processing facilities”. In: *International Journal for Numerical Methods in Engineering* 79.11 (May 2009), pp. 1309–1331. DOI: 10.1002/nme.2579. URL: https://doi.org/10.1002/nme.2579.

[90] James Ahrens, Berk Geveci, and Charles Law. “Paraview: An end-user tool for large data visualization”. In: *The visualization handbook* 717.8 (2005).

[91] Dileep Kumar Ganji and G. Rajyalakshmi. “Influence of Alloying Compositions on the Properties of Nickel-Based Superalloys: A Review”. In: *Lecture Notes in Mechanical Engineering*. Springer Singapore, 2020, pp. 537–555. DOI: 10.1007/978-981-15-1071-7_44. URL: https://doi.org/10.1007/978-981-15-1071-7_44.

[92] Dayong Cai et al. “Dissolution kinetics of delta phase and its influence on the notch sensitivity of Inconel 718”. In: *Materials Characterization* 58.3 (Mar. 2007), pp. 220–225. DOI: 10.1016/j.matchar.2006.04.020. URL: https://doi.org/10.1016/j.matchar.2006.04.020.

[93] Volodymyr P. Sabelkin et al. “Mitigation of anisotropic fatigue in nickel alloy 718 manufactured via selective laser melting”. In: *Materials & Design* 182 (Nov. 2019), p. 108095. DOI: 10.1016/j.matdes.2019.108095. URL: https://doi.org/10.1016/j.matdes.2019.108095.

[94] L.Y. Wang et al. “Comparative investigation of small punch creep resistance of Inconel 718 fabricated by selective laser melting”. In: *Materials Science and Engineering: A* 745 (Feb. 2019), pp. 31–38. DOI: 10.1016/j.msea.2018.12.083. URL: https://doi.org/10.1016/j.msea.2018.12.083.

[95] Tanja Trosch et al. “Microstructure and mechanical properties of selective laser melted Inconel 718 compared to forging and casting”. In: *Materials Letters* 164 (Feb. 2016), pp. 428–431. DOI: 10.1016/j.matlet.2015.10.136. URL: https://doi.org/10.1016/j.matlet.2015.10.136.

[96] Fabrizia Caiazzo, Vittorio Alfieri, and Giuseppe Casalino. “On the Relevance of Volumetric Energy Density in the Investigation of Inconel 718 Laser Powder Bed Fusion”. In: *Materials* 13.3 (Jan. 2020), p. 538. DOI: 10.3390/ma13030538. URL: https://doi.org/10.3390/ma13030538.

[97] Michihiko Nagumo. *Fundamentals of hydrogen embrittlement*. Vol. 921. Springer, 2016.

[98] Zemin Wang et al. “The microstructure and mechanical properties of deposited-IN718 by selective laser melting”. In: *Journal of Alloys and Compounds* 513 (Feb. 2012), pp. 518–523. DOI: 10.1016/j.jallcom.2011.10.107. URL: https://doi.org/10.1016/j.jallcom.2011.10.107.

[99] Z. Tarzimoghadam et al. “Hydrogen-assisted failure in Ni-based superalloy 718 studied under in situ hydrogen charging: The role of localized deformation in crack propagation”. In: *Acta Materialia* 128 (Apr. 2017), pp. 365–374. DOI: 10.1016/j.actamat.2017.02.059. URL: https://doi.org/10.1016/j.actamat.2017.02.059.

[100] Karolien Kempen et al. “Dimensional accuracy of internal channels in SLM produced parts”. In: *2014 ASPE Spring Topical Meeting: Dimensional Accuracy and Surface Finish in Additive Manufacturing, Berkeley, CA, Apr.* 2014, pp. 13–16.

[101] Zhenbo Zhang et al. “In-situ observation of hydrogen induced crack initiation in a nickel-based superalloy”. In: *Scripta Materialia* 140 (Nov. 2017), pp. 40–44. DOI: 10.1016/j.scriptamat.2017.07.006. URL: https://doi.org/10.1016/j.scriptamat.2017.07.006.

[102] Johannes Strößner, Michael Terock, and Uwe Glatzel. “Mechanical and Microstructural Investigation of Nickel-Based Superalloy IN718 Manufactured by Selective Laser Melting (SLM)”. In: *Advanced Engineering Materials* 17.8 (June 2015), pp. 1099–1105. DOI: 10.1002/adem.201500158. URL: https://doi.org/10.1002/adem.201500158.

[103] S.H. Fu et al. “Alloy design and development of INCONEL718 type alloy”. In: *Materials Science and Engineering: A* 499.1-2 (Jan. 2009), pp. 215–220. DOI: 10.1016/j.msea.2007.11.115. URL: https://doi.org/10.1016/j.msea.2007.11.115.

[104] Shubhrodev Bhowmik, Brandon A. McWilliams, and Marko Knezevic. “Effect of powder reuse on tensile, compressive, and creep strength of Inconel 718 fabricated via laser powder bed fusion”. In: *Materials Characterization* 190 (Aug. 2022), p. 112023. DOI: 10.1016/j.matchar.2022.112023. URL: https://doi.org/10.1016/j.matchar.2022.112023.

[105] P. D. Hicks and C. J. Altstetter. “Hydrogen-enhanced cracking of superalloys”. In: *Metallurgical Transactions A* 23.1 (Jan. 1992), pp. 237–249. DOI: 10.1007/bf02660868. URL: https://doi.org/10.1007/bf02660868.

[106] Xinfeng Li et al. “Tensile mechanical properties and fracture behaviors of nickel-based superalloy 718 in the presence of hydrogen”. In: *International Journal of Hydrogen Energy* 43.43 (Oct. 2018), pp. 20118–20132. DOI: 10.1016/j.ijhydene.2018.08.179. URL: https://doi.org/10.1016/j.ijhydene.2018.08.179.

[107] C.J. McMahon. “Hydrogen-induced intergranular fracture of steels”. In: *Engineering Fracture Mechanics* 68.6 (Apr. 2001), pp. 773–788. DOI: 10.1016/s0013-7944(00)00124-7. URL: https://doi.org/10.1016/s0013-7944(00)00124-7.

[108] A. Drexler et al. “Verification of the generalised chemical potential for stress-driven hydrogen diffusion in nickel”. In: *Philosophical Magazine Letters* 100.11 (Sept. 2020), pp. 513–523. DOI: 10.1080/09500839.2020.1808253. URL: https://doi.org/10.1080/09500839.2020.1808253.

[109] M. Sundararaman, P. Mukhopadhyay, and S. Banerjee. “Deformation behaviour of γ" strengthened inconel 718”. In: *Acta Metallurgica* 36.4 (Apr. 1988), pp. 847–864. DOI: 10.1016/0001-6160(88)90139-3. URL: https://doi.org/10.1016/0001-6160(88)90139-3.

[110] Michael Janssen, Jan Zuidema, and Russell Wanhill. *Fracture Mechanics*. CRC Press, Aug. 2004. DOI: 10.1201/9781482265583. URL: https://doi.org/10.1201/9781482265583.

[111] Jiwei Lin et al. “Hydrogen permeation behavior and hydrogen-induced defects in 316L stainless steels manufactured by additive manufacturing”. In: *Materials Chemistry and Physics* 250 (Aug. 2020), p. 123038. DOI: 10.1016/j.matchemphys.2020.123038. URL: https://doi.org/10.1016/j.matchemphys.2020.123038.

[112] V.A. Popovich et al. “Impact of heat treatment on mechanical behaviour of Inconel 718 processed with tailored microstructure by selective laser melting”. In: *Materials & Design* 131 (Oct. 2017), pp. 12–22. DOI: 10.1016/j.matdes.2017.05.065. URL: https://doi.org/10.1016/j.matdes.2017.05.065.

[113] G. C. Obasi et al. “Effect of Microstructure and Alloy Chemistry on Hydrogen Embrittlement of Precipitation-Hardened Ni-Based Alloys”. In: *Metallurgical and Materials Transactions A* 49.4 (Feb. 2018), pp. 1167–1181. DOI: 10.1007/s11661-018-4483-9. URL: https://doi.org/10.1007/s11661-018-4483-9.